Universidad de Valparaíso
Facultad de Ciencias
Instituto de Física y Astronomía

Strong Gravitational Lensing as a Probe of Structure from Small to Large Scale

by

Karina Rojas Olate

Thesis presented to the Instituto de Física y Astronomía of

Universidad de Valparaíso, Chile to obtain the degree of Doctor en Astrofísica.

Advisors: Verónica Motta (Universidad de Valparaíso)

Readers: Dante Minniti (Universidad Andres Bello, UNAB)

and

Eric Jullo (Laboratoire d'Astrophysique de Marseille, LAM)

July, 2018
Valparaíso, Chile

Contents

Abstract

The gravitational lens effect occurs when the light is deflected by a gravitational field, generating multiple images or arcs. This powerful technique allows us to study structures at different scales in the universe that are usually related to different astrophysical problems. For instance, the characterization of dark objects in our galaxy (structure and mass distribution), the compact objects in the galaxy halos, the inner structure of quasars. Furthermore, it can be used to probe the cosmological model, for example through estimations of the Hubble constant (H_0) and the mass distribution profile in galaxies, groups and cluster of galaxies.

In this work I studied different structures that are affected or produced by gravitational effect. In our galaxy at interstellar scale, I searched for microlensing effects in a region of the VISTA Variable in the Vía Láctea Survey (VVV). At galaxy-size scale, I studied the microlensing effect in lensed quasars to estimate the size (r_s) and temperature profile (p) of their accretion disks and the effect of microlensing on time delay (Δt) measurements (related to H_0). At cosmological scales, I performed a dynamical analysis for groups and clusters of galaxies to finally study the mass distribution profile in their halos.

To reach these objectives I used visual and infrared images, spectroscopic data, models and simulations. The results presented in this thesis have been published in Rojas et al. (2014); Minniti et al. (2015); Verdugo et al. (2016); Motta et al. (2017); Courbin et al. (2018); Bonvin et al. (2018) among others, and part of the work is in preparation to be publish in Rojas et al. in prep(a,b), among others.

Chapter 1

Introduction

In our universe there are different types of objects and structures. Some of them are well defined as stars and planets, other are more diffuse with no clear edges as the galaxies and their halos. Some are ′invisible′ because they do not emit light like inactive black holes and the unknown dark matter, or because the technology available today can not resolve the structures like very distant quasar accretion disks and the stars in the halo of distant galaxies. One common thing among all these very different structures is their gravitational field, e.g. the dark matter existence and its properties are inferred from its gravitational effects on visible matter. This allow us to probe different structures at different scales using gravitational lensing as a tool.

The gravitational lens effect is produced when the light of a source is deflected by the lens gravitational potential, yielding multiple images, arcs or a ring around the lens. The ring is only possible when there is a perfect alignment between the source and the lens (Chwolson 1924), although it is produced when there is a small misalignment but the source is extended (Miralda-Escude & Lehar 1992; Narayan & Bartelmann 1996). Einstein predicted this effect in 1912, but was written in a unpublished note lately discovered (Schneider 2006). As Einstein was the first to describe this effect, it it is named as ′Einstein ring′.

Following a historical context, John Mitchell, Pierre-Simon Laplace, and Johann von Soldner, were the firsts to propose some bases for the gravitational lens effect (Michell 1784; Laplace 1794; Soldner 1804). Using the Newton gravitation theory they estimated the deflected angle ($\hat{\alpha}$) of the light propagating in the field of a spherical object with mass M, obtaining a relation among the gravitational constant (G), the speed of light (c), the impact parameter (ξ), and the mass: $\hat{\alpha} = 2\mathrm{GM}/(\mathrm{c}^2\xi)$. In 1911 Einstein recalculated this estimation and found a factor 2 more than the estimation based on Newtonian calculation. The Einstein estimation was confirmed in 1919 when Eddington, during a solar eclipse, observed the stars in a apparent position near to the sun and measured the deflection angle (Eddington 1919). This observation also confirmed the General Relativity Theory.

An estimation of the image positions, separation and magnification was made by Einstein (1936) requested by R. W. Mandl. His conclusion was: ′there is not great chance of observing this phenomenon, even if dazzling by the light of the much nearer star B is disregarded′, where star B was the lens. One year later, the new calculations by Zwicky (1937a,b) were published. In these studies the ′extragalactic nebulae′ (nowadays known as galaxies) were considered as lenses. Zwicky estimated a deflection angle higher by an order of 10 compared to those produced by stars, concluding that ′nebulae′ offer a better chance than stars to observe the gravitational effect. Furthermore, he included three interesting reasons to search for this phenomenon in ′nebulae′: (1) additional information to test the General Relativity Theory, (2) we could be able to see ′nebulae′ at distances greater than the ordinary, and (3) to estimate lens masses.

For around three decades there was not many studies in the field. The awakening was in 1963 where several studies revived the topic. Among those, Refsdal calculated the time delay between two images of a source and proposed the possibility of testing cosmological parameters like the Hubble constant H_0 (Refsdal 1964a,b, 1966a,b).

The first discovery of a strong gravitational lens system was made by Walsh et al. (1979). They detected a pair of quasars separated 6 arc-seconds known as Q0957+561. They confirmed that this is a gravitational lens system using spectra, both quasars are at the same redshift and show the same features. A year after the confirmation, a galaxy was detected between the two images (Stockton 1980; Young et al. 1980). The galaxy is part of a cluster which gravitational potential contribute to produce the large separation between the images.

In the following years diverse gravitational lens systems were discovered. A quadruple gravitational lens system, called PG1115+080 discovered by Young et al. (1981). The first ′Einstein ring′ discovered is MG1131+0456 (Hewitt et al. 1988). A giant arc between two clusters of galaxies was independently detected by Lynds &

Petrosian (1986) and Soucail et al. (1987), but at that time the nature of the arc was not clear. A strong gravitational effect was a possible explanation when Soucail et al. (1988) estimated that the redshift of the arcs was much higher than the redshift of the cluster.

Since 1990's several surveys search for extragalactic gravitational lens systems. some of them are: CfA-Arizona Space Telescope LEns Survey of gravitational lenses (CASTLES, Kochanek et al. 1999), Cosmic Lens All-Sky Survey (CLASS[1], Myers et al. 2003; Browne et al. 2003), the Sloan Lens ACS Survey (SLACS, Bolton 2004), the SDSS Quasar Lens Search (SQLS, Oguri et al. 2006; Inada et al. 2012), the Strong Lensing Legacy Survey (SL2S, Cabanac et al. 2006), STRong-lensing Insights into Dark Energy Survey (STRIDES, Treu et al. 2015), among others. At the moment we know roughly a hundred of lensed quasars.

The science that can be done with all these systems is multiple, and some of the goals that can be achieved to study are: the luminous and dark matter component of the lens galaxies (Kochanek et al. 2001; Oguri et al. 2002; Davis et al. 2003; Mandelbaum et al. 2009; Jiménez-Vicente et al. 2015a), the quasar inner structure (Pooley et al. 2007; Blackburne et al. 2011; Guerras et al. 2013b; Jiménez-Vicente et al. 2014; Rojas et al. 2014; Motta et al. 2017), the Hubble constant (Falco et al. 1997; Vuissoz et al. 2007; Bonvin et al. 2017; Courbin et al. 2018), galaxy cluster dynamics including substructures, luminous and dark matter content (Kneib & Natarajan 2011; Foëx et al. 2013; Jauzac et al. 2014), cosmological constraints (Schneider et al. 1992; Jullo et al. 2010; Magaña et al. 2015; Acebron et al. 2017), among others.

The modeling of strong lensed quasars opened a debate due to flux anomalies detected, i.e. discrepancies between the observed and modeled flux. For example the model for SDSS0924+0219 predict that the images A and B have approximately equal fluxes by symmetry (Keeton et al. 2006a), but the measurements show a flux difference of nearly 3 magnitudes (Figure 1.1). More complex models were studied to explain the variations in flux (Kochanek 1991; Keeton 2001; Muñoz et al. 2001; Congdon & Keeton 2005), but they did not fully explain the anomalies. Another possible explanation was dust extinction produced by the lens galaxy. The dust and gas in the galaxies is heterogeneously distributed, then, as the light of the quasar follows different paths through the lens galaxy, the flux of the images produced can be affected in different proportions by dust extinction (Falco et al. 1999; Motta et al.

[1]http://www.aoc.nrao.edu/ smyers/class.html

2002; Muñoz et al. 2004; Mediavilla et al. 2005). Although these effects play a role in several systems, they are not enough to explain the variation in flux in others. Finally, another phenomenon was proposed as an explanation: microlensing (Refsdal & Surdej 1994; Wambsganss 2006; Mediavilla et al. 2009).

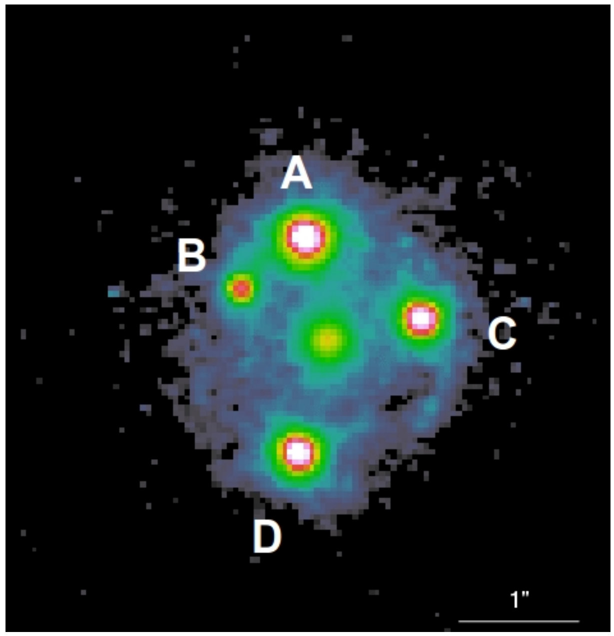

Figure 1.1: Image for the gravitational lens system SDSS0924+0219 taken with HST telescope in the filter F555W.

Microlensing is produced by stars in the lens galaxy halo crossing one or more of the lensed images and producing another light deflection (Chang & Refsdal 1979; Wambsganss 2006). The separation between the images produced by this effect are around micro-arc-seconds, hence the name microlensing, and are not resolvable individually with the observational techniques available today. This effect is size sensitive, producing large magnifications of sources with angular sizes comparable to (or smaller than) the microlens Einstein radius. In the case of quasars, the accretion disk has an apparent size comparable to the microlens, being its light affected by this effect. Microlensing can also be a chromatic effect (Wambsganss & Paczynski 1991; Wisotzki et al. 1995; Mosquera et al. 2009; Mediavilla et al. 2011). This is because, according to the thin disk model, the size of the accretion disk (r_s) varies with wavelength ($r_s \propto \lambda^p$, where p is the temperature profile), thus, the flux variation is stronger for shorter wavelengths (i.e. smaller part of the accretion disk) and almost negligible in IR.

However, QSO intrinsic variability coupled with time delay also introduce chromatic variations at a given single epoch. For example in the case of DES J0408-5359 (Figure 4.38) we can see how the magnitude difference between A and B changes at a given epoch. This image pair have a separation ∼6.0 arc-seconds, and a time delay ~ 112 days. Following Yonehara et al. (2008) we estimate that these intrinsic variations couple with time delay can produce a chromaticity change <0.04 mag. Then, special care is required to distinguish among microlensing, chromaticity, and differential dust extinction along the path of each image through the lens galaxy.

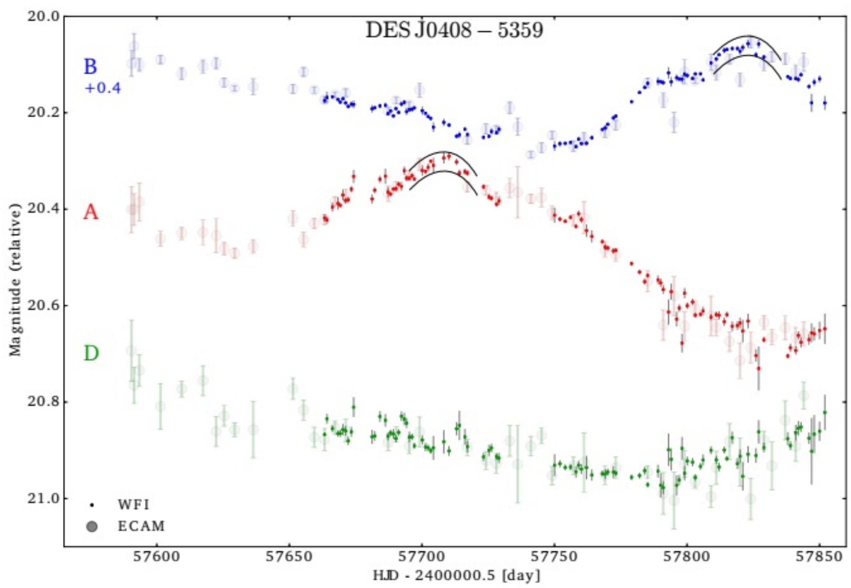

Figure 1.2: Light curve for the system DES J0408-5359. Figure taken from Courbin et al. (2018)

The microlensing effect is a useful tool to study the quasar accretion disk, the broad line region (BLR) (Guerras et al. 2013a; Braibant et al. 2014; Motta et al. 2017) and also the mass fraction of stars in haloes of distant galaxies (Mediavilla et al. 2009; Jiménez-Vicente et al. 2015a). But this effect also produce some systematic problems in the analysis of quasar light curves, which are used to estimate the Hubble constant (Tie & Kochanek 2018a).

In our own galaxy the galactic gravitational lens effect, produced between stars, is also known as microlensing because the separation of the images are just micro-arc-seconds. This is a unique technique to detect dark objects in our galaxy. Some of these kind of objects, like isolated black holes, distant brown and white dwarfs, are not possible to detect with other methods. Therefore, this technique allows us to characterize a part of the stellar population that has not been studied before, and it is also a robust probe of the structure and mass distribution in the Milky Way (Kiraga & Paczynski 1994; Gould 2001; Evans & Belokurov 2002; Wyrzykowski et al. 2015). However, an important disadvantage is that the microlensing event is not repeated, having only one chance to study the object (Dominik 2010).

Several surveys, designed with this purpose, have reported microlensing events towards the center of our galaxy, i.e. OGLE (Mao et al. 2002; Skowron et al. 2007; Udalski et al. 2015; Calchi Novati et al. 2015; Wyrzykowski et al. 2015, 2016), MOA (Alcock et al. 1997; Abe et al. 2004; Rattenbury et al. 2005; Sumi et al. 2013; Gould et al. 2014), UKIRT (Shvartzvald et al. 2017). Some of those events have also been found in surveys designed with other purposes, i.e. VISTA Variables in the Vía Láctea (VVV, Minniti et al. 2015). VVV also differs by observing in the infrared, while the other surveys use visual bands, thus going deeper into the galaxy bulge. There are also surveys that search for this effect toward M31 to investigate the outer parts of the Milky Way halo, i.e. MACHO project (Alcock et al. 2000), POINT-AGAPE (Calchi Novati et al. 2005), and EROS (Tisserand et al. 2007).

Gravitational lensing as a tool provides us with many information because allows us to characterize the geometry and content of our universe. For example, strong lensing through time delay equation depends on cosmological parameters like the Hubble constant H_0, which combined with other cosmological probes, like Cosmic Microwave Background (CMB), Baryon acoustic oscillations (BAO) or supernova, is very effective breaking degeneracies in the estimation of these parameters (Komatsu et al. 2009).

On the other hand using strong lens groups and clusters of galaxies we can study the mass distribution profile at different scales with different techniques like X-rays, dynamics, strong and weak lensing (Dressler & Shectman 1988; Clowe et al. 2006; Bayliss et al. 2013; Foëx et al. 2014; Verdugo et al. 2014; Girardi et al. 2015). Recently, has been proven that combining dynamics and strong lensing, it is possible to better constraint the mass distribution profile of groups and cluster (Verdugo et al. 2016).

The objectives of my thesis are to analyze different structures, at different scales, that are affected or produced by gravitational lens effect:

(1) I analyzed galactic microlensing light curves from the VVV. This is a public

ESO survey devoted to study the near-infrared variability in the galactic bulge and the adjacent section of the mid-plane (Minniti et al. 2010). This survey is doing a variable search and follow up of the stars in the bulge and part of the disk in the K_s band[2]. Observed microlensing events in this near-IR band give us an advantage with respect to other surveys because it allow us to observe deeper through the dust in our galaxy. I present the work done for two publications: Minniti et al. (2015) and Rojas et al. submitted to the MNRAS.

(2) I studied the microlensing effect in quasars with two objectives: to investigate the inner structure of the quasar and to explore the effect of microlensing in the estimation of time delays. For the first objective I used single-epoch spectra of lensed quasars to analyze perturbations produced by microlensing, chromatic microlensing or extinction. I present the systems HE0047-1756 and SDSS1155+6346 Rojas et al. (2014), HE2149-2745 (Motta et al. 2017), SDSS0924+0219, Q1355-2257, and SDSS1029+2623 (Rojas et al. in prep). For the second objective, I developed two codes that reproduced the work done by Tie & Kochanek (2018a) to evaluate the effect of microlensing in the estimation of the time delays in the light curves. I present my own code to reproduce the paper and the results applied to PG1115-080, Bonvin et al. (2018); Chen et al. (2018). In this same topic, I also was involved as an observer in two follow-up campaigns: STRIDES (P.I. Treu) to search for new lensed quasars and COSMOGRAIL (P.I. Courbin) to obtain light curves of lensed quasars. I present the scientific results obtained with these observations.

(3) I performed a dynamical analysis for the lens galaxy groups SL2S J02140-0535 and SL2S08521-0343 and the lens galaxy cluster Abell 1703. I present the confirmation of members using new spectroscopic candidates, and the velocity dispersion measurement. For SL2S J02140-0535, this information was used to improve the lens model and to study the mass distribution profile by combining dynamics and strong lensing (Verdugo et al. 2016). The dynamical analysis of Abell 1703 will be presented in Motta et al. in prep, and the combined analysis in Verdugo et al. in prep.

[2] and now have been extended to VVVX

Chapter 2

Theory

In this section the basics concepts about the gravitational lensing effect will be introduced. I will explain the geometry, obtain a mathematical expression for the lens equation, the time delay, the images distortion, define the critical and caustic curves, and describe the lens system configurations. I will present simple lens models used in this work, and the basic equations for microlesing.

2.1 Lens equation

The typical diagram of gravitational lens effect is shown in Figure 2.1, where a lens located at an angular diameter distance D_d from the observer, deflects the light from a source located at D_s. The lens and the source planes are perpendicular to the optical axis (dashed line in the figure). A light ray emitted by the source, with coordinates $\boldsymbol{\eta} = (\eta_1,\eta_2)$ in the source plane and $\boldsymbol{\xi} = (\xi_1,\xi_2)$ in the lens plane, is deflected an angle $\hat{\boldsymbol{\alpha}}$. Considering small angles: $\sin\hat{\alpha} \approx \hat{\alpha} \approx \tan\hat{\alpha}$. Using simple geometrical relationships, we can write (Schneider et al. 1992):

$$\boldsymbol{\eta} = \frac{D_s}{D_d}\boldsymbol{\xi} - D_{ds}\hat{\boldsymbol{\alpha}}(\boldsymbol{\xi}), \tag{2.1}$$

where we assumed that the gravitational field is weak, the potential is static, and the impact parameter $\boldsymbol{\xi}$ is larger than the Schwarzschild radius of the lens mass: $\xi \gg R_s \equiv 2GMc^{-2}$ and also the extension of the deflection mass along the line of view is smaller than the distances D_d and D_{ds}, this mass distribution is so-called *geometrically thin lens*.

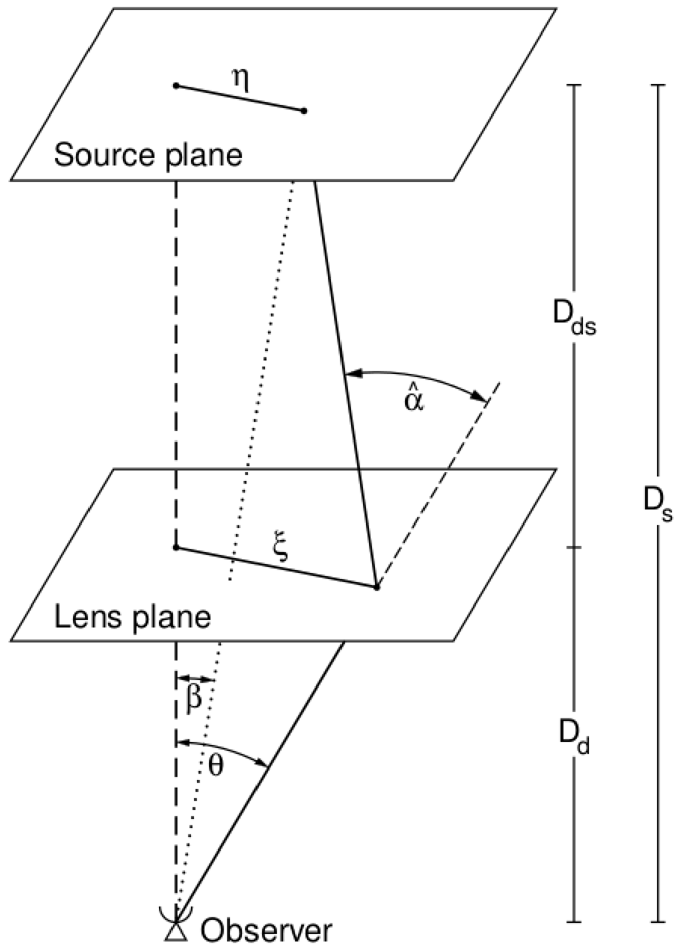

Figure 2.1: Scheme of gravitational lens effect, taken from Schneider (2006). The angular diameter distances between the lens and the source, the observer and the lens, and the observer and the source are: D_{ds}, D_d, and D_s respectively. The source is at position $\boldsymbol{\eta}$ in the source plane, its light is deflected at the lens plane an angle of $\hat{\boldsymbol{\alpha}}$ at coordinate $\boldsymbol{\xi}$, which is the impact parameter in the lens plane. The observed images have an angular position $\boldsymbol{\theta}$, that are related in the lens equation 2.3 to the angular position of the source $\boldsymbol{\beta}$.

In terms of angular coordinates:

$$\boldsymbol{\eta} = D_s\boldsymbol{\beta}, \quad \text{and} \quad \boldsymbol{\xi} = D_d\boldsymbol{\theta}, \tag{2.2}$$

where $\boldsymbol{\beta}$ is the angular position of the source, and $\boldsymbol{\theta}$ are the positions of the images. Using this description in Equation 2.1:

$$\boldsymbol{\beta} = \boldsymbol{\theta} - \boldsymbol{\alpha}(\boldsymbol{\theta}), \tag{2.3}$$

$\boldsymbol{\alpha}$ is the *scaled deflection angle*, which is related to the true deflection angle $\hat{\boldsymbol{\alpha}}$ by:

$$\boldsymbol{\alpha}(\boldsymbol{\theta}) \equiv \frac{D_{ds}}{D_s}\hat{\boldsymbol{\alpha}}(D_d\boldsymbol{\theta}), \tag{2.4}$$

Under the geometrically thin lens assumption we found that $\hat{\alpha} \ll 1$. Then, the light rays can be described like straight rays bended near to the deflector. Thus, for a geometrical thin lens, the light ray with spatial trajectory $\boldsymbol{r} = (\xi_1,\ \xi_2,\ r_3)$, that pass thought a three-dimensional density $\rho(\boldsymbol{r'})$ will be deflected by:

$$\hat{\boldsymbol{\alpha}}(\boldsymbol{\xi}) = \frac{4G}{c^2}\int d^2\xi' \int dr'_3 \rho(\xi'_1, \xi'_2, r'_3)\frac{\boldsymbol{\xi} - \boldsymbol{\xi}'}{\mid \boldsymbol{\xi} - \boldsymbol{\xi}' \mid^2}, \tag{2.5}$$

combining this Equation with 2.1, we can describe the scaled deflection angle as:

$$\boldsymbol{\alpha}(\boldsymbol{\theta}) = \frac{1}{\pi}\int_{\mathbf{R}^2} d^2\theta' \kappa(\boldsymbol{\theta}')\frac{\boldsymbol{\theta} - \boldsymbol{\theta}'}{\mid \boldsymbol{\theta} - \boldsymbol{\theta}' \mid^2}, \tag{2.6}$$

where κ is the dimensionless surface mass density or convergence, defined as:

$$\kappa(\boldsymbol{\theta}) = \frac{\sum(D_d\boldsymbol{\theta})}{\Sigma_{cr}}, \tag{2.7}$$

and Σ_{cr} is the critical surface mass density:

$$\Sigma_{cr} = \frac{c^2}{4G\pi}\frac{D_s}{D_d D_{ds}} \tag{2.8}$$

Depending on the value of Σ_{cr} we can distinguish between strong and weak lensing. When $\kappa \geq 1$ the lens will be able to produce multiple images corresponding to a strong lensing regime, while $\kappa < 1$ corresponds to the weak lensing regime.

To study more complex density profiles, we define the *effective lensing potential*:

$$\psi(\boldsymbol{\theta}) = \frac{1}{\pi}\int_{\mathbf{R}^2} d^2\theta' \kappa(\boldsymbol{\theta}') ln \mid \boldsymbol{\theta} - \boldsymbol{\theta}' \mid, \tag{2.9}$$

that is a Newtonian potential scaled and projected onto the lens plane. Following the property $\bigtriangledown \ln\mid \boldsymbol{\theta} \mid = \boldsymbol{\theta} / \mid \boldsymbol{\theta}^2 \mid$, we can rewrite the scaled deflected angle like $\boldsymbol{\alpha}(\boldsymbol{\theta}) = \bigtriangledown\psi(\boldsymbol{\theta})$.

The effective lensing potential is related to the dimensionless surface mass density using the Poisson equation:

$$\nabla^2\psi = 2\kappa. \tag{2.10}$$

2.2 Time delay

The light rays from the source follow different paths once they are deflected by the gravitational potential of the lens. The Fermat principle says: ′The light path to propagate from one point to another is such that the time spent in travel is stationary with respect to possible variations of the trajectory′ (Feynman 1963), and is defined as:

$$\tau(\boldsymbol{\theta};\boldsymbol{\beta}) = \frac{1}{2}(\boldsymbol{\theta}-\boldsymbol{\beta})^2 - \psi(\boldsymbol{\theta}). \tag{2.11}$$

This potential is connected with the excess time delay by:

$$t(\boldsymbol{\theta};\boldsymbol{\beta}) = \frac{D_d D_s}{cD_{ds}}(1+z_d)\tau(\boldsymbol{\theta};\boldsymbol{\beta}), \tag{2.12}$$

$$= \frac{D_d D_s}{cD_{ds}}(1+z_d)\left[\frac{1}{2}(\boldsymbol{\theta}-\boldsymbol{\beta})^2 - \psi(\boldsymbol{\theta})\right], \tag{2.13}$$

where z_d is the lens redshift. The derivation of these equations can be seen in Schneider (1984) or in Schneider et al. (1992). The time delay has a geometrical and gravitational component. The geometrical component corresponds to the first term in the bracket of Equation 2.13 and is related to the additional path length of the observed light ray. The gravitational component is the second term and is associated with the gravitational delay due to the lens mass distribution.

In terms of lensing effect, the Fermat principle states that the images of the source will be formed at positions $\boldsymbol{\theta}$ where the time delay will be stationary: $\nabla_\theta t(\boldsymbol{\theta};\beta) = \nabla_\theta \tau(\boldsymbol{\theta};\beta) = 0$. The application of this condition in the equation 2.13 yields the lens equation 2.3.

The equation 2.12 can be simplified as:

$$t(\boldsymbol{\theta};\boldsymbol{\beta}) = \frac{D_{\Delta t}}{c}\tau(\boldsymbol{\theta};\boldsymbol{\beta}), \tag{2.14}$$

where $D_{\Delta t}$ is the *time-delay distance*, defined as:

$$D_{\Delta t} \equiv (1+z_d)\frac{D_d D_s}{D_{ds}}. \tag{2.15}$$

In the specific cases of quasars as lensed sources, where the brightness vary with time, we can measure the time delay between two images as:

$$\Delta t_{ij} = \frac{D_{\Delta t}}{c}\left[\frac{(\boldsymbol{\theta}_i - \boldsymbol{\beta})^2}{2} - \psi(\boldsymbol{\theta}_i) - \frac{(\boldsymbol{\theta}_j - \boldsymbol{\beta})^2}{2} + \psi(\boldsymbol{\theta}_j)\right]. \tag{2.16}$$

For those systems with measured time delays, it is possible to determine $D_{\Delta t}$ using this equation. Furthermore, Δt_{ij} is inversely proportional to the Hubble constant H_0. Given the mass distribution, the time delay measurement allows the study of the parameter and also other cosmological tests (Refsdal 1964a; Fadely et al. 2010; Suyu et al. 2013; Bonvin et al. 2017; Courbin et al. 2018).

2.3 Images

The shape of the images can be different from the shape of the source because the light rays are deflected differentially by the gravitational potential, but the brightness of the source remains intact. Following the Liouville's theorem, assuming that there is no emission or absorption of photons, the lens effect conserves the source surface brightness. That means that the surface brightness distribution in the source plane ($\mathrm{I}^{(s)}[\boldsymbol{\beta}(\boldsymbol{\theta})]$) is the same as the one observed in the lens plane ($\mathrm{I}(\boldsymbol{\theta})$). To quantify the change in the shape of the source, we assume a local linear approximation and define the Jacobian matrix:

$$\mathcal{A}(\boldsymbol{\theta}) = \frac{\partial \boldsymbol{\beta}}{\partial \boldsymbol{\theta}} = (\delta_{ij} - \frac{\partial^2 \psi(\boldsymbol{\theta})}{\partial \theta_i \partial \theta_j}) = \begin{pmatrix} 1-\kappa(\boldsymbol{\theta})-\gamma_1(\boldsymbol{\theta}) & -\gamma_2(\boldsymbol{\theta}) \\ -\gamma_2(\boldsymbol{\theta}) & 1-\kappa(\boldsymbol{\theta})+\gamma_1(\boldsymbol{\theta}) \end{pmatrix}, \tag{2.17}$$

where γ_1 and γ_2 are the components of the shear:

$$\gamma \equiv \gamma_1 + i\gamma_2. \tag{2.18}$$

The shear components are the second derivatives of the lens potential:

$$\gamma_1 = \frac{1}{2}(\psi_{,11} - \psi_{,22}),\ \gamma_2 = \psi_{,12}, \tag{2.19}$$

where the subindex in the lens potential correspond to: $\psi_{,ij} = \dfrac{\partial^2\psi}{\partial\theta_i\partial\theta_j}$.

To visualize the distortion we considered a point within the source, $\boldsymbol{\beta}_0 = \boldsymbol{\beta}(\boldsymbol{\theta}_0)$ corresponding to a point within the image, $\boldsymbol{\theta}_0$. Using the Liouville's theorem we obtain the locally linearized lens equation:

$$I(\boldsymbol{\theta}) = I^{(s)}[\boldsymbol{\beta}_0 + \mathcal{A}(\boldsymbol{\theta}_0)(\boldsymbol{\theta} - \boldsymbol{\theta}_0)]. \tag{2.20}$$

Considering a small circular source with radius R parametrized by:

$$\boldsymbol{\beta}(\lambda) = \boldsymbol{\beta}_0 + R(\cos\lambda, \sin\lambda), \tag{2.21}$$

with λ varying from 0 to 2π. Using this information in the equation 2.17 we obtain:

$$\mathcal{A}(\boldsymbol{\theta}) = \frac{R(1-\kappa-\gamma_1)}{R(1-\kappa+\gamma_1)} \begin{pmatrix} \cos\lambda \\ \sin\lambda \end{pmatrix}, \tag{2.22}$$

where the resulting images have an elliptical distortion produced by γ_1 values. Then, the mayor axis (a) and minor axis (b) are:

$$a = \frac{R}{(1-\kappa)(1- \mid g \mid)}, b = \frac{R}{(1-\kappa)(1+ \mid g \mid)}, \tag{2.23}$$

where g is the *reduced shear*:

$$g(\boldsymbol{\theta}) = \frac{\gamma(\boldsymbol{\theta})}{1-\kappa(\boldsymbol{\theta})}. \tag{2.24}$$

An important consequence of the image distortion is the magnification in the images. Integrating over the brightness distribution I($\boldsymbol{\theta}$) and I$^{(s)}(\boldsymbol{\beta})$, we obtain the observed fluxes of the image and the unlensed source, respectively. The ratio between these two values is the magnification $\mu(\boldsymbol{\theta}_0)$, related to the magnification tensor, M($\boldsymbol{\theta}$), that yields the local mapping from the source plane to the image plane. This tensor is the inverse of the Jacobian matrix $\mathcal{A}(\boldsymbol{\theta})$. Thus, the magnification factor is:

$$\mu(\boldsymbol{\theta}) = \det(M(\boldsymbol{\theta})) = \frac{1}{\det(\mathcal{A}(\boldsymbol{\theta}))} = \frac{1}{(1-\kappa)^2 - \mid \gamma \mid^2}. \tag{2.25}$$

Images with $\mu > 0$ are images with positives parities while images with $\mu < 0$ have negative parities. Furthermore, the images with negative parities are mirror images of the background source.

2.4 Critical and caustic curves

The *critical curves* correspond to the location where the magnification is maximum, then, $\det(\mathcal{A}) = 0$. Theoretically, the magnification in the critic curve is infinite, but in the practice this does not happen. Mapping the critical curves to the source plane using the lens equation (2.1) gives the *caustic curves* on the source plane. The shape of the curves depends on the lens distribution as the Figure 2.2 shows. One of the most simple case is a circular mass distribution (a), where the critical curve is a circle and the caustic curve is a point. Another simple example are the curves in (b) where the mass distribution is elliptical, the caustic have the shape of a diamond, called *astroid*. The four smooth curves of the astroid are known as *folds* and the place where they join is known as *cusp*. A little more complex mass distribution is shown in panel (f) with a bimodal distribution with unequal masses, in here both, critical and caustics curves, have complicated shapes, like those in cluster of galaxies, where the mass distribution is the contribution of many unequal masses. In all of the cases we see one *tangential* critical curve, where the lensed systems locate tangentially to the radius, and one *radial* critical curve, where the images are magnified radially in the vicinity (and their corresponding caustics), but when the lens have circular symmetry these curves are a point.

Back to simple cases, when we have a galaxy as lens, the number of the images produced depends on the relative position between the source and the caustic curves, and the distribution of the images depends on the source displacement along to the axis of the potential (Schneider 2006). A source outside of the astroid but inside of the tangential critical curve will produce three images, but a source inside of the caustic will produce five images (Figure 2.3). Most of the known systems are doubles or quadruples, this is because the 3rd and 5th images in general are demagnified and located in the center of the lens, thus obstructed by the lens galaxy. From Figure 2.3 we see four different examples modeled using the code *lensmodel* (Keeton 2001), where (a) is the case already mentioned, in which three images are formed, (b) is a particular case that happen when the observer, the lens and the source are nearly aligned (and the galaxy is not symmetric) then the image configuration is the called 'Eintein cross'. In the case of (c) the source lie near a fold, thus two of the images are formed closer. Finally, in the case (d) the source is near one cusp, producing three images at one side of the lens.

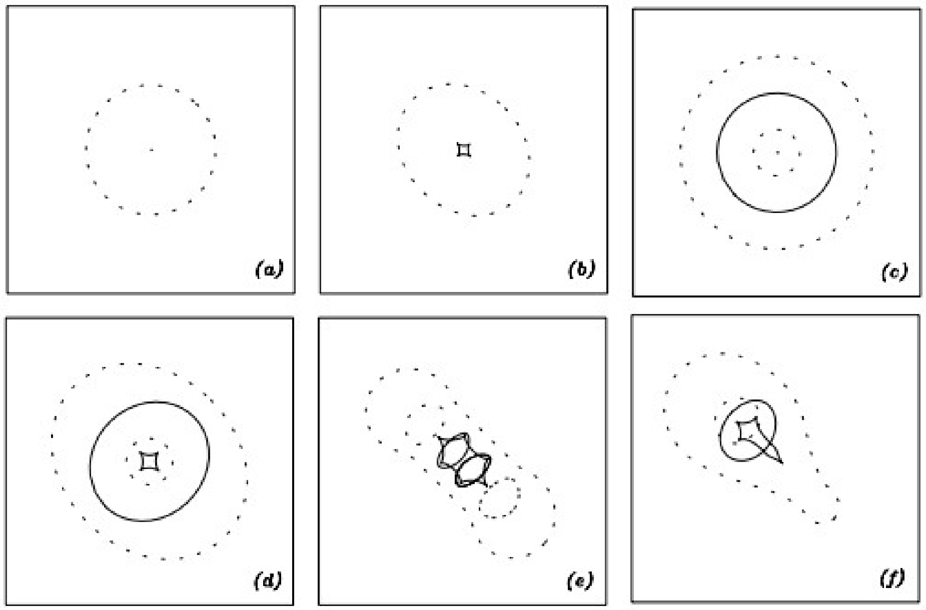

Figure 2.2: Critical and caustic curves for different mass distributions, figure taken from Kneib & Natarajan (2011). The dashed lines are the critical curves and the solid lines are the caustics. The different mass distributions are: (a) circular, (b) singular isothermal ellipsoid, (c) circular with a inner slope shallower than the isothermal mass distribution. (d) elliptical with a inner slope shallower than the isothermal mass distribution. (e) bimodal with two clumps of equal mass. (f) bimodal with unequal masses.

According to the theory, the flux of the merging images in the fold and cusp obey certain relationships. The fold relation says that the magnification of two images have to be the same but with opposite parity:

$$\mu_1 + \mu_2 = 0, \quad | \mu_1 |=| \mu_2 |, \tag{2.26}$$

and for cusp the lens the magnification of the three nearby images are related as:

$$\mu_1 + \mu_2 + \mu_3 = 0, \quad | \mu_2 |=| \mu_1 | + | \mu_3 |, \tag{2.27}$$

where μ_2 is the magnification of the image that it is produced inside of the tangential critical curve.

In practice, both relations are often unfulfilled due to external factors like time delay, dust extinction, intrinsic variability of the source, and microlensing.

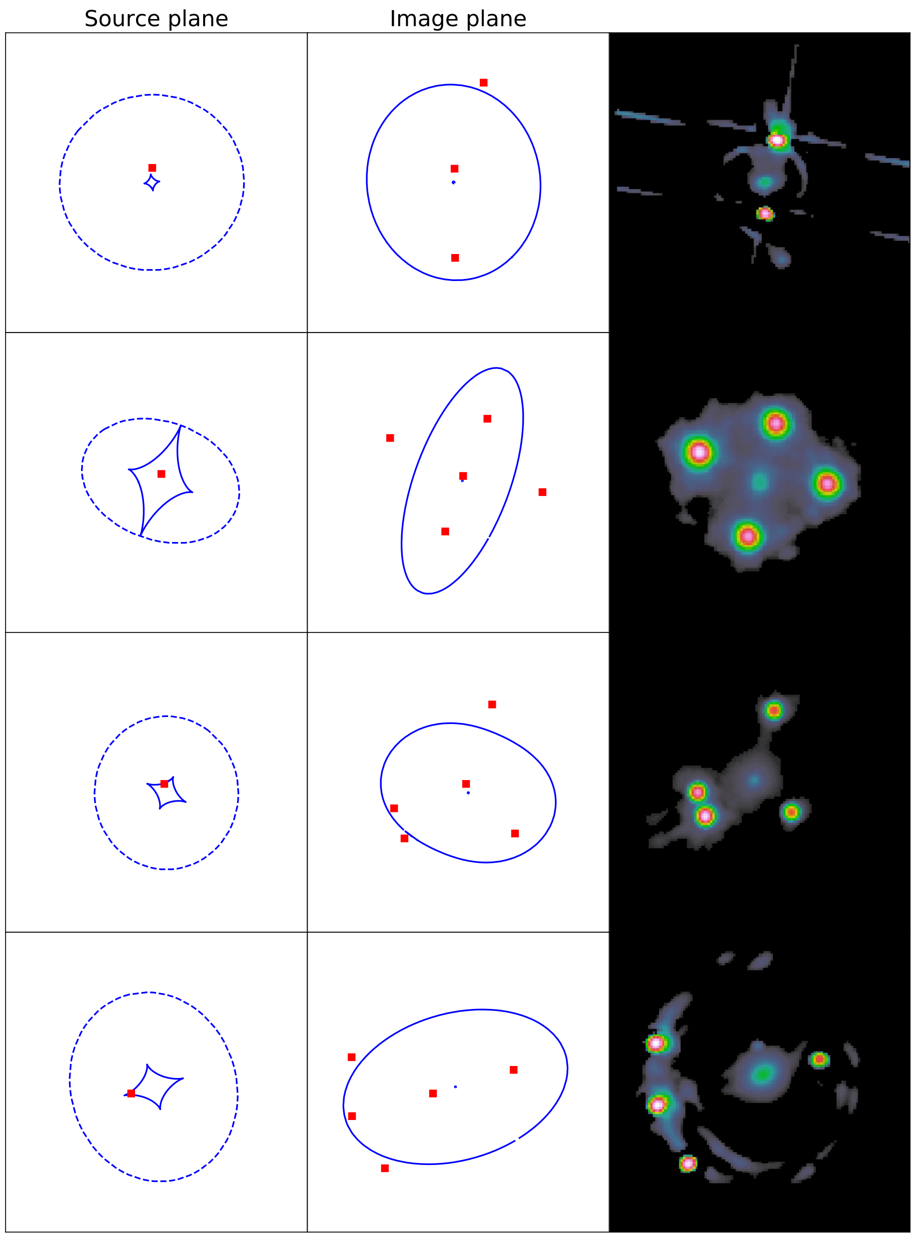

Figure 2.3: Different image configuration depending of the source position using as examples the systems HE0047-1756, HE0435-1223, PG1115+080, and RXJ1131-1231. The four systems where modeled using lensmodel (Keeton 2001). The systems where modeled with a Singular Isothermal Ellipsoid (SIE) with the exception of PG1115+080 which is modeled with a Singular Isothermal Ellipsoid plus shear (SIE+γ), the explanation of the model can be found in Section 2.5. The blue lines are the critical and caustics curves corresponding the image and source plane respectively. The red squares in the source plane represent the location of the source and in the image plane they represent the image positions. The images of the systems where taken HST telescope using F555W filter and where obtained from CASTLES database, and show the quasar images and the lens galaxy in the middle.

2.5 Simple lens models

Modeling of the gravitational lens systems allow us to obtain more information about them, for example, the influence of external gravitational potentials deforming the images, the mass convergence and shear in the region of the images, estimate the time delay, among others. First, we need to solve the lens equation, but some parameters like the total deflection angle are not easy to obtain because numerical integrations are needed. For some simple mass distributions it is possible to obtain analytical expressions for the deflection angle. In this section I will explain the lens models used in this work.

2.5.1 The point-mass lens

This is the simplest lens representation, where the lens is a point with mass M and, for simplicity, it is located in the origin of the lens plane. The lens equation for this case is:

$$\boldsymbol{\beta} = \boldsymbol{\theta} - \theta_E^2 \frac{\boldsymbol{\theta}}{\mid \boldsymbol{\theta} \mid^2}, \tag{2.28}$$

where θ_E is the angular radius of the critical curve, the so called *Einstein radius*, and it is defined as:

$$\theta_E = \left(\frac{4GM}{c^2} \frac{D_{ds}}{D_d D_s} \right)^{1/2}, \tag{2.29}$$

in the specific case of a point-mass lens $\theta_E = (\theta_1 \theta_2)^{1/2}$, where θ_1 and θ_2 are the position of the two images formed. In the case of stellar lens effect, the Einstein radius is related to the mass M by:

$$\theta_E^2 = CM\pi_{rel}, \theta_E = \mu_{rel} t_E \quad C \equiv \frac{4G}{c^2 AU} \simeq 8.1 \frac{mas}{M_\odot}, \tag{2.30}$$

where π_{rel} is the relative parallax between the lens and the source.

The solutions for the lens equation can be written in terms of $u_\pm = \theta/\theta_E$ and $u = \beta/\theta_E$:

$$u_\pm = \frac{1}{2} \left(u \pm \sqrt{u^2 + 4} \right). \tag{2.31}$$

The magnification of the images is given by:

$$\mu_{\pm} = \frac{1}{det\mathcal{A}} = \left(1 - \frac{1}{u_{\pm}^4}\right)^{-1}, \tag{2.32}$$

then the total magnification is:

$$A = A_{+} + A_{-} = \frac{u^2 + 2}{u\sqrt{u^2 + 4}}. \tag{2.33}$$

2.5.2 Singular models

The *Singular Isothermal Sphere* (SIS) model is the simplest parameterization of the spatial distribution of matter to represent a galaxy. In the case of gravitational lens system it is a good first approximation to continue with more complicated models. The three-dimensional mass density distribution is described by:

$$\rho(r) = \frac{\boldsymbol{\sigma}_v^2}{2\pi G r^2}, \tag{2.34}$$

where σ_v is the velocity dispersion, and r is the radius. The central density diverges as $\rho \propto \mathrm{r}^{-2}$, for that reason this model is called *singular*. A finite core radius can fix this problem. The surface mass density is:

$$\Sigma(\xi) = \frac{\sigma_v^2}{2G}\xi^{-1}. \tag{2.35}$$

The one-dimensional lens equation for the model is:

$$\beta = \theta - \theta_E \frac{\theta}{\mid \theta \mid}, \tag{2.36}$$

where the Einstein radius for this case is:

$$\theta_E = 4\pi \left(\frac{\sigma_v}{c}\right)^2 \frac{D_{ds}}{D_s}. \tag{2.37}$$

The magnification for the SIS model is:

$$\mu = \frac{1}{det\mathcal{A}} = \frac{\mid \theta \mid}{\mid \theta \mid - \theta_E}. \tag{2.38}$$

The SIS model is unrealistic to describe most of the observed lens systems. To improve it, we add two parameters: the ellipticity and the position angle that describe the lens orientation. Then, this model consider the elliptical gravitational potential of the lens galaxy. The addition of these parameters complicates the mathematical construction of this model. The density distribution is described as:

$$\rho(r) = \frac{\sigma_v^2}{2\pi G r_e^2}, \quad r_e^2 = r_x + r_y/q \tag{2.39}$$

where q is the projected axis ratio, for the SIS case r_x=r_y. When $r_x \neq r_y$ we have the case of a Singular Isothermal Ellipsoid (SIE) model.

More complicated models to describe for example the mass density in the halos of galaxies come from to the cosmological N-body simulations. The so-called NFW (Navarro et al. 1996, 1997) predicted that mass density profile is given by:

$$\rho(r) = \frac{\rho_s}{(r/r_s)(1 + r/r_s)^2}, \tag{2.40}$$

where ρ_s is a characteristic density and r_s is the scale radius that corresponds to the region where the logarithmic slope of the density equals the isothermal value.

2.6 Microlensing

This effect is produced by low mass objects like planets, stars and black holes. The angular separation between the multiple images of the source is of the order of micro-arc-seconds, thus with the current instrumentation it is very difficult to resolve them individually. The phenomenon is detectable because the relative motion between the source, the object field and the observer, produce an increase and decrease of the brightness of the source. This is a transient effect and its duration depends on the lens mass and the relative distances: hours for planets (Gould 2005), weeks for stars in our galaxy (Paczynski 1996; Wambsganss 2006), and years for stars in lens galaxy halos (Kochanek 2004). In this subsection I will present two of the microlensing cases studied in this thesis.

2.6.1 Galactic microlensing toward the galactic center.

In this case, the microlensing events are produced by stars located in the disk of our galaxy which magnify sources located in the bulge. Since the lens subtends a small angle, we can treat this case as a point-mass lens (Paczynski 1991). The magnification is described by the Equation 2.33 where the parameter u is related to the impact parameter (u_0), the time of the maximum magnification (T_0), and the Einstein crossing time (t_E) through the following relationship:

$$u = u_0^2 + \left(\frac{t - T_0}{t_E}\right). \tag{2.41}$$

Paczynski (1996) showed that the mass M of the obscured lens is related to the Einstein crossing time by:

$$t_E = 0.215 yrs \left(\frac{M}{M_\odot}\right)^{1/2} \left(\frac{D_d}{10kpc}\right)^{1/2} \left(1 - \frac{D_d}{D_s}\right)^{1/2} \left(\frac{200kms^{-1}}{V}\right), \tag{2.42}$$

where D_d is the distance to the deflector, D_s is the distance to the source and V is the transverse velocity of the lens relative to the source.

2.6.2 Quasar microlensing

This effect is produced by stars in the lens galaxy halo. Chang & Refsdal (1979, 1984) studied the lensed quasar images and how these would be affected by stars in the lens galaxy halo. They found that micro-images with separations of the order of 10 micro-arc-seconds will be formed. They estimated, using the surface mass density κ and the optical depth, that at the position of the macro-images, at any given time, the microlenses can affect the brightness of the lensed quasar. Where the optical depth is defined as the probability that a microlensing event will be occurring at any instant in a particular direction for a single source. The first observational evidence was reported by Irwin et al. (1989) in an image of the quadruple lens system Q2237+0305. To detect this effect it is possible to use two observational techniques: light curves or spectra.

In the first case, monitoring the images of the lens system for months allows to notice the variation produced by microlensing. The technique consist on comparing the amplitude and variability in the images assuming that at least one of them is not affected by microlensing. For example, in the case of Q2237+0305, after years of monitoring and more than 100 data points per year, it was possible to confirm that all four images vary constantly in periods of months (Udalski et al. 2015). This is a very special case because all the images are seen through the bulge of the spiral lens galaxy. In most of the known lensed quasars the images are formed in the halo of an elliptical lens galaxy, then the variations are slower than in the previous case and not necessarily all the images are affected at the same time, because they are formed in a sparsely populated region compared to the bulge of a spiral galaxy. Monitoring campaigns are following several systems with the main goal to measure accurate time delays and estimate the Hubble constant, e.g. COSmological MOnitoring of GRAvItational Lenses (COSMOGRAIL, Eigenbrod et al. 2005). Microlensing plays a important role introducing systematic errors in the measurements (Tie & Kochanek 2018a,b).

In the second case, using single epoch spectra, it is possible to determine if there is microlensing effect in the images of the quasar (Moustakas & Metcalf 2003). This effect is size sensitive, producing large magnifications of sources with angular size comparable to (or smaller than) the microlens Einstein radius. That means that regions like the accretion disk and the Broad Line Region (BLR) can be affected, but larger regions like the Narrow Line Region (NLR) are not sensitive to this effect. Using this property, we can search for microlensing in the spectra of lensed images. As the continuum comes from the accretion disk and the core of the emission lines from NLR, we compare the magnitude differences between of two images (e.g., A and B) in the continuum under the emission lines with the magnitude difference in the emission line cores[1], uncontaminated by the continuum:

$$\Delta m = \mid (m_B - m_A)_{core} - (m_B - m_A)_{cont.} \mid . \tag{2.43}$$

If we find differences in $(m_B - m_A)_{core}$ along the wavelength, these can be produced by extinction that come from different amounts of dust and gas in the lens galaxy. If $(m_B - m_A)_{core}$ do not present any change along the wavelength, it is considered as no-microlensing baseline, thus $\Delta m \neq 0$ means the presence of microlensing effect in one or both images of the quasar. Furthermore, if $(m_B - m_A)_{cont}$ change with wavelength, being larger in the blue than in the red, the system exhibits chromatic microlensing effect. The chromatic variation are produced because, according to the thin disk model (Shakura & Sunyaev 1973), the size of the accretion disk (r_s) varies with wavelength ($r_s \propto \lambda^p$, Wambsganss & Paczynski 1991; Wisotzki et al. 1995; Mosquera et al. 2009; Mediavilla et al. 2011) and this effect is size sensitive, i.e.

[1]that is a region of ~ 20 Å around the center of the line

the magnification will be different depending of the wavelength (regions of the disk). These variations are also detected in light curves at different wavelengths (Eigenbrod et al. 2008) and, allow us to estimate the size r_s and temperature profile p of the accretion disk (Mediavilla et al. 2011; Rojas et al. 2014; Motta et al. 2017).

Also, as BLR can be affected by microlensing, mostly in high ionization emission lines like CIV and CIII] and some UV iron emission lines like FeII and FeIII (Guerras et al. 2013b) we can estimate a size for this region. This effect can be detected comparing the profile of the emission lines, if there is significantly differences in the broad emission line this can be sign of microlensing.

Chapter 3

Galactic microlensing results

In this chapter I present galactic microlensing results using the data from the VISTA Variables in the Vía Láctea survey (VVV). The analysis were published in Minniti et al. (2015) and Rojas et al. in prep.

As I mentioned in subsection 2.6.1 the events are produced by dark objects located in the disk of our galaxy, increasing the brightness of sources located in the bulge. Since the lens subtends a small angle, we can treat this case as a point-mass lens (Paczynski 1991), where the magnification is given by the equations 2.33 and 2.40. Paczynski (1996) showed that the mass M of the obscured lens is related to the Einstein crossing time, equation 2.41, and Gould (2001) showed that M is related to the proper motion, the relative parallax, and the Einstein crossing time using the equation 2.30.

The VVV is a public ESO survey devoted to study the near-infrared variability in the galactic bulge and the adjacent section of the mid-plane (Minniti et al. 2010). This survey is doing a variable search and follow up of the stars in the bulge and part of the disk in the K_s band. Observed microlensing events in this near-IR band give us an advantage with respect to other surveys because it allow us to observe deeper through the dust in our galaxy.

The observations used in this chapter are acquired with VISTA 4m telescope at Paranal Observatory, Chile. The telescope use a near-infrared (NIR) camera (VIRCAM, VISTA Infrared CAMera, Dalton et al. 2006) with five broad band filters (Z,Y,J,H, and K_s). The camera contains 67 million pixels (i.e., an array of 16x2048x2048 pixels) and the field-of-view is 1.65 deg^2. The variability search and follow up is carried out in the K_s-band (Saito et al. 2012). The reduction, astrometry and stacking are made by the Cambridge Astronomy Survey Unit (CASU) using the VISTA Data Flow System pipeline (Emerson et al. 2004; Hambly et al. 2004; Irwin et al. 2004).

3.1 Microlens stellar mass black hole candidate in VVV Survey

*This section is based on the publication: 'VVV Survey observations of a microlensing stellar mass black hole candidate in the field of the globular cluster NGC 6553' by D. Minniti, R. Contreras Ramos, J. Alonso-García, T. Anguita, M. Catelan, F. Gran, V. Motta, G. Muro, **K. Rojas**, and R. K. Saito, 2015 ApJ, 810, L20*

We report the discovery of a microlensing event with the VVV Survey. Based on the position in the color-magnitude diagram the source is a bulge giant star with magnitude $K_s = 13.52$. As the microlensing event is projected only 3.5 arcmin away from the center of the globular cluster NGC 6553, the lens may be located in the globular cluster. The distance and proper motions of the cluster are known, if the lens is part of the cluster its mass is $M = 1.5 - 3, 5M_{\odot}$, which corresponds to a black hole. If the lens is not part of the cluster but it is located in the galactic disk, the mass also points to a massive stellar remnant.

3.1.1 Microlensing event observation

We performed PSF photometry using Dophot (Schechter et al. 1993; Alonso-García et al. 2012). The object in each image were cross-correlated using the STILTS package (Taylor 2006), and the light curves generated were then analyzed for variability (see Alonso-García et al. (2015)).

We discovered a microlensing event located at R.A.(J2000) = 18:09:13.86, Dec.(J2000) = 25:57:52.7. The event is located only 3.5 arcmin away from the cluster center with tidal radius $R = 8.16$ arcmin (figure 3.1-left). The peak of the event is in 2012 season, the brightness of the source star increase from a constant magnitude of $K_s = 13.5$ to up $K_s = 12.8$.

The seeing for the different data points vary between 0.6 and 1.2 arc-seconds. The source is located between two bright saturated stars with $K_s < 12$, and separated

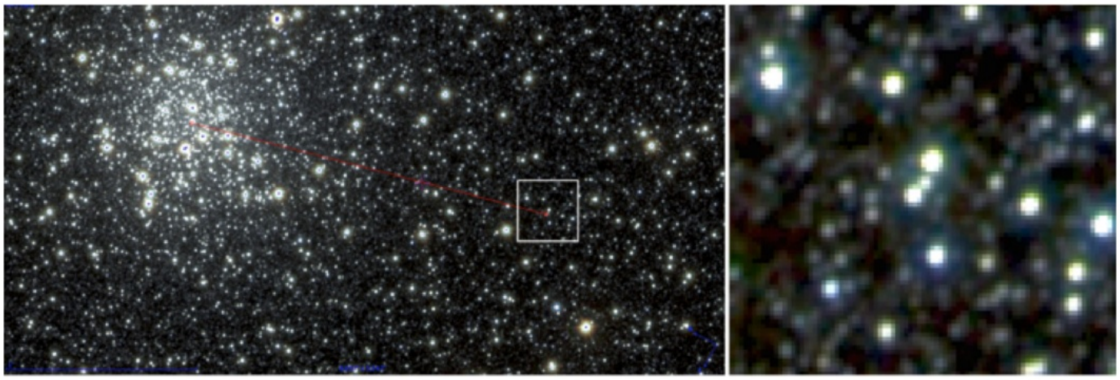

Figure 3.1: Image of the cluster NGC 6553 and the microlensing event, taken from Minniti et al. (2015). Left: Finding chart (6.8 x 3.5 arc-min) with the cluster, the red line start in the center of the cluster and end in the microlensing event that is in the white box. Right: Zoom of 30 x 30 arcsec^2 where is the event, the seeing of the image is 0.8 arcsec

Table 3.1: lens model parameters

Model	K_s [a]	u_0	T_0 (JD)	t_E (days)	f	χ^2
Simple	13.515 ± 0.002	0.62 ± 0.004	56117.5 ± 0.43	51.3 ± 0.8	1.0	201
Simple + f	13.515 ± 0.002	0.46 ± 0.08	56117.4 ± 0.42	62.5 ± 9	0.61 ± 0.17	199

by 3 arc-seconds (figure 3.1 right). In the worst seeing conditions the photometry value presents large errors as can be seen in the light curve (figure 3.2).

We fit the light curve with a simple lens model (Equation 2.33)and for comparison we also fit the event with a simple lens model including the blending parameter (f). The parameter obtained from both fits are in table 3.1.

The χ^2 obtained shows that there is no improvement with the addition of a blending factor. The shape of the light curve is symmetric enough to not correspond to any other transient events like a nova, dwarf novae or super nova, which typically show a fast increase in brightness and a slow declination.

OGLE independently found this event[1] in I band, the parameters reported by OGLE are in agreement with those fitted with VVV data.

3.1.2 NGC 6553

The physical parameters of this cluster are well known. It is an old and metal-rich bulge globular cluster (Minniti 1995; Ortolani et al. 1995; Barbuy et al. 1998; Zoccali

[1] http://ogle.astrouw.edu.pl/ogle4/ews/2012/blg-0548.html

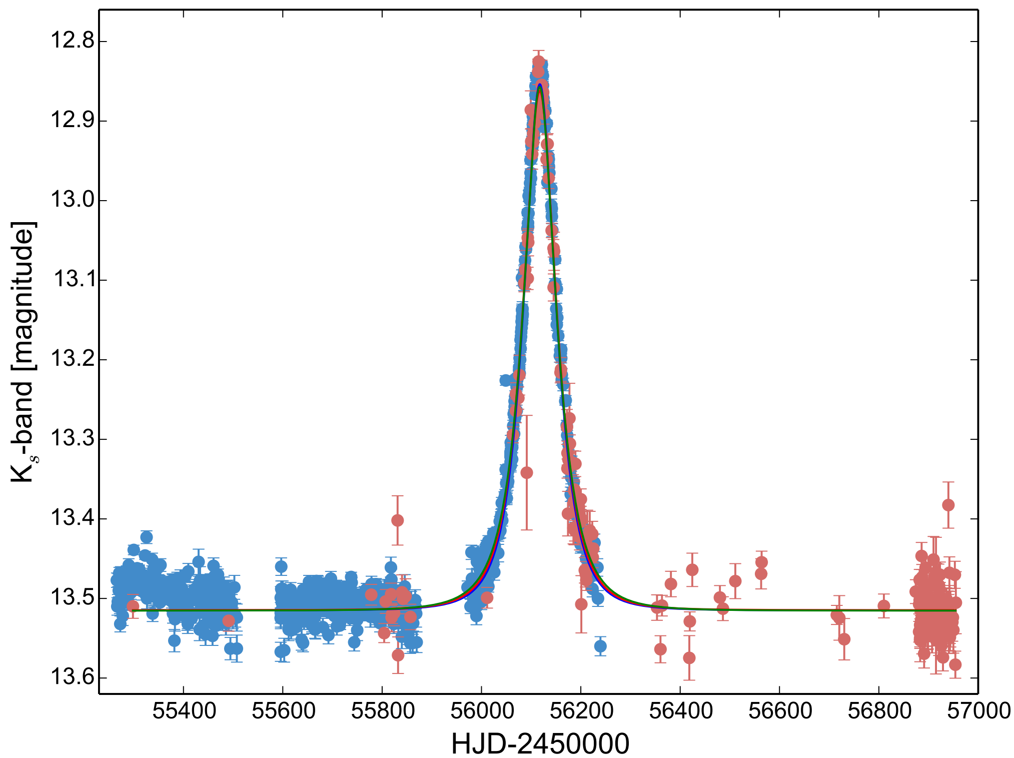

Figure 3.2: Light curve for the microlensing event. Light-blue data are from OGLE. Pink data is from VVV survey. The lines are the best fit of VVV-unblended (red), VVV-blended (green) and the fit provided by OGLE (blue). The data from OGLE taken in I band was shifted to fit the K$_s$ magnitudes of VVV data.

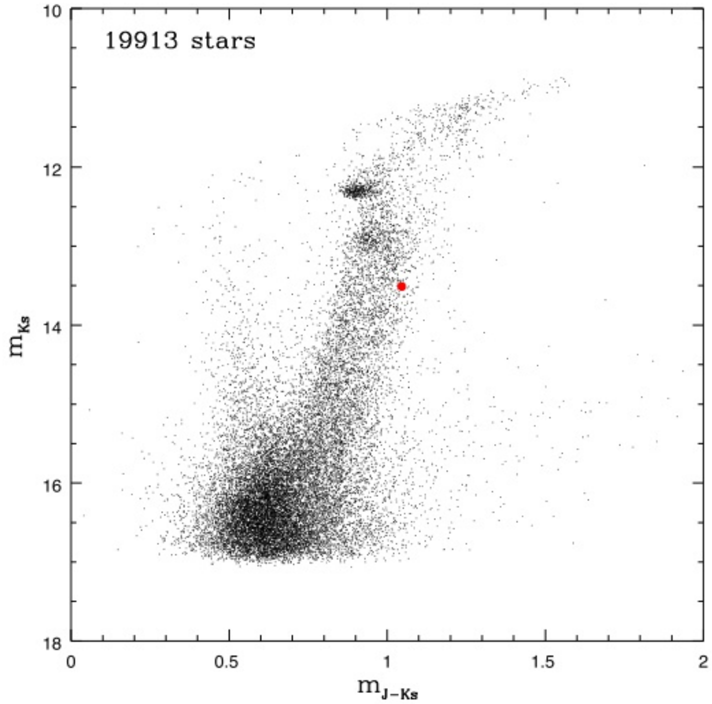

Figure 3.3: color magnitude diagram $K_s vs J - K_s$ of the field centered in the globular cluster, taken from Minniti et al. (2015). The red circle is the source star of the microlensing event.

et al. 2001). It is moderately concentrated with a core radius $r_c = 0.55$ arcmin and a tidal radius $r_t = 8.16$ arcmin. The cluster is very reddened: $E(B - V) = 0.73$, $A_v = 2.26$, and $A_{k_s} = 0.23$ (Barbuy et al. 1998). Following Alves-Brito et al. (2006), we adopt a distance of 6.0 kpc for the cluster, observing the cluster horizontal branch at $K_s = 12.5$ (figure 3.3) the distance measured is consistent.

The relative proper motion of the cluster with respect to the bulge is $\mu_\ell = 5.89$ and $\mu_b = 0.42$ mas/yr (Zoccali et al. 2001). Thus, the relative mean proper motion difference between bulge and cluster in the sky is 5.9 mas/yr.

For the further microlensing analysis the distances matter. Then, if the lens would be part of the cluster, relative mean proper motion difference between bulge and cluster will be the same for the lens. Following the procedure in Yee et al. (2013), there is roughly 50% probability that the lens belongs to the cluster. On the other hand, the source star is redder than the RGB of the globular cluster, consistent with a bulge giant, then if it is a red clump giant star it would be located at a distance of ~ 9 Kpc.

3.1.3 Black hole lens candidate

To obtain the mass of the lens we used the equation 2.41. The source, as the CMD shows, is located in the galactic bulge, then we tested two distances: $D_s = 8$ Kpc, where the density of bulge stars peaks along the line of sight, and $D_s = 9$ Kpc in the far side of the bulge. For the lens distance we assumed two cases: the lens is a member of the cluster with a known distance and the lens is not a member, then the distance is unknown.

In the first case, considering that the lens is a member of the cluster we assume $D_d = 6kpc$, and the source is at $D_s = 8kpc$, using a transverse velocity of $V = 220kms^{-1}$ we obtain a mass for the lens of $M_l = 3.5{\pm}0.1M_\odot$, and with $V = 168kms^{-1}$ a mass of $M_l = 2.0{\pm}0.1M_\odot$. If the source is at $D_s = 9kpc$ we obtain $M_l = 2.7{\pm}0.1M_\odot$ and $M_l = 1.5 \pm 0.1M_\odot$ respectively for the two transverse velocity values.

The most suitable characterization for the lens is a black hole, but it would be expected that a massive and old lens is located at the center of the cluster.

In the second case, where the lens is not a member of the NGC 6553, the distance to the lens is unknown, then we assumed three different locations: $D_d =$ 3,4, and 5 kpc. For a source distance of $D_s = 8kpc$ and typical disk velocity of $V = 220kms^{-1}$ we obtain: $M_{3kpc} = 2.8M_\odot$, $M_{4kpc} = 2.6M_\odot$, and $M_{5kpc} = 2.8M_\odot$. For a source at $D_s = 9kpc$ we obtain: $M_{3kpc} = 2.6M_\odot$, $M_{4kpc} = 2.3M_\odot$, and $M_{5kpc} = 2.3M_\odot$.

The masses estimate are larger for a typical disk main sequence star, furthermore if the lens is a main sequence star should be bright enough to be detected at the distance D_d proposed.

3.1.4 Conclusions

We found a microlensing event in the field of the globular cluster NGC 6553. We fit an unblended and a blended model obtaining very similar parameters, that also are in agreement with OGLE estimations. The CMD suggest that the position of the source is in the bulge ($D_s = 8 - 9kpc$). The distance to the cluster is known (D = 6kpc) then, if the lens is a cluster member, we estimate a mass of $M = 1.5 - 3.5M_\odot$, which correspond to a heavy remnant as a black hole.

We studied an alternative case where the lens is located in the disk between $D_d = 3 - 5kpc$. The estimation of the mass also yields massive lens with $M = 2.3 - 2.8M_\odot$. This case looks less likely because the lens would be a bright star, detectable by the surveys.

To predict if the lens is a cluster member we need to wait until the lens moves away from the source star. We know that the relative proper motion of the globular cluster is large, then, if the lens is a stellar object it would be detected but if it remains invisible it is an isolated black hole. The source-lens separation can reach the 60 mas range within 10 year (Zoccali et al. 2001).

Using follow-up observations we could confirm that the lens is a cluster member, this also will confirm that is a black hole remnant. Then, this would be the first detected black hole in a globular cluster and also the oldest stellar black hole detected. If this discovery is validated it will open interesting questions like why this black hole is not in the center of the globular cluster as is expected by dynamical friction, what is the mass distribution of globular cluster black holes, and how much of these objects contribute to the mass in the Milky Way.

3.2 Galactic microlensing events in the VVV Survey

This section is based on the article submitted to the MNRAS: 'Galactic microlensing events in the VVV Survey' by ***K. Rojas****, N. Medina, V. Motta, D. Minniti, J. Borissova, N. Godoy, R. Kurtev, J. Beamín, and A. Melo*

We report 19 microlensing events found in two tiles of the VISTA Variables in the Vía Láctea Survey (VVV). Five of the events are only in the VVV Survey while the other fourteen were independently found by the Optical Gravitational Lensing Experiment (OGLE). Fifteen of these events are in the b309 VVV tile and four in the b296 VVV tile, both regions are located deep within the bulge. We fit the light curves with a simple single-lens model for all the events. Due to incompleteness in the VVV light curves, for only 5 events in both surveys, our estimated parameters are in agreement with those obtained by OGLE. Based on color-magnitude diagrams and proper motion analysis, we estimate that the magnified star (background source) in 10 cases is located in the bulge (i.e. at a distance of 8–9 Kpc). The event VVV-b309-m002 is located in the red clump at a distance of 7.7kpc, which allows us to estimate the lens mass of 0.5-0.7 $M_{\odot}$.

3.2.1 Data reduction

The PSF photometric process is similar to the one described in Section 3.1.1, but include some different steps, in the following I summarize those steps. The photometry was performed in all the available epochs of K_s and J bands for tiles b309 and b296 using the software `Dophot` (Schechter et al. 1993; Alonso-García et al. 2012). The photometric calibration was done following the procedure described by Navarro Molina et al. (2016), where a set of non-variables stars were selected using the aperture photometry catalogs produced by the Cambridge Astronomical Survey Unit (CASU)[2] database. The final magnitude for each source was obtained with the parameters estimated from a 3-σ clipping linear fit. The light-curves were obtained conducting a cross-correlation process among the catalogs created for all the available epochs in K_s-band, using a tolerance of 0.35 arcsec. The extracted light-curves have mean baseline K_s-band magnitudes between $10.8 < K_s < 17.3$, with typical errors for magnitudes fainter than 16 mag between ∼0.09 and 0.13 magnitudes (Medina et al. 2018). The cadence of the light curves is not homogeneous, being in the first epochs ∼9 days and in the last ones ∼1.7 days, mainly is because the yearly bulge observing season runs from April to October.

3.2.2 Detection of microlensing events

Analyzing the tiles b309 and b296 we obtained 2,731,325 light curves for b309 and 2,226,602 for b296. We used the variability index η (von Neumann 1941) to check the independence of successive observations in a light curve (Medina et al. 2018). In this case, we used it to separate the population of transient objects and non-transient ones. When the light curve has uncorrelated normally distributed measurements $\eta \sim 2$ (non-transient objects), and when $\eta \lesssim 1.4$ we have the transient region. We classify the events with $\eta < 0.6$ as "secure" transients, and those with $0.6 < \eta < 1.4$ as "possible" transients (pending on further analysis). The second step is the visual inspection of those objects in the secure region to confirm their status as microlensing events. We identify nine: VVV-b309-m001, VVV-b309-m002, VVV-b309-m003, VVV-b309-m004, VVV-b309-m005, VVV-b309-m006, VVV-b296-m001, VVV-b296-m002, and VVV-b296-m003.

The microlensing detection efficiency is a product of two almost independent

[2]http://casu.ast.cam.ac.uk/vistasp/

effects: the photometric and the sampling efficiencies. Regarding the photometric efficiency, in spite of using different wavelengths, the VVV survey should be comparable to the OGLE and MOA experiments, that also reach faint magnitudes in the bulge, deeper than the red giant clump. But, taking into account that VVV uses K_s band instead of the optical bands used by OGLE, we can observe objects through dusty patches. On the other hand, the VVV sampling efficiency is lower in comparison with the other microlensing experiments because it was designed for variable stars. Thus, the smaller total time coverage (from 2010 to 2015), and the non-optimal cadence of the observations contribute to the reduced number of points in the final light curves.

To assess the efficiency of our detections we cross-correlate the coordinates of all objects in both tiles with OGLE catalog[3], within a radius of 1.0 arc-seconds to account for differences in pixel size seeing and blending. We find 88 OGLE objects in tile b309 and 45 in tile b296, ∼90% of the OGLE total sample. Fourteen of these objects are classified in the "secure" and "possible" regions (i.e. $\eta < 1.4$). Five of them are in the "secure" region (VVV-b309-m002, VVV-b309-m005, VVV-b309-m008, VVV-b296-m001, VVV-b296-m002), and the other 9 are in the "possible" region (VVV-b309-m007, VVV-b309-m009, VVV-b309-m010, VVV-b309-m011, VVV-b309-m012, VVV-b309-m013, VVV-b309-m014, VVV-b309-m015, VVV-b296-m004). Notice that 4 of these 5 objects in the "secure" region where independently detected using η index in VVV light curves, while VVV-b309-m008 was originally discarded in the visual inspection because it is poorly sampled due to its low magnitude ($\sim 17mag$). In total we have light curves for 19 microlensing events, 15 in the tile b309 and 4 in b296 (see Table 3.2 and Figure 3.4).

3.2.3 Ligth curve fitting method

The light curves were fitted using a simple single-lens model (see Equation **??**). We run 10000 Monte Carlo Markov Chain (MCMC) steps using PYMC3 package (Salvatier et al. 2016). We used the Maximum a Posteriori (MAP) method to obtain the posterior distribution, and No-U-Turn Sampler (Hoffman & Gelman 2011, NUTS) as a sampler. A uniform prior was used to constraint the following parameters: the mean baseline magnitude of the source before the magnification (K_s), the impact

[3]http://ogle.astrouw.edu.pl/ogle4/ews/ews.html

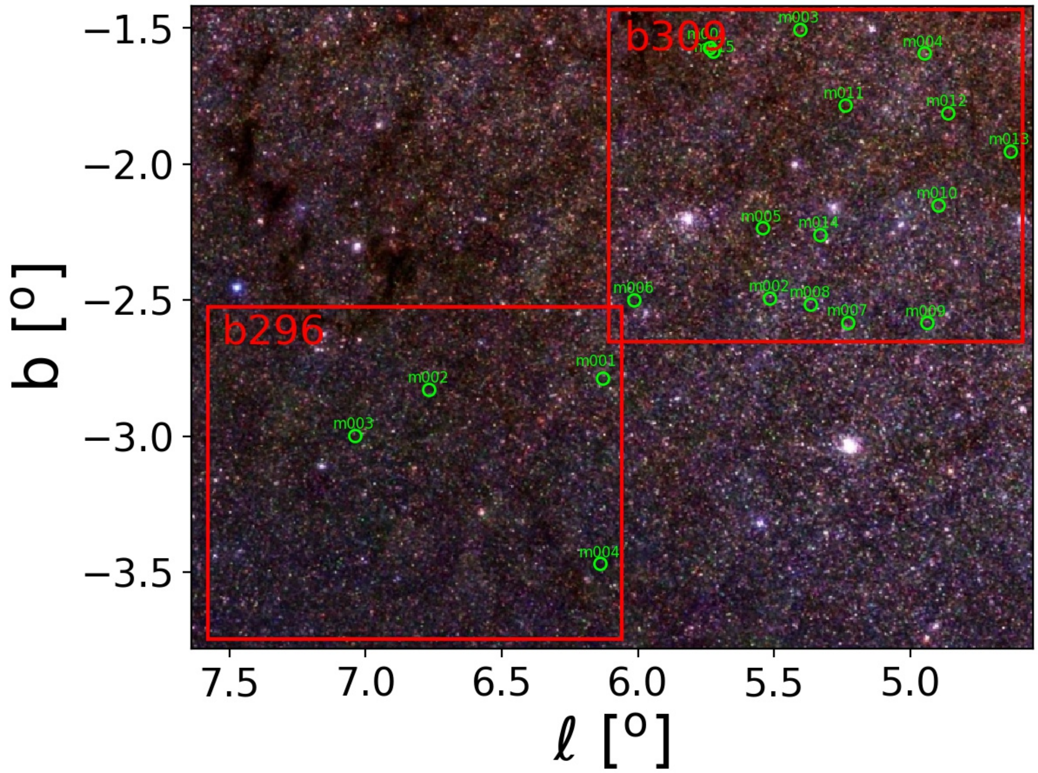

Figure 3.4: Spatial distribution of the detected microlensing events through the field (green circles). The red squares represent the footprint and location of each tile with dimensions 1.2x1.5 degrees. The background image is a false color image composite 2MASS survey (Skrutskie et al. 2006) for our field of view (taken from Aladin sky atlas survey Bonnarel et al. (2000)).

parameter (u_0), the time of the maximum magnification by the lens (T_0), and the Einstein crossing scale (T_E). The search of each parameter was done in intervals, u_0 in the range 0.05-1.5, and T_E in 10-200 days range. In the case of K_s, we distinguish two cases: i) if the difference between the minimum and maximum magnitude is less than 2 magnitudes, we took the mean magnitude and used a ± 1.0 magnitude range, ii) otherwise we took the minimum magnitude and used ± 0.5 magnitude range. The limits for T_0 are ± 100 days around the maximum magnification. The confidence contour and the marginalized 1-dimensional posterior probability distributions (PDFs) on the parameters are shown in the appendix material. The mean of the distribution of each parameter and its error at 3σ are presented in Table 3.3, the best fits are shown in Figures 3.24, 3.25 and 3.26.

For all the events originally detected in the "secure" region (9), the fitting proce-

Table 3.2: Microlensing events detected in VVV K_s-band.

Event	OGLE ID	Ra (deg)	Dec (deg)	ℓ (deg)	b (deg)	Tile	A_k (mag)	Epochs
VVV-b309-m001	–	271.1791	-24.7968	5.72273	-1.58577	b309	0.262 ± 0.102	171
VVV-b309-m002	2015-BLG-1502	271.9420	-25.4187	5.51600	-2.49199	b309	0.268 ± 0.117	245
VVV-b309-m003	–	270.9317	-25.0352	5.40483	-1.50712	b309	0.449 ± 0.141	202
VVV-b309-m004	–	270.7674	-25.4750	4.94854	-1.59391	b309	0.496 ± 0.208	173
VVV-b309-m005	2014-BLG-1745	271.7084	-25.2708	5.54289	-2.23560	b309	0.234 ± 0.102	247
VVV-b309-m006	–	272.2139	-24.9859	6.01431	-2.49788	b309	0.221 ± 0.103	235
VVV-b309-m007	2014-BLG-1744	271.8735	-25.7134	5.22803	-2.58083	b309	0.573 ± 0.165	157
VVV-b309-m008	2015-BLG-1581	271.8822	-25.5613	5.36501	-2.51395	b309	0.204 ± 0.103	131
VVV-b309-m009	2015-BLG-1653	271.7211	-25.9665	4.93990	-2.58374	b309	0.236 ± 0.121	170
VVV-b309-m010	2014-BLG-1593	271.2779	-25.7921	4.89788	-2.15052	b309	0.352 ± 0.128	143
VVV-b309-m011	2012-BLG-1065	271.1088	-25.3146	5.23989	-1.78380	b309	0.450 ± 0.178	213
VVV-b309-m012	2015-BLG-1583	270.9323	-25.6579	4.86235	-1.81337	b309	0.550 ± 0.187	236
VVV-b309-m013	2014-BLG-1366	270.9426	-25.9263	4.63298	-1.95318	b309	0.686 ± 0.231	243
VVV-b309-m014	2014-BLG-1697	271.6184	-25.4666	5.33211	-2.25983	b309	0.303 ± 0.114	123
VVV-b309-m015	2012-BLG-1041	271.1752	-24.7802	5.73539	-1.57456	b309	0.579 ± 0.163	159
VVV-b296-m001	2014-BLG-1018	272.5526	-25.0242	6.12890	-2.78527	b296	0.188 ± 0.107	195
VVV-b296-m002	2015-BLG-0684	272.9309	-24.4846	6.76794	-2.82752	b296	0.225 ± 0.117	225
VVV-b296-m003	–	273.2375	-24.3265	7.04069	-2.99704	b296	0.367 ± 0.112	211
VVV-b296-m004	2012-BLG-0839	273.2190	-25.3435	6.13742	-3.46756	b296	0.578 ± 0.162	240

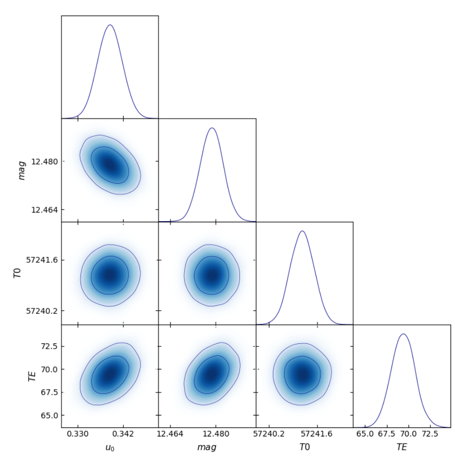

Figure 3.5: Event VVV-b309-m001

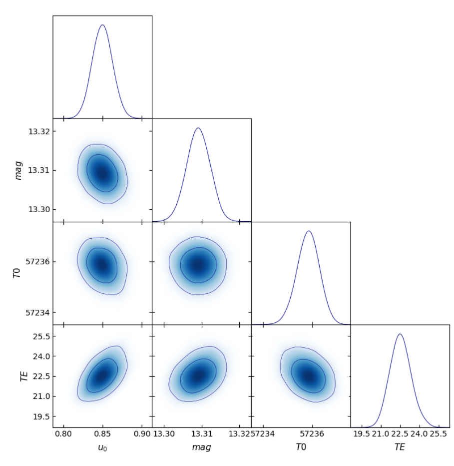

Figure 3.6: Event VVV-b309-m002

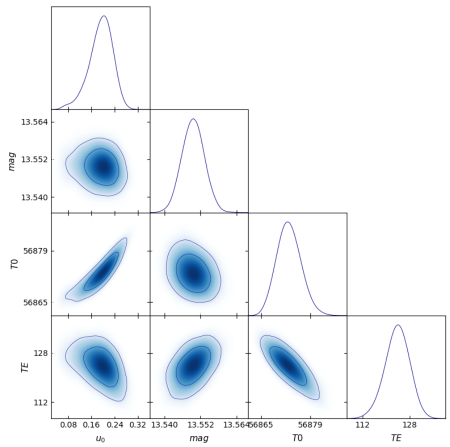

Figure 3.7: Event VVV-b309-m003

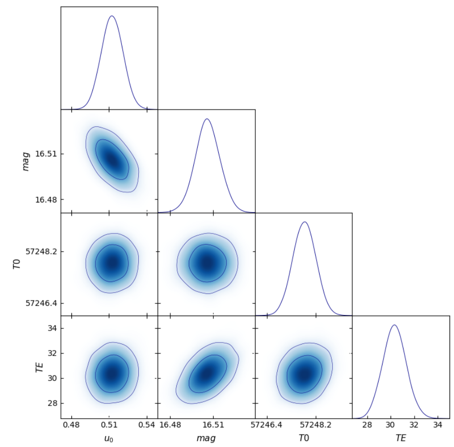

Figure 3.8: Event VVV-b309-m004

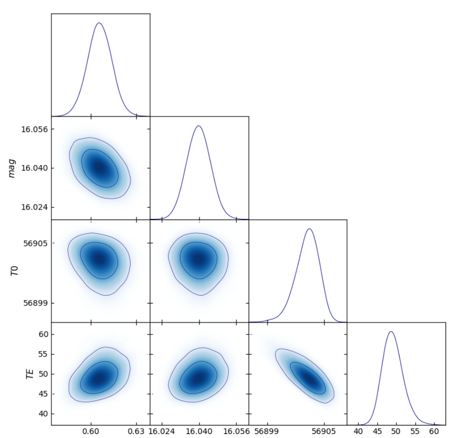

Figure 3.9: Event VVV-b309-m005

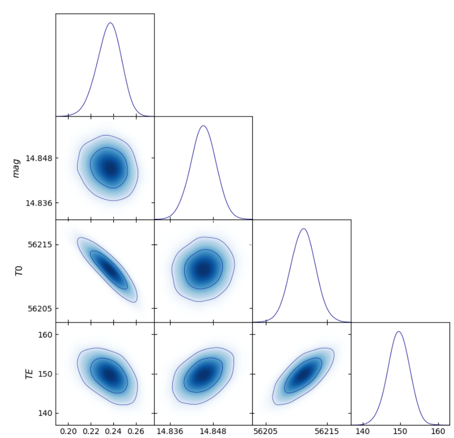

Figure 3.10: Event VVV-b309-m006

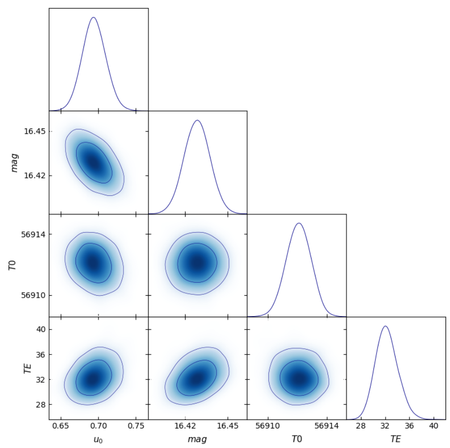

Figure 3.11: Event VVV-b309-m007

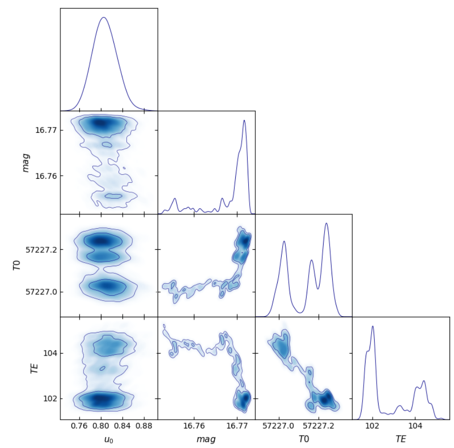

Figure 3.12: Event VVV-b309-m008

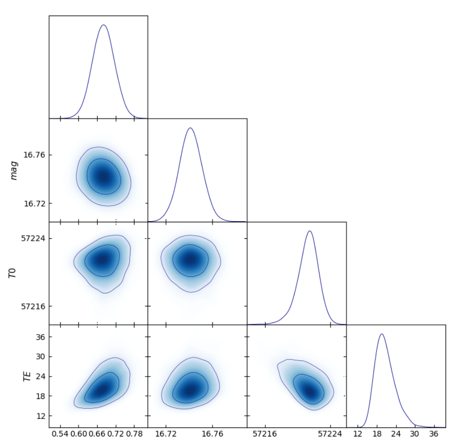

Figure 3.13: Event VVV-b309-m009

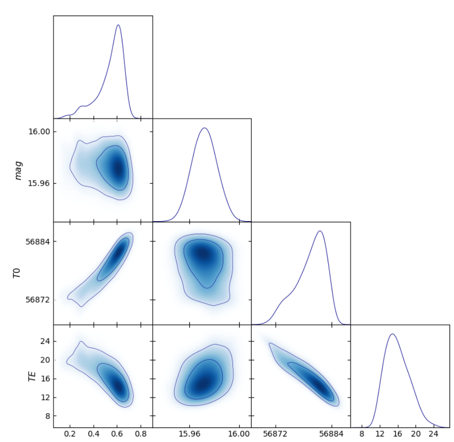

Figure 3.14: Event VVV-b309-m010

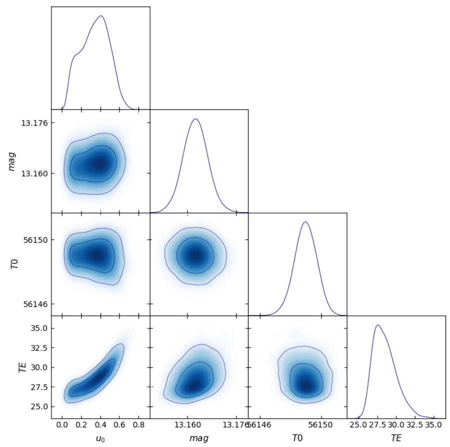

Figure 3.15: Event VVV-b309-m011

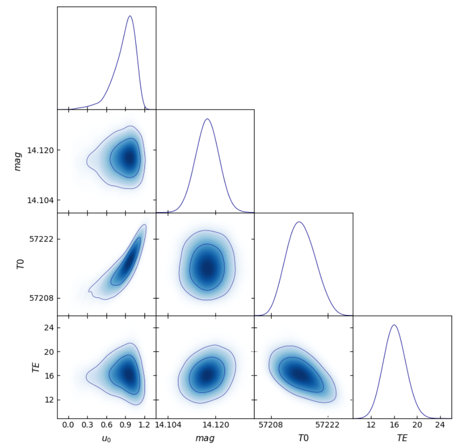

Figure 3.16: Event VVV-b309-m012

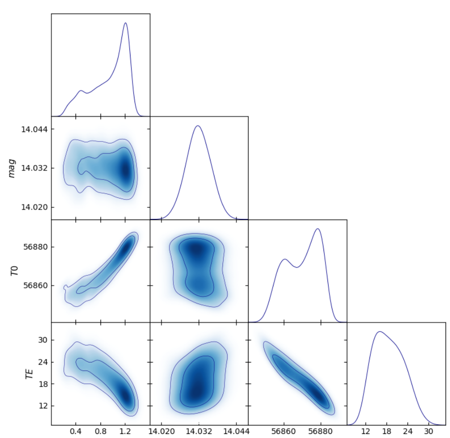

Figure 3.17: Event VVV-b309-m013

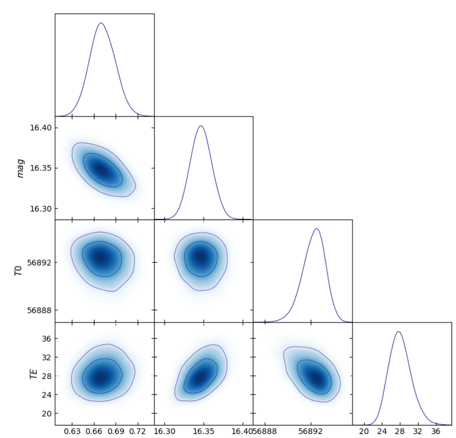

Figure 3.18: Event VVV-b309-m014

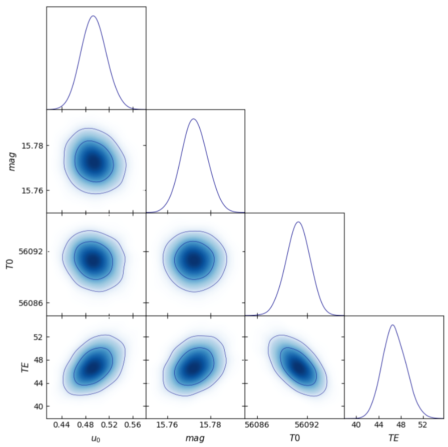

Figure 3.19: Event VVV-b309-m015

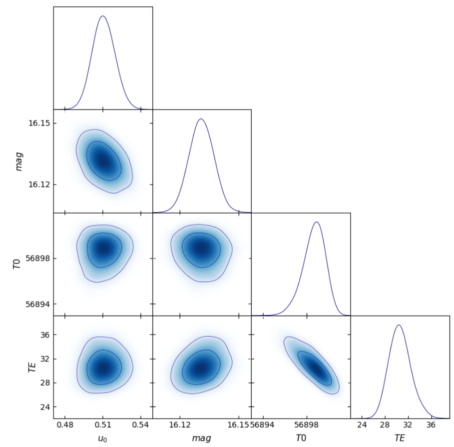

Figure 3.20: Event VVV-b296-m001

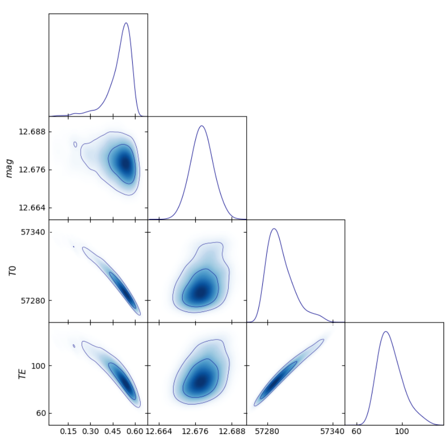

Figure 3.21: Event VVV-b296-m002

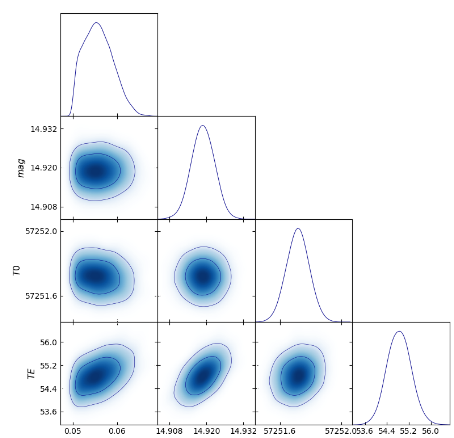

Figure 3.22: Event VVV-b296-m003

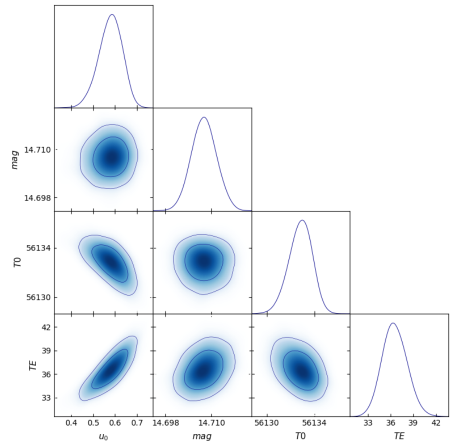

Figure 3.23: Event VVV-b296-m004

Table 3.3: Simple single-lens model

Event	K_s[a]	u_0	T_0 (JD)	T_E (days)
VVV-b309-m001	12.479 ± 0.009	0.34 ± 0.01	57241 ± 1	69 ± 3
VVV-b309-m002	13.309 ± 0.007	0.85 ± 0.03	57236 ± 1	23 ± 3
VVV-b309-m003	13.550 ± 0.008	0.19 ± 0.10	56873^{+9}_{-6}	124 ± 9
VVV-b309-m004	16.506 ± 0.009	0.51 ± 0.02	57248± 1	30 ± 2
VVV-b309-m005	16.040 ± 0.010	0.61 ± 0.02	56903 ± 3	49^{+8}_{-5}
VVV-b309-m006	14.845 ± 0.008	0.24 ± 0.02	56211 ± 5	150 ± 7
VVV-b309-m007	16.428 ± 0.020	0.69 ± 0.04	56912 ± 2	32 ± 5
VVV-b309-m008	$16.841\ ^{0.04}_{0.02}$	$0.23^{+0.03}_{-0.21}$	57218^{+7}_{-1}	17^{+8}_{-1}
VVV-b309-m009	16.742 ± 0.020	0.68 ± 0.08	57221 ± 3	21^{+10}_{-5}
VVV-b309-m010	15.972 ± 0.020	$0.54^{+0.13}_{-0.33}$	56879^{+5}_{-8}	16^{+8}_{-4}
VVV-b309-m011	13.163 ± 0.009	0.34± 0.30	56149 ± 2	29^{+4}_{-2}
VVV-b309-m012	14.117 ± 0.009	$0.88^{+0.25}_{-0.54}$	57215^{+8}_{-7}	16 ± 4
VVV-b309-m013	14.032 ± 0.009	$0.95^{+0.31}_{-0.76}$	56870^{+14}_{-19}	19^{+11}_{-7}
VVV-b309-m014	16.347 ± 0.030	0.67 ± 0.04	56892 ± 2	28^{+7}_{-4}
VVV-b309-m015	15.773 ± 0.010	$0.49^{+0.05}_{-0.04}$	56091 ± 3	47^{+5}_{-4}
VVV-b296-m001	16.131 ± 0.010	0.51 ± 0.02	56899 ± 3	31 ± 5
VVV-b296-m002	12.678 ± 0.008	$0.50\ ^{0.09}_{0.30}$	57292^{+40}_{-16}	90^{+33}_{-17}
VVV-b296-m003	14.919 ± 0.008	0.06 ± 0.01	57251.7 ± 0.2	55 ± 1
VVV-b296-m004	14.708 ± 0.007	0.58± 0.12	56133 ± 2	37 ± 4

[a]Mean baseline magnitude of the source in K_s band.

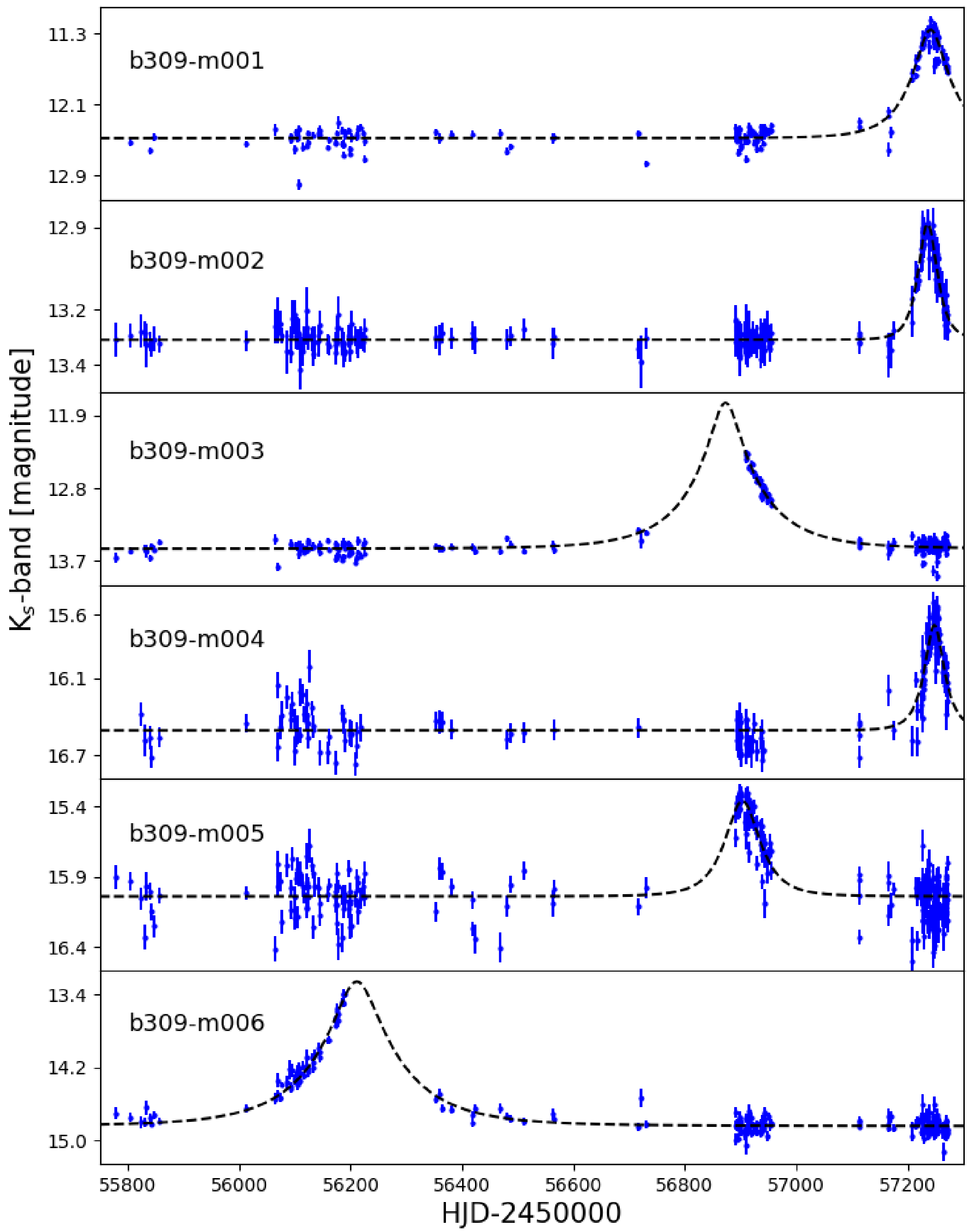

Figure 3.24: Simple Single-lens model fit for the microlensing events in b309 VVV tile. The gray points are the measurements and their associated photometric errors. The blue line shows the the best fit model.

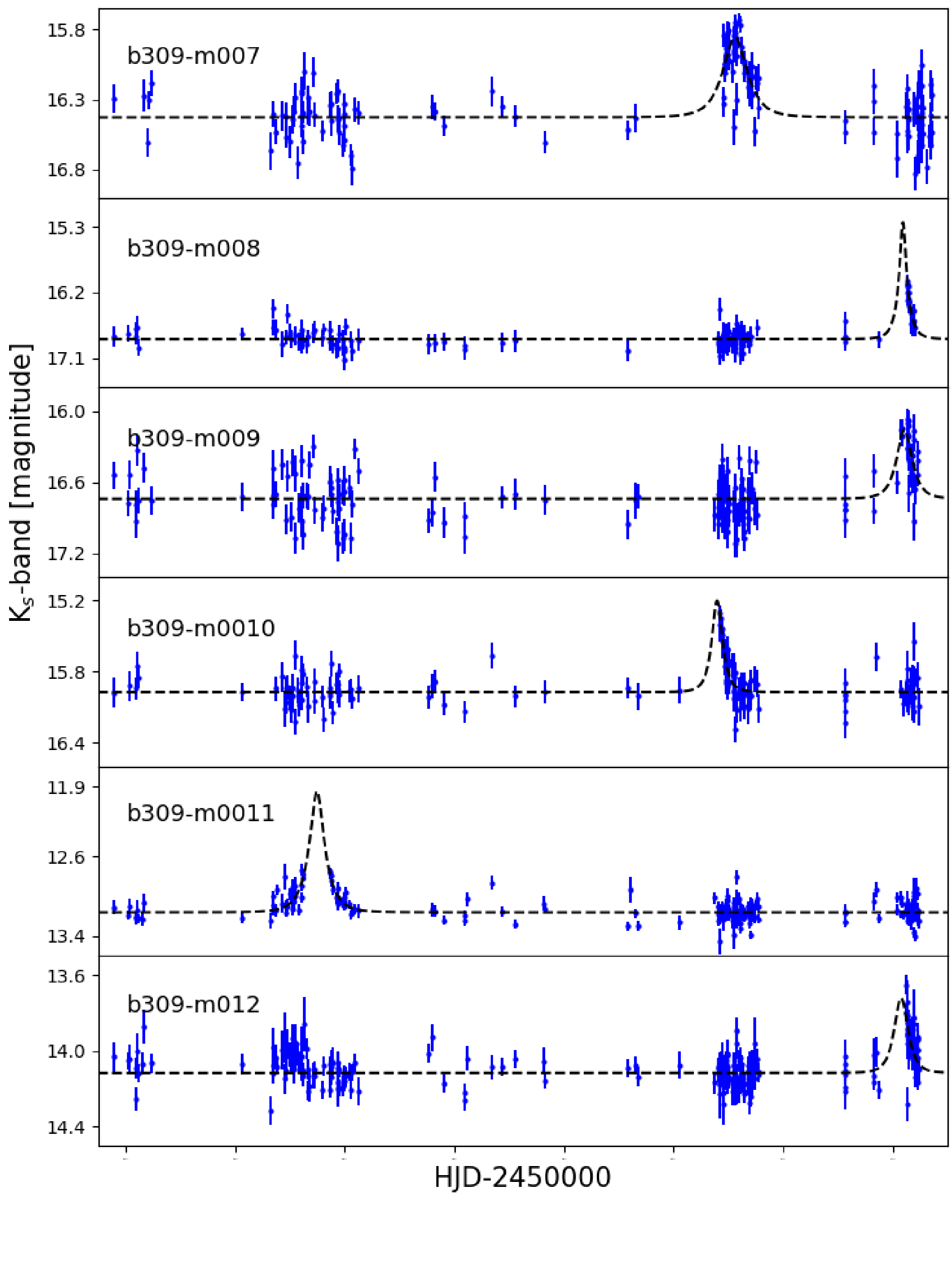

Figure 3.25: continuation of figure 3.24: Simple model fit for the microlensing events in b309 VVV tile.

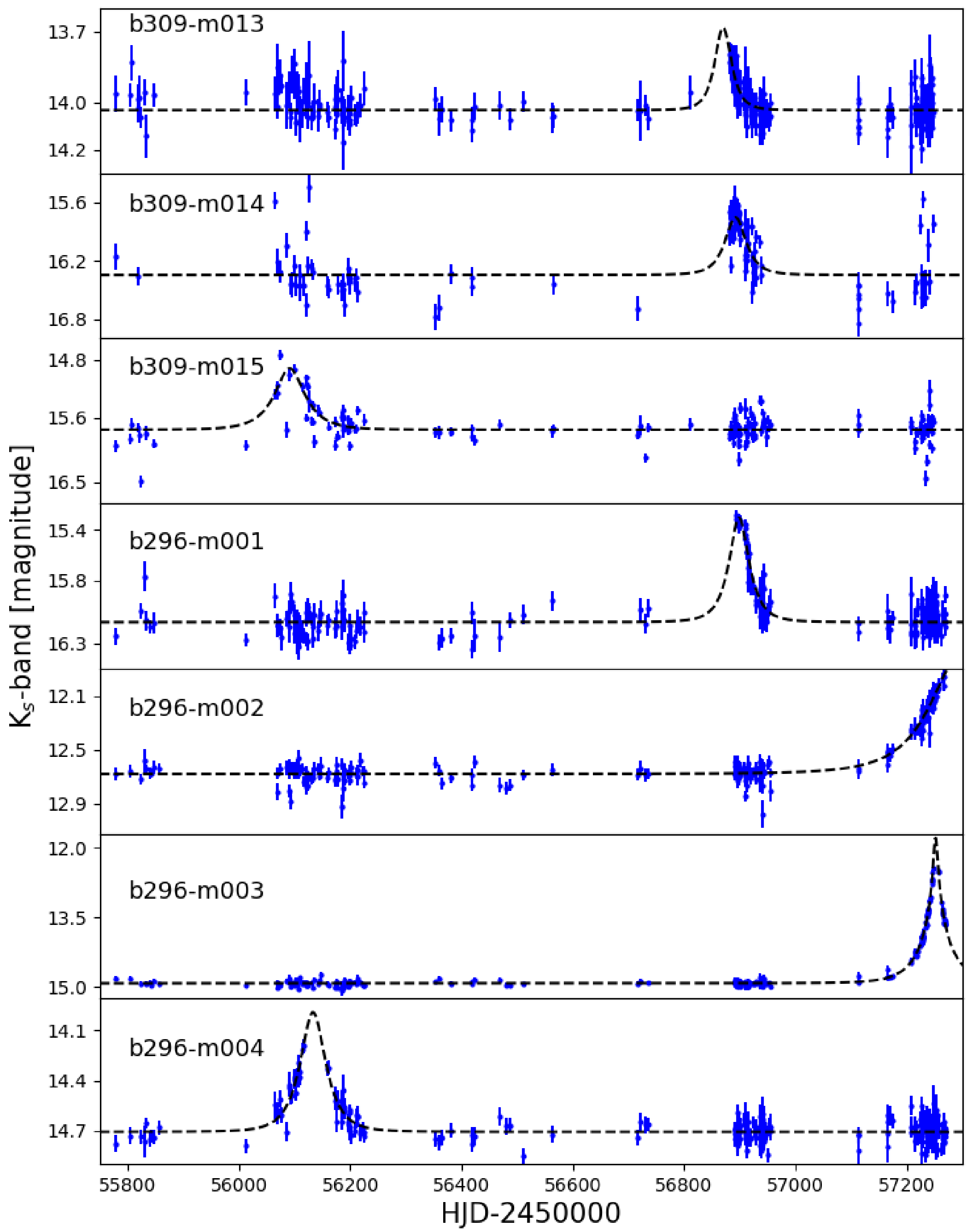

Figure 3.26: continuation of figure 3.25: Simple model fit for the microlensing events in b309 and b296 VVV tiles.

dure yield well constrained parameters at 3σ, with the exception of VVV-b296-m002. For the events in the "possible" region (10), 6 have well constrained parameters while 4 present some difficulties associated with the light curve incompleteness (see appendix). In the case of VVV-b309-m008 the fit was not reliable because, as it was explained before, this light curve it is very incomplete, thus we discard this event for further analysis.

3.2.4 Extinction and position in the galaxy

We took the well constrained events in the "secure" region to investigate the location of source stars. We analyzed the lensed star positions on the proper motion (PMD) and color-magnitude (CMD) diagrams, shown in Figure 3.27 and Figure 3.28 respectively. The precise proper motions are taken from the Gaia Data Release 2 (DR2) (Gaia Collaboration et al. 2016, 2018) and the VVV InfraRed Astrometric Catalogue - VIRAC (Smith et al. 2018). There are no proper motion data for all of the lensed stars because some of them are faint and reddened due to the high interstellar extinction near to the Galactic plane and bulge. In Gaia DR2 we found data for 5 of the 9 objects: VVV-b309-m002, VVV-b309-m003 VVV-b309-m006, VVV-b296-m002, and VVV-b296-m003. In VIRAC there are proper motions for 7 of the objects: VVV-b309-m001, VVV-b309-m002, VVV-b309-m003, VVV-b309-m005, VVV-b309-m006, VVV-b296-m002, and VVV-b296-m003.

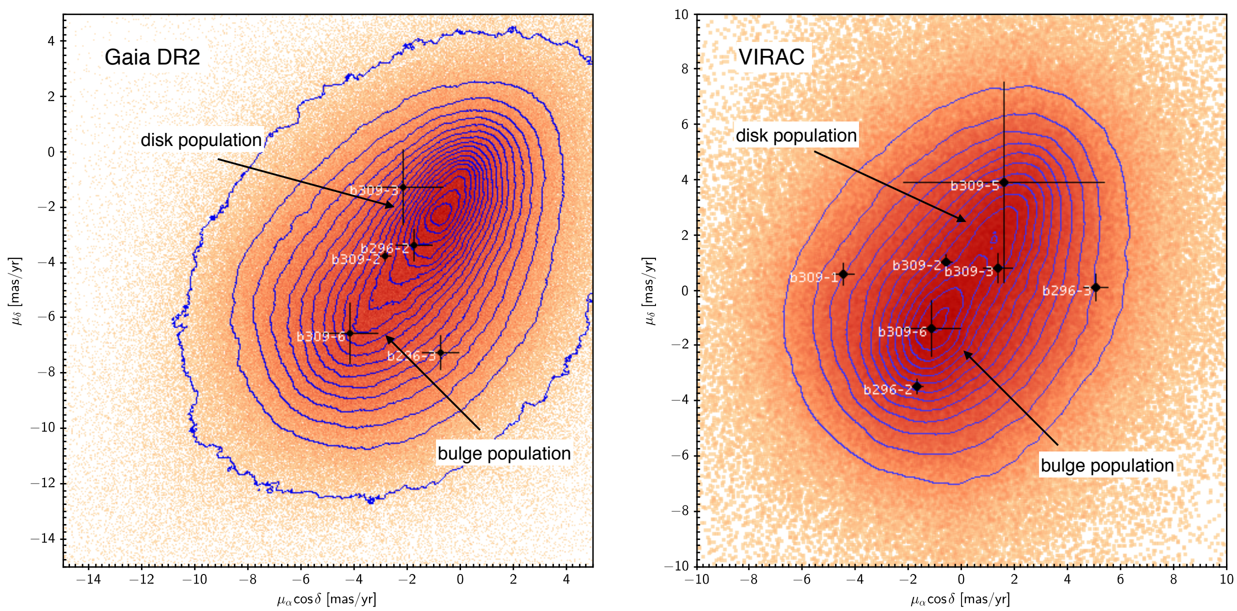

Figure 3.27: **Left panel** The Gaia DR2 ($\mu_\alpha \cos\delta, (\mu_\delta)$ proper motion diagram of the area covered by the VVV tiles b296 and b309. **Right panel** The VIRAC proper motion diagram of the same area. The proper motions of the lensed stars are given together with their designations. The crosses represent 1σ proper motion errors. On both panels the populations of the disk and the bulge stars are well visible and separated. The curves of the constant stellar densities are also plotted. The positions of the stellar populations in both diagrams are slightly shifted because of the differences in the zero points of Gaia DR2 and VIRAC. Gaia is in the absolute coordinate system and VIRAC still offers relative proper motions.

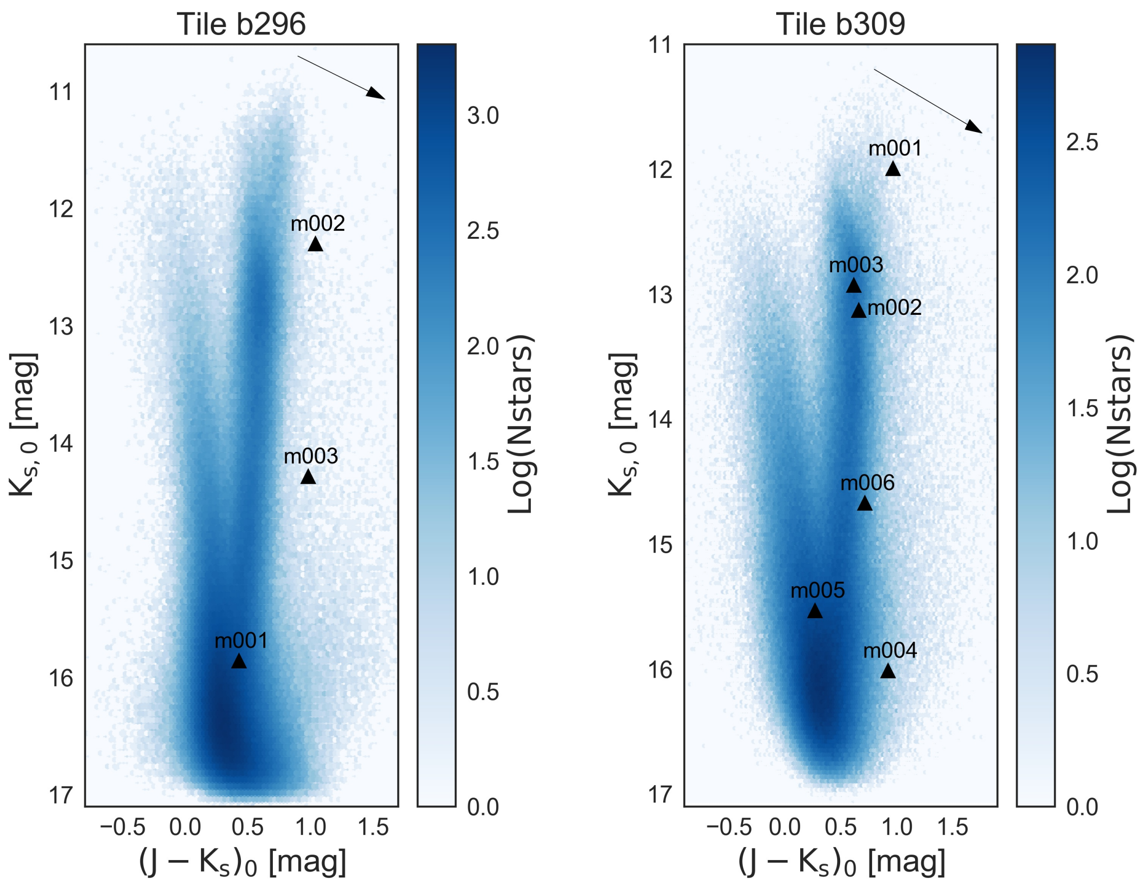

Figure 3.28: Corrected color-magnitude diagram for each tile using the extinction maps. With this correction, the sources move up and to the left. The black symbols are the 9 microlensing events obtained using the η index. The black vectors upper right represent the reddening vectors, that shows where the magnitude will move without extinction correction.

The J_0-K_{S_0} vs K_{S_0} dereddened CMD, shows the position for the 9 objects. The reddening vectors, shown in the upper right part, represent the shifted magnitude due by extinction. It was constructed using the extinction maps from Gonzalez et al. (2012) (based on the extinction law from Nishiyama et al. (2009)), that provides an average A_{K_s} value for each tile. For tile b309, this value is $< A_{K_s} > = 0.441$ mag, and for b296 is $< A_{K_s} > = 0.299$ mag. Once these extinction corrections are applied, the CDMs depict a narrower and bluer distribution of the stellar population (Gonzalez et al. 2011). Figure 3.28 shows the separation between the population in the disk and the bulge: the left branch represents the disk main sequence and the right one the Red Giant Branch (RGB), with an over-density corresponding to the Red Clump

(RC).

Combining the information from the PMDs and CMDs we can conclude that the stars VVV-b309-m001, VVV-b309-m006, VVV-b296-m002 and VVV-b296-m003, belong to the bulge population. The stars VVV-b309-m002 and VVV-b309-m003 stay in the intermediate zone between the disk and the bulge populations on the PMDs, but on the CMD they likely belong to the RC. We cannot make any definitive conclusion about VVV-b309-m005 because the proper motion error is high and the position on the CMD is also in the intermediate zone between the bulge and the disk. In the case of VVV-b296-m001 the result is inconclusive because we have no PMD information and the CDM place it in the intermediate region. Finally, in spite of lacking PMD information for the case of VVV-b309-m004 the CDM show that it likely belong to the bulge.

3.2.5 Discussion

For those events that have OGLE counterpart (14), we compared the obtained parameters in our data and those published by OGLE. For 12 events our estimation of the parameter T_0 is in agreement, within errors (3σ), with those estimated by OGLE. For the two cases in disagreement we found difference of ~6 days (VVV-b309-m014) and ~10 days (VVV-b309-m015). The T_E parameter is more sensitive than T_0 to the heterogeneous cadence of our sample, therefore we only have agreement within errors (3σ) for 10 events. On the other hand, the T_E values obtained for VVV-b309-m008, VVV-b309-m014, VVV-b296-m001, and VVV-b296-m004 do not agree with those in OGLE. The most sensitive parameter is u_0, we found agreement for: VVV-b309-m002, VVV-b309-m010, VVV-b309-m011, VVV-b309-m013, VVV-b296-m002, where only VVV-b309-m002 and VVV-b296-m002 shows PDFs that converge to a single value. The rest of the events do not agree with OGLE results, mainly because most of them have incomplete light curves where the maximum and/or a wind is missing. Two events in the "secure" region are in disagreement (VVV-b309-m008 and VVV-b296-m001). In the first case as we mentioned before, the parameters do not converge to a single value thus the fit to our VVV light curve is unreliable. In the second case for the event VVV-b296-m001, which corresponds to OGLE 2014-BLG-1018[4], our data cover the final part of the event, missing the perturbation produced

[4]http://ogle.astrouw.edu.pl/ogle4/ews/2014/blg-1018.html

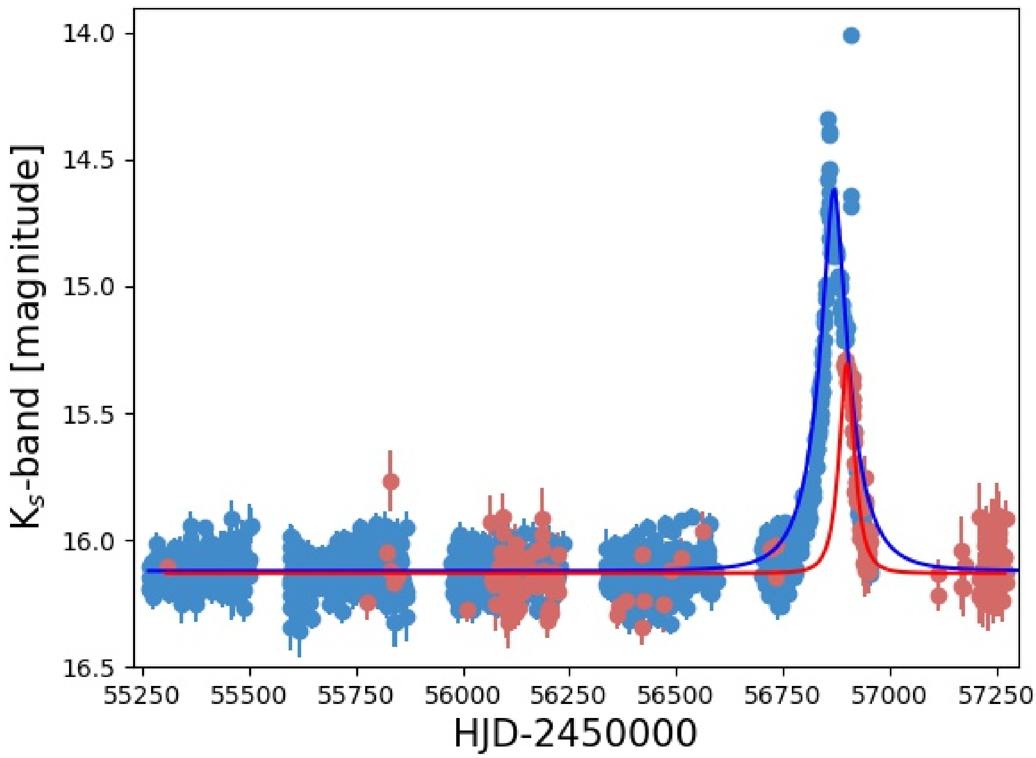

Figure 3.29: Light curve for the event VVV-b296-m001 (OGLE-2014-BLG-1018). OGLE data (blue) was shifted 2.59 magnitudes to match with VVV data (red). The solid lines are the fits presented by OGLE (blue) and ours (red).

by a planet. Then, our simple single-lens model estimate for $t_E = 31 \pm 5$ days, which is less than half the value obtained by the complete light curve used by OGLE.

From the PMs and CMDs we concluded that the source stars in VVV-b309-m002 and VVV-b309-m003 are located in the RC, which can be utilized as a distance indicator (Gonzalez et al. 2011). First, we apply a color-magnitude cut in the data of the tile b309: $1.5 > (J_0 - K_{s_0}) > 0.5$ and $15 > K_{s_0} > 12$. Then, we used the K_{s_0} subsample histogram to identify two RC, with our microlensing events located nearby to the brightest one. We fitted two Gaussians, obtaining an apparent magnitude for that RC of $m^{RC}_{K_s} = 12.91 \pm 0.04$. Assuming a stellar population with a solar metallicity of 10Gyrs, we obtain a RC intrinsic magnitude of $M^{RC}_{K_s} = -1.55$ and a distance $d^{RC}_s = 7.78 \pm 0.06$ Kpc. Only VVV-b309-m002 has a reasonably complete light curve to provide reliable parameters. Thus, we use our results, assuming the source is at $d_s^{RC} = 7.78 \pm 0.06$ Kpc and the lens is located in the disk, with a range of possible distances D_d = 2-6 kpc. The transverse velocity was set as V=220 km/s, estimated from the Galaxy disk rotation (Paczynski 1991). We obtain a range of masses for the lens using Equation **??**, with a minimum value of 0.5 $M_\odot$ (at D_d = 3.9 Kpc), and a maximum one of 0.7 $M_\odot$ (at D_d = 5.9 Kpc). This range of masses indicates that the lens is likely a white dwarf (Kepler et al. 2007).

Table 3.4: Total number of VVV microlensing events

Field	RA(J2000)	DEC(J2000)	Longitude	Latitude	R_{GC} (deg)	Nb ($K_s < 16$)	N_{all}
b296	273.2473	-24.6025	6.80204	-3.13666	7.5	4	4
b309	271.4093	-25.3632	5.33034	-2.04451	5.7	15	9
b332	265.0755	-30.5373	358.031	0.13982	1.0	42	48
b333	265.9633	-29.2980	359.490	0.13988	0.5	78	84
b334	266.8297	-28.0530	0.94855	0.13988	1.0	42	52

The present work also serves as useful comparison for the microlensing results in the Galactic center recently published by Navarro et al. (2017). Their search was made using similar PSF photometry on VVV NIR images, and share similar photometric and sampling efficiencies. Therefore, it is fair to directly compare the total number of VVV microlensing events discovered by both searches in the different fields at different distances from the Galactic center (Table 3.4). Such comparison is very basic, but it shows that the number of microlensing events (and consequently the optical depth) in the Galactic center fields is much larger than those on other bulge fields located at intermediate latitudes and longitudes. This may be due to three different factors, each of them interesting in their own right. First, the Galactic center fields are the densest regions of the bulge. Second, the fact that they are located in the plane of our Galaxy and therefore the number of disk events is maximized. Finally, there may be more heavy remnants (e.g. black holes, neutron stars) closer to the Galactic center. Which one of these factors is dominant remains to be determined through adequate modeling of the optical depth in the near-IR. Regardless, it appears that the microlensing optical depth in the near-IR keeps rising all the way to the Galactic center (Navarro et al. 2017).

3.2.6 Conclusions

We analyzed 19 microlensing light curves, 15 in the tile b309 and 4 in the tile b296 of VVV survey. Nine of these events are considered "secure" detection using η index. Five of them are new events discovered by VVV with no OGLE counterpart.

Using a simple single-lens model we fitted the 19 microlensing light curves. For the nine events found by the variability index η we obtained well constrained parameters. We compared the parameters obtained for our 14 VVV events with those published by OGLE. We found that 5 events have a good agreement within errors with those presented by OGLE, but only VVV-b309-m002 and VVV-b296-m002 show well constrained parameters.

The PMs and CMDs help us to pinpoint the location of the source stars for the events in the "secure" region. We found that VVV-b309-m001, VVV-b309-m006, VVV-296-m002 and VVV-b296-m003 sources are likely located in the bulge. Furthermore, we determined that VVV-b309-m002 and VVV-b309-m003 are located in the red clump, which allows to estimate a distance for those sources of d=7.78 $\pm$ 0.06 Kpc. As we obtained well constrained parameter only for VVV-b309-m002 we used the source distance and assumed an interval for the lens of D_d=2-6kpc, then we estimated a lens mass range of M_{lens}=0.5-0.7 $M_{\odot}$, characteristic of a white dwarf.

By design the VVV survey is optimized for variable star searches like RR Lyrae and Cepheids. We conclude that, in spite of the relatively small number of epochs, the VVV microlensing search is successful. It is clear, however, that our survey is much less effective than the MOA and OGLE searches, which are specifically tailored for microlensing. The VVV survey still allows us to explore microlensing in very crowded and very reddened regions of the Milky Way as confirmed by the comparison with similar searches towards more crowded tiles in VVV survey (Navarro et al. 2017).

Chapter 4

Microlensing in strong lensed quasars

In this chapter I present all the results of the studies related to lensed quasars. In section 4.1 I will present the analysis of the spectra of 6 systems and, in those cases with chromatic microlensing, estimate the size and temperature profile of the emitting region. The results were published in: Rojas et al. (2014), Motta et al. (2017), and Rojas et al. in prep (b). In section 4.2 I will present the results related to the COSMOGRAIL collaboration aimed to measure the time delay in lensed quasars and quantify the microlensing effect into light curves and its error in the estimation of the Hubble constant. These results were published by Courbin et al. (2018) and Bonvin et al. (2018). In section 4.3 I will show the results related to the search and confirmation of new lensed quasar candidates in the collaboration STRIDES.

4.1 Spectroscopic analysis of quasar microlensing

We used spectroscopic data of the gravitational lensed systems HE0047-1756(AB), SDSS1155+6346(AB), HE2149-2745(AB), SDSS0924+0219(BC), Q1355-2257(AB), and SDSS1029+2623(BC) to analyze microlensing and extinction in the observed components (Figure 4.1). We detected chromatic microlensing effect and/or differences in the broad emission line profile in the five first systems. We use magnification maps (see Section 4.1.3) to simulate microlensing and model the emitting region as

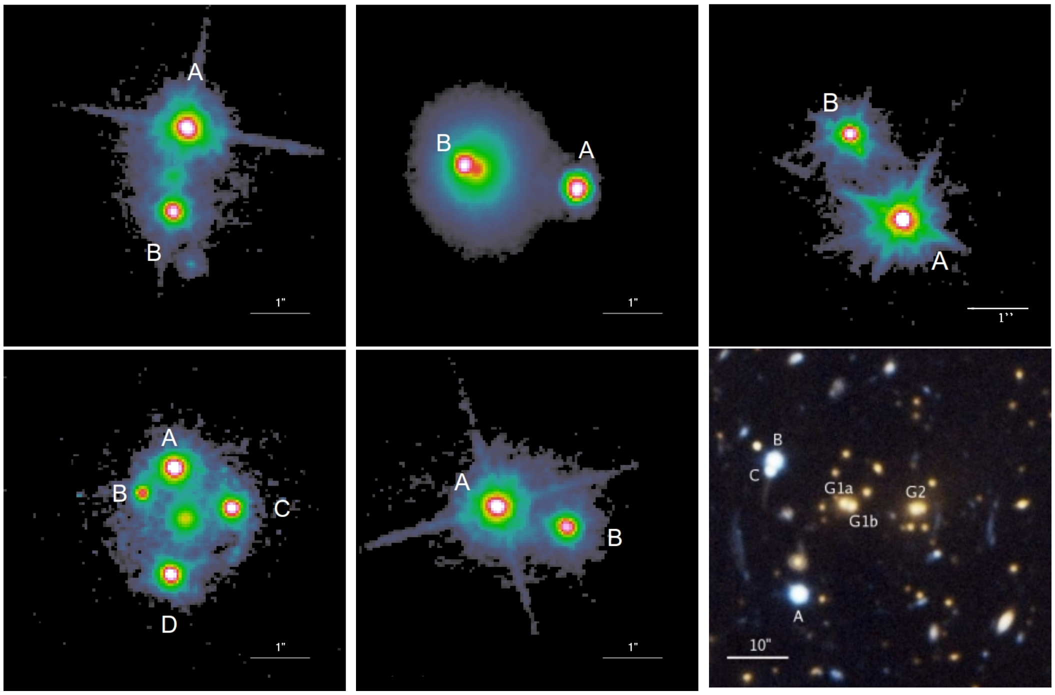

Figure 4.1: Image of each gravitational lens system observed. The components of the quasar are labeled following the astrometry presented in CASTLE. Top: HE0047-1756 (left), SDSS1155-6346 (middle), HE2149-2745 (right). Bottom: SDSS0924+0219 (left), Q1355-2257 (middle), SDSS1029+2623 (right). All the images were taken from CASTLE data base and correspond to band F555W from HST telescope, with the exception of SDSS1029+2623, which is a composite image produced from the Keck g and R bands, and was taken from Oguri et al. (2006).

a Gaussian intensity profile with size $r_s \propto \lambda^p$, obtaining probability density functions. We obtain values for the sizes and temperature profiles with 1σ. In general, we found sizes larger than those predicted by thin disk theory (Shakura & Sunyaev 1973). The systems HE2149-2745 and SDSS0924+0219 show an estimation for p that is significantly smaller (< 0.7) than the theoretical prediction (4/3), while the estimation for SDSS1155+6346, Q1355-2257 and HE0047-1756 are in agreement with the theory, within errors. On the other hand, SDSS1029+2326 spectra shows no microlensing, but there is extinction probably produced by a galaxy in the vicinity of image C. Fitting a extinction curve to the data, we estimate $\Delta E = 0.35 \pm 0.09$, $\Delta M_0 = 1.0 \pm 0.1$ and $R_v = 4.2 \pm 0.5$. Using the parametrized extinction law with $R_v = 3.1$ we obtain $\Delta E = 0.18 \pm 0.01$ and $\Delta M_0 = 1.24 \pm 0.03$, which is in agreement with previous results.

4.1.1 Introduction

This effect is size sensitive, producing large magnifications of sources with angular size comparable to (or smaller than) the microlens Einstein radius, then the flux of inner regions as the accretion disk can be affected by microlensing, and larger regions like the Narrow Line Region (NLR) are not affected. Shakura & Sunyaev (1973) theoretical work shows that the size of the accretion disk (r_s) varies with wavelength ($r_s \propto \lambda^p$), and this can produce chromatic variations (Wambsganss & Paczynski 1991; Wisotzki et al. 1995; Mosquera et al. 2009; Mediavilla et al. 2011), that means that the flux variation is stronger for shorter wavelengths and almost negligible in IR.

Probing this theory is a big challenge because this region has a small size and it is not resolvable with current observational facilities, then indirect observational evidence is needed, like reverberation mapping, that requires monitoring campaigns in multiple wavelength (Wanders et al. 1997; Collier et al. 1998; Edelson et al. 2015), or chromatic microlensing which uses single-epoch spectra (Bate et al. 2008; Floyd et al. 2009; Sluse et al. 2012; Motta et al. 2012; Guerras et al. 2013b; Jiménez-Vicente et al. 2014; Rojas et al. 2014; Mediavilla et al. 2015; Motta et al. 2017).

The magnification of the accretion disk is not the only cause of chromatic variations in the flux of the QSO images. Intrinsic variability of the source coupled with time delay and dust extinction also introduce chromatic variations. Then, as was mentioned in Section 2.6.2 special care is required to distinguish among microlensing, chromaticity, and differential dust extinction along the path of each image through the lens galaxy.

4.1.2 Observations and data reduction

We obtained IMACS Long-Camera/Magellan spectra for HE0047-1756 in 2008, Blue Channel Spectrograph/MMT spectra for SDSS1155+6346 in 2010 (P.I. E. Falco), VLT/FORS2 spectra for HE2149-2745, SDSS0924+0219 and Q1355-2257 in 2008 (P.I. V. Motta, 381.A-0508(A)). The log of the observations is in Table 4.1. In the case of Q1355-2257, we additionally used the deconvolved spectra from Sluse et al. (2012) provided by the VizieR[1] catalog (Ochsenbein et al. 2000). The spectra of SDSS J1029+2623 were observed with the LRIS-ADC at Keck. Reduced spectra

[1]Based on data obtained with the VizieR catalog access tool, CDS, Strasbourg, France.

were kindly provided by M. Oguri (private communication). The details related to the observation and data reduction are explained in Oguri et al. (2008).

Table 4.1: Log of observations

Object	Pair[a]	Δ[b]	Instrument	Grating	Date	Airmass	P.A.[c]	Seeing[d]	Exposure[e]
HE0047-1756	AB	1.43	Baade 6.5m/IMACS	300	2007-dec-10	1.03	-62.9	0.6	X×1200
SDSS1155+6346	AB	1.94	MMT/Blue Channel	300	2008-Mar-19	1.18	124.9	0.7	X×1800
HE2149-2745	AB	1.7	VLT/FORS2	300	2008-May-07	1.38	-28.6	0.8	3×300
					2006-Aug-04	1.48	-32	0.6	6×1400
SDSS0924+0219	BC	1.1	VLT/FORS2	300	2008-Apr-02	1.12	42	0.8	10×1800
Q1355-2257	AB	1.18	VLT/FORS2	300	2008-Apr-02	1.06	-72	0.8	3×540
SDSS J1029+2623	BC	1.8	Keck/UH88	400/8500	2006-Nov-14		-88	0.8	
					2007-May-17				
					2007-Nov-12				

[a]Pair or image observed.

[b]Separation between images in arcseconds.

[c]Position angle in degrees E of N.

[d]Seeing in arcseconds.

[e]Seconds of time.

The data reduction was performed with IRAF tasks and included bias subtraction, flat normalization, and wavelength calibration. The flux calibration was not done because we are only interested in the flux ratios. The spectra extraction for all the systems except for SDSS J1029+2623, were made by fitting a Gaussian function to each component along the wavelength axis to obtain uncontaminated spectra for each component. In the case of SDSS0924+0219, part of the flux of the lens galaxy is contaminating the quasar components, hence we fit three Gaussians: two for the components and one for the lens galaxy. To better constrain the lens spectrum we guided the lens galaxy position in a determined range of pixels between the two images, and the flux amplitude using a simulated spectrum of the galaxy (Figure 4.2). The model was obtained from ESO Exposure Time Calculators[2] (ETC) for FORS2 instrument. We choose the template of a elliptical galaxy spectrum at the redshift of the lens, the sky conditions and instrument setup were selected as being the same as when the spectra were taken.

For all the systems we also used broad-band data from CASTLES[3]. These data

[2]https://www.eso.org/observing/etc/

[3]CFA-Arizona Space Telescope LEns Survey, Kochanek, C.S., Falco, E., Impey, C., McLeod, B., & Rix, H.W. http://www.cfa.harvard.edu/glensdata.

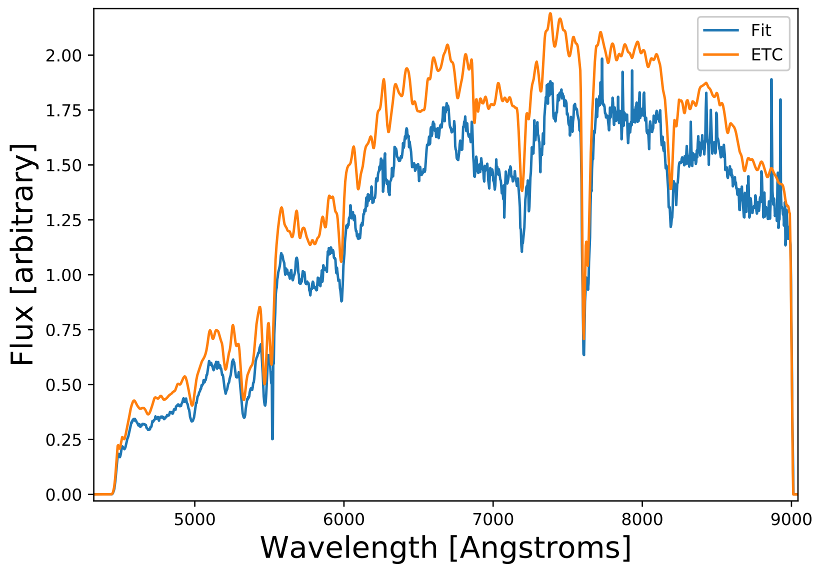

Figure 4.2: SDSS0924+0219 lens galaxy spectra. In Orange is the simulated spectrum using ESO ETC. Blue is the spectrum fitted by a Gaussian function to extract the observed lens spectrum.

were taken in 2003-2004 with Hubble Space Telescope (HST) in three different bands (F160W, F555W, and F814W). Additionally, we used data from the literature: for HE0047-1756 (Wisotzki et al. 2004; Sluse et al. 2012), SDSS1155+6346 (Pindor et al. 2004), HE2149-2745 (Wisotzki et al. 1996; Lopez et al. 1998; Fadely & Keeton 2011; Burud et al. 2002), SDSS0924+0219 (Inada et al. 2003; Pooley et al. 2007; Floyd et al. 2009; Blackburne et al. 2011), and Q1355-2257 (Morgan et al. 2003; Sluse et al. 2012).

4.1.3 Method

We compare the magnitude difference in the continuum under the emission lines with the magnitude difference in the emission line cores, $\Delta m = (m_B - m_A)_{cont} - (m_B - m_A)_{core}$ (e.g., see Mediavilla et al. 2009, 2011; Rojas et al. 2014; Motta et al. 2017). We perform this analysis with DIPSO (Howarth et al. 2004) in STARLINK. The continuum is obtained by fitting a line ($F = a\,\lambda + b$) to regions selected at both sides of each emission line. Then, the continuum is subtracted, and we integrate the emission line in a relatively narrow interval (between 20 to 60Å, depending of the line shape) around the line peak (hereafter "core of the line"). The narrower intervals around 20-25Å are for those lines that present absorptions splitting the line, then a more restricted interval must be selected, for example in CIV for SDSS1029+2623. The uncertainty for the continuum is the fit rms error, and for the lines is the rms error in the determination of the total flux added in quadrature, which is assumed to be the same as the continuum.

If $(m_B - m_A)_{core}$ does not present any change along to the wavelength, we used the mean of these values as a no-microlensing baseline, thus if $(m_B - m_A)_{cont} \neq (m_B - m_A)_{core}$ (i.e. $\Delta m \neq 0$) it means there is microlensing effect. Furthermore, if these Δm values change with wavelength, being larger in the blue than in the red wavelength, the system exhibits chromatic microlensing effect (e.g. Figure 4.4).

In the case in which a lens model is not found in the literature, we build our own model using a Singular Isothermal Ellipsoid (SIE) or a Singular Isothermal Sphere plus shear (SIS $+\gamma$) with *Lensmodel* (Keeton 2001). We employ the astrometry available in CASTLES and the flux ratios between images from the emission line cores in our data. From the model, we obtain the convergence and shear at the position of each image (κ_A, γ_A, κ_B, γ_B). The convergence and shear are used to compute magnification maps applying the Inverse Polygon Mapping method (Mediavilla et al. 2006, 2011). We considered microlenses of 1 $M_\odot$ and assumed a mass fraction in stars $\alpha = 0.1$ (Mediavilla et al. 2009; Pooley et al. 2009). The size for each map is 1000$\times$1000 pixels^2 for HE0047-1756 and SDSS11556346, and 5000$\times$5000 pixels^2 for HE2149-2745 and SDSS0924+0219, all of them have a size in Einstein radii of 15$\times$15.

To estimate the size of the accretion disk and its temperature profile from the microlensing data, we follow a Bayesian procedure (see, e.g. Mediavilla et al. 2011). The accretion disk is modeled as a Gaussian with intensity profile I(R) $\propto$ exp(-R^2/2r$_s^2$), where r$_s$ is the accretion disk size and p is related to the temperature profile of the disk (p=1/β=4/3, Shakura & Sunyaev 1973). To estimate the likelihood to reproduce the measured microlensing amplitudes, we randomly place Gaussian sources with different sizes and profile slopes on the magnification maps. The estimations were obtained at the rest frame wavelengths λ_{rf}: 2045Å (HE0047-1756), 1398Å (SDSS1155+6346), 1310Å (HE2149-2745), and 3533Å (SDSS0924+0219 and Q1355-2257).

4.1.4 HE0047-1756 results

This subsection is based on the publication: 'Chromatic Microlensing in HE0047-1756 and SDSS1155+6456'. ***Rojas K.****, Motta V., Mediavilla E., Falco E., 2014, ApJ, 797, 61.*

HE00471756 is a double system discovered by Wisotzki et al. (2004) with a separation between images A and B of 1.43 arc-seconds (CASTLES). The quasar and lens galaxy redshifts are $z_S = 1.66$ and $z_L = 0.41$, respectively (Eigenbrod et al. 2006; Ofek et al. 2006).

In Figure 4.3, the A and B spectra obtained with the Magellan telescope in 2008 are presented in the spectral ranges corresponding to the MgII and CIII] emission lines. There are no differences between the emission line profiles that could indicate microlensing effects on the BLR. In Table 4.2 and Figure 4.4, we present $m_B - m_A$ magnitude differences for the core of the emission lines and adjacent continua. There is good agreement between our results and those of Sluse et al. (2012). The $m_B - m_A$ emission line average is 1.59 ± 0.02 mag. In the 2008 (this work) and 2005 (Sluse et al. 2012) epochs, there is a relatively small offset between lines and continua that indicates microlensing of amplitude less than 0.2 mag

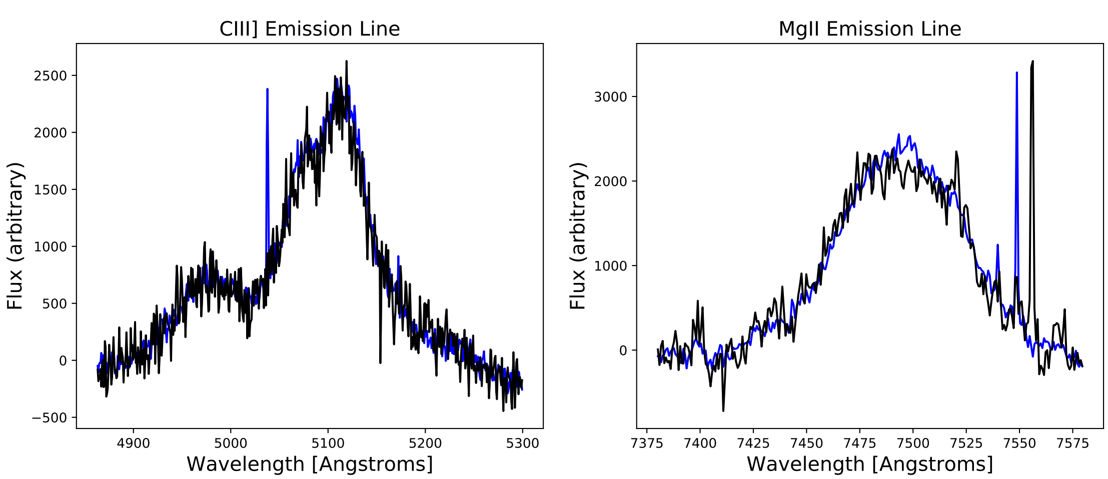

Figure 4.3: CIII] and MgII emission lines profiles as a function of observed wavelength for HE00471756. The blue line is the emission line without the continuum for A. The black line is the emission line without the continuum for B multiplied by a factor of four in each case to match the peak of A.

Table 4.2: HE0047-1756 Magnitude Differences.

Region	λ(Å)	Window[a](Å)	m_B - m_A (mag)	m_B - m_A[b](mag)
Continuum	5077	4800-5400	1.39 ± 0.12	1.394 ± 0.003
	7445	7330-7750	1.34 ± 0.07	1.471 ± 0.003
Line	CIII]	5080-5140	1.57 ± 0.16	1.591 ± 0.007
	MgII	7465-7525	1.56 ± 0.09	1.644 ± 0.005

[a]Integration window

[b]Data from Sluse et al. (2012)

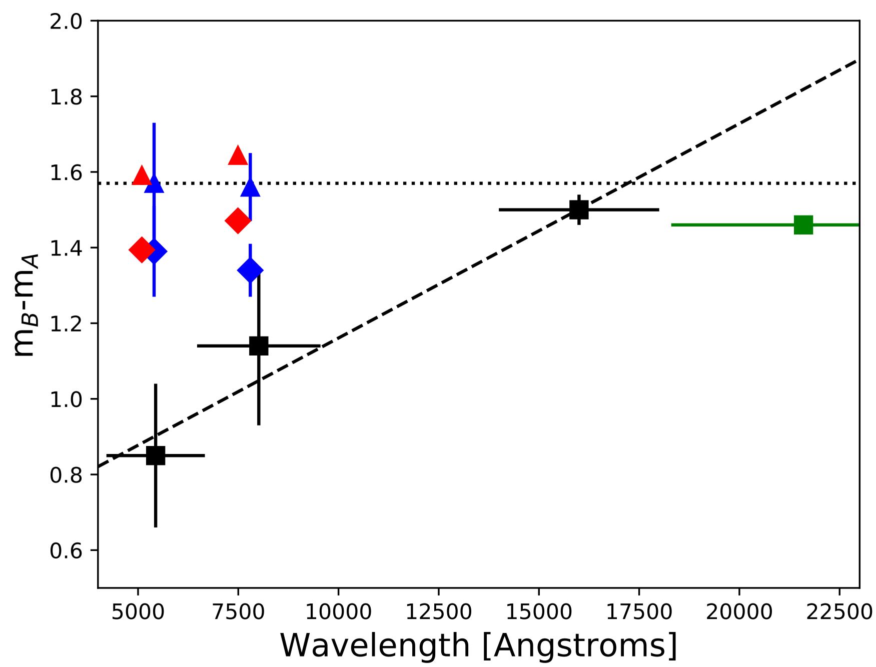

Figure 4.4: Magnitude differences $m_B - m_A$ as a function of wavelength for HE00471756. Solid squares are the continuum obtained from CASTLES. The horizontal error bar is the width of the broad band filter. The green square is a K_s band taken from Wisotzki et al. (2004). The diamonds represent magnitude differences from the continuum under the emission line core. The triangles represent the emission line cores without the continuum. Blue symbols are for our observed spectra and red symbols those from Sluse et al. (2012). The dashed line is the best linear fit for the CASTLES data. The dotted line is the median value for our emission lines.

Table 4.3: HE0047-1756 Chromatic Microlensing.

λ(Å)	Δm (mag)
5439	-0.75 $\pm$ 0.19
8012	-0.45 $\pm$ 0.22
16000	-0.09 $\pm$ 0.04

Much more significant variations of the continua (Figure 4.4) are found by comparing with CASTLES data in the F555W and F814W filters. The result for the H-band filter ($m_B - m_A$=1.5 $\pm$ 0.04), however, agrees with the $m_B - m_A$ emission line average, indicating that the region generating the emission in the H band is not affected by microlensing. The dependence on wavelength is evidence of chromatic microlensing in the 2003 epoch when the HST data were taken. The differences between the average value of the emission lines and the three CASTLES points (Δm) are listed in Table 4.3.

Following the method described in Subsection 4.1.3, we use these wavelength-dependent microlensing measurements to estimate the size and temperature profile of the accretion disk. We have used *Lensmodel* (Keeton 2001) to fit an SIS $+\gamma$ lens model to the image coordinates of HE0047–1756 from CASTLES and to the emission-line average flux ratio that we measured. The best fit yields: $\kappa_A = 0.45$, γ_A=0.48, $\kappa_B = 0.62$, and $\gamma_B = 0.66$. These results are in agreement with Mediavilla et al. (2009) and Sluse et al. (2012).

In Figure 4.5, we present the probability density functions of r_s and p conditioned to the microlensing measurements, Δm_i (Table 4.3) and $p(r_s, p|\Delta m_i)$. From these probability distributions, we obtain $r_s = 4.6^{+5.5}_{-2.5} \sqrt{M/M_\odot}$ light days and p = (2.3 $\pm$ 0.8) (Figure 4.5). For 0.3 $M_\odot$ microlenses, $r_s = 2.5^{+3.0}_{-1.4} \sqrt{M/0.3M_\odot}$ light days. The values for r_s are in reasonable agreement with typical size estimates derived for other systems using microlensing (see Jiménez-Vicente et al. (2012), and references therein). Due to the large microlensing chromaticity detected in this system, the values for p are larger than those predicted by Shakura & Sunyaev (1973), although consistent within errors. This is notable because in previous studies (Jiménez-Vicente et al. 2014), microlensing chromaticity was relatively weak and the inferred values for p were significantly smaller than the predictions of the thin disk model.

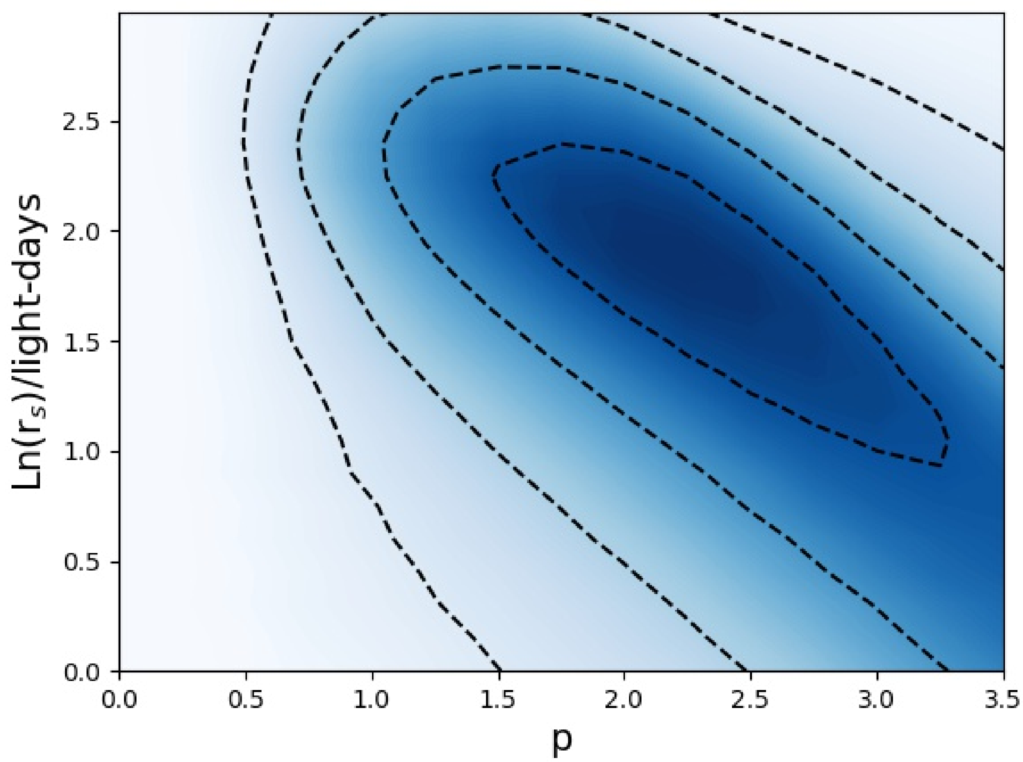

Figure 4.5: Probability density functions for HE00471756. The contours of probability are scaled in 0.5σ steps from the maximum

4.1.5 SDSS1155+6346 results

This subsection is based on the publication: 'Chromatic Microlensing in HE0047-1756 and SDSS1155+6456'. ***Rojas K.****, Motta V., Mediavilla E., Falco E., 2014, ApJ, 797, 61.*

SDSS1155+6346 is a double system discovered by Pindor et al. (2004) in the Sloan Digital Sky Survey data set (York et al. 2000) with a separation of 1.94 arc-seconds between the images (CASTLES). Pindor et al. (2004) measured redshifts of $z_L = 0.18$ and $z_S = 2.89$ for the lens and the source, respectively. The B image is within 0.2 arc-seconds from the galaxy center and, unusually, it is the brighter component.

In Figure 4.6, we present the A and B spectra from the 2010 MMT observations. These spectra are very similar in shape to those obtained by Pindor et al. (2004).

The contribution from the lens galaxy to the continuum almost disappears blueward from Lyα.

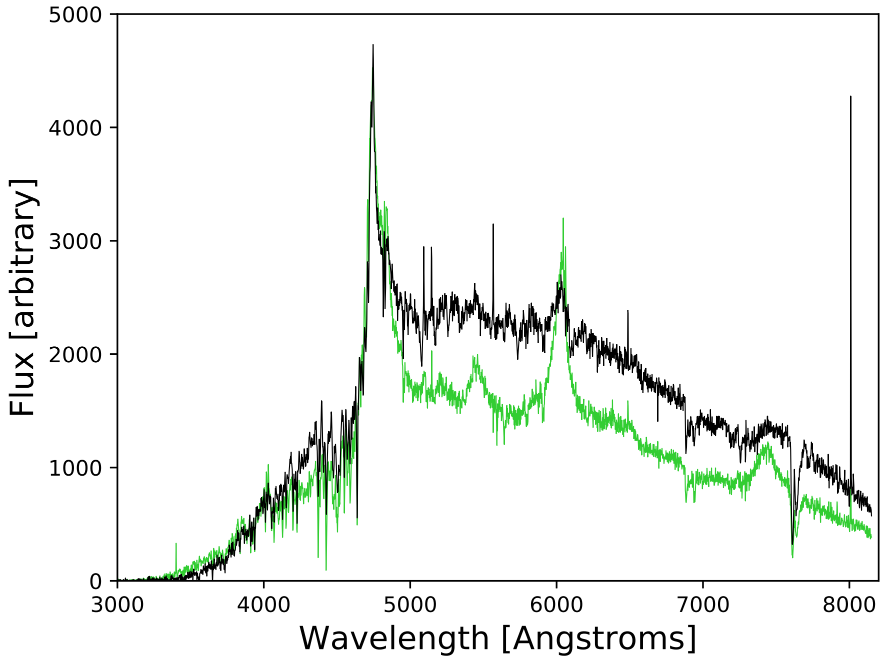

Figure 4.6: SDSS1155+6346 spectra from the 2010 MMT observations. The A (B) component is shown in green (black). The shapes of these spectra are very similar to those spectra obtained by Pindor et al. (2004).

In Figure 4.7 and Table 4.7, we present the continuum-subtracted and normalized spectra in the regions corresponding to the Lyα, SiIV, CIV, and CIII] emission lines. The A and B spectra are well matched for SiIV, CIV, and CIII] taking into account the presence of absorption features corresponding to the lens galaxy in the B spectrum. In Lyα, however, there is a significant difference between the shapes of the line profiles corresponding to A and B images. We have tried a second-order polynomial fit to the continuum and obtained the same results. These differences seem to be also present in the spectra taken by Pindor et al. (2004). However, the lens galaxy contribution to the continuum of the B image spectrum drastically changes from the red to the blue sides of Lyα, making the continuum subtraction more uncertain, and a sharp decay of the lens galaxy contribution in the red wing of Lyα may explain the observed differences.

The m_B–m_A magnitude differences obtained from the continua adjacent to the

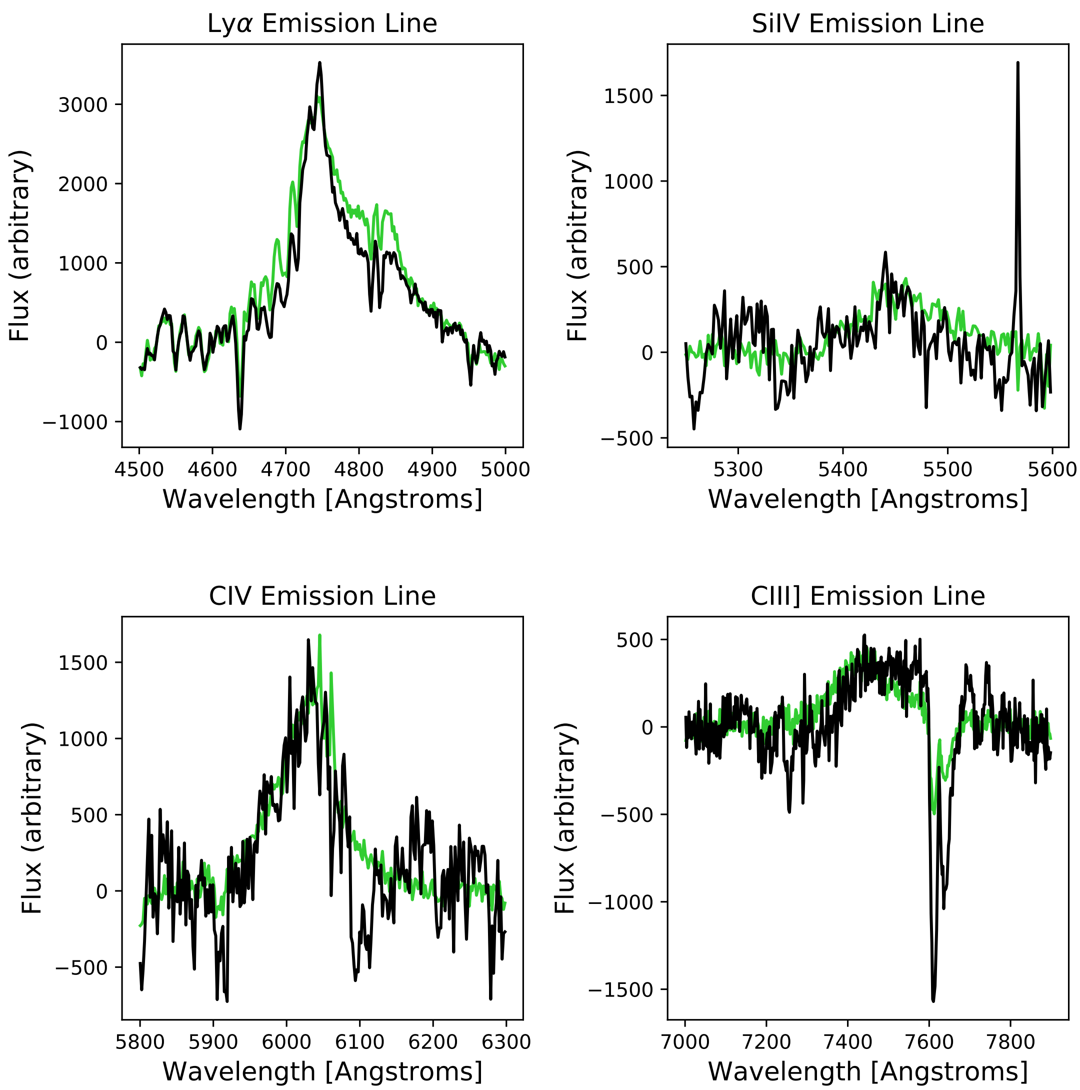

Figure 4.7: Lyα, SiIV, CIV, and CIII] emission lines profiles as a function of observed wavelength for SDSS1155+6346. The green line is the emission line without the continuum for A. The black line is the emission line without the continuum for B multiplied by a factor of 1.2 (Lyα), 2 (SiIV), 3.2 (CIV), and 2 (CIII]) to match the peak of A.

emission lines show a significant variation at Lyα: -0.23 $\pm$ 0.17 mag (Lyα), -0.44 $\pm$ 0.08 mag (SiIV region), -0.42 $\pm$ 0.20 mag (CIV region), and -0.49 $\pm$ 0.20 mag (CIII] region). In Figure 4.8, we plot the magnitude differences corresponding to the emission lines and adjacent continua with data corresponding to the F555W, F814W, F160W (CASTLES), and K bands (Pindor et al. 2004) obtained after subtracting

Table 4.4: SDSS1155+6346 Magnitude Differences.

Region	λ(Å)	Window[a](Å)	m_B - m_A (mag)
Continuum	4730	4500-5050	-0.23 $\pm$ 0.17
	5434	5350-5700	-0.44 $\pm$ 0.08
	6025	5600-6400	-0.42 $\pm$ 0.20
	7426	7000-7800	-0.49 $\pm$ 0.20
Line	Lyα	4718-4768	0.22 $\pm$ 0.34
	SiIV	5400-5500	1.14 $\pm$ 0.12
	CIV	6015-6065	1.34 $\pm$ 0.29
	CIII]	7390-7490	1.03 $\pm$ 0.29

Table 4.5: SDSS1155+6346 CASTLES continuum.

λ(Å)	Continuum (mag)
5439	0.42 $\pm$ 0.12
8012	0.76 $\pm$ 0.07
15500	0.97 $\pm$ 0.03

the lens galaxy. The contamination from the lens galaxy is clearly present in our continuum data. In fact, if we use the F555W data without removing the contamination of the galaxy (Figure 4.8), the resulting magnitude difference is in agreement with our data. If we leave aside the Lyα data that may be most contaminated by the lens galaxy continuum, the m_B–m_A magnitude differences obtained from the other lines agree within the uncertainties and are also consistent with the K-band data from Pindor et al. (2004), indicating that no strong differential extinction is affecting the flux ratios. If we take the average of the m_B–m_A values corresponding to SiIV, CIV, and CIII] emission lines as the no microlensing baseline, $(m_B–m_A)_{core} = 1.17 \pm 0.11$ mag, we can determine the chromatic variation of the CASTLES continuum (see Table 4.5).

We use Lensmodel (Keeton 2001) to fit an SIS + γ lens model to the image positions of SDSS1155+6346 from CASTLES and of the average flux ratio of the emission lines measured (excluding Lyα). The best fit yields κ_A=0.22, γ_A=0.34, κ_B=1.67, and γ_B=1.47. Chantry et al. (2010) suggest a nearby cluster may explain the high shear and ellipticity that we measured. We identify this cluster as MaxBCG J178.81693+63.83446 (Koester et al. 2007).

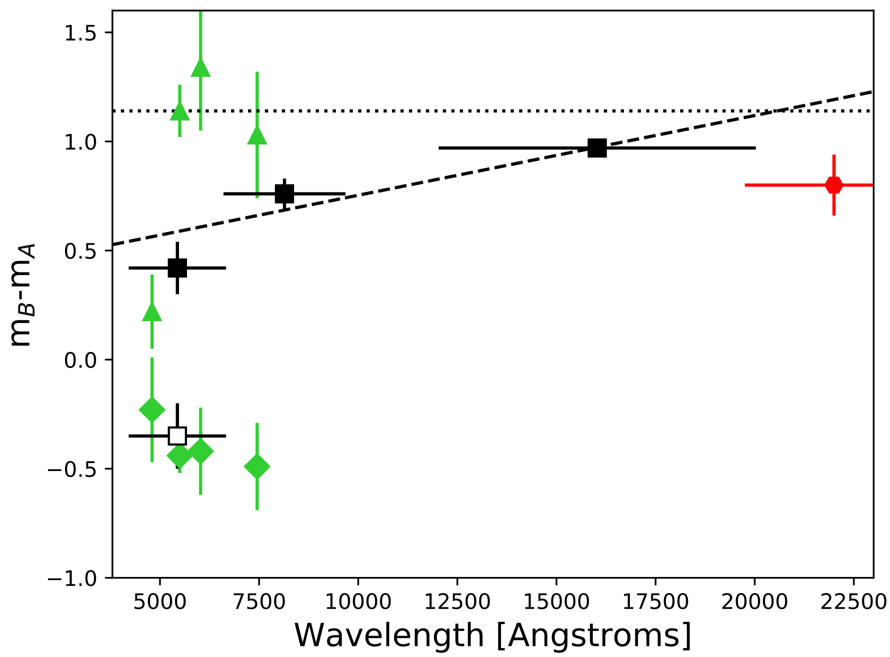

Figure 4.8: Magnitude differences $m_B - m_A$ as a function of wavelength for SDSS115+6346. The green diamonds represent magnitude differences from the continuum under the emission line cores, and the green triangles represent the emission line cores without continuum for our observed spectra. The dotted line is thecmedian value for the emission lines. The solid black squares are data from CASTLES for three bands: F555W, F814W, and F160W. The horizontal error bar is the width of the broad band filter. The solid hexagon is from Pindor et al. (2004). The dashed line is the best linear fit for the CASTLES points. The open square at $\lambda = 5500$ Å is the CASTLES continuum taking into account contamination from the lens galaxy.

In Figure 4.9, we present $p(r_s, p|\Delta m_i)$, the pdf of r_s and p conditioned to the microlensing measurements, Δm_i (Table 6). From these probability distributions, we obtain the following estimates for the accretion disk parameters: $r_s = 10^{+15}_{-6}$ $\sqrt{M/M_\odot}$ light days and p = 1.5 ± 0.6. For $0.3M_\odot$ microlenses, the sizes would be $r_s = 5.5^{+8.2}_{-3.3}$ $\sqrt{M/0.3M_\odot}$ light days.

The large measured microlensing chromaticity implies values of p consistent with the thin disk model. The inferred size is large not only compared with the thin disk model predictions but also with microlensing based estimates obtained for other lensed systems

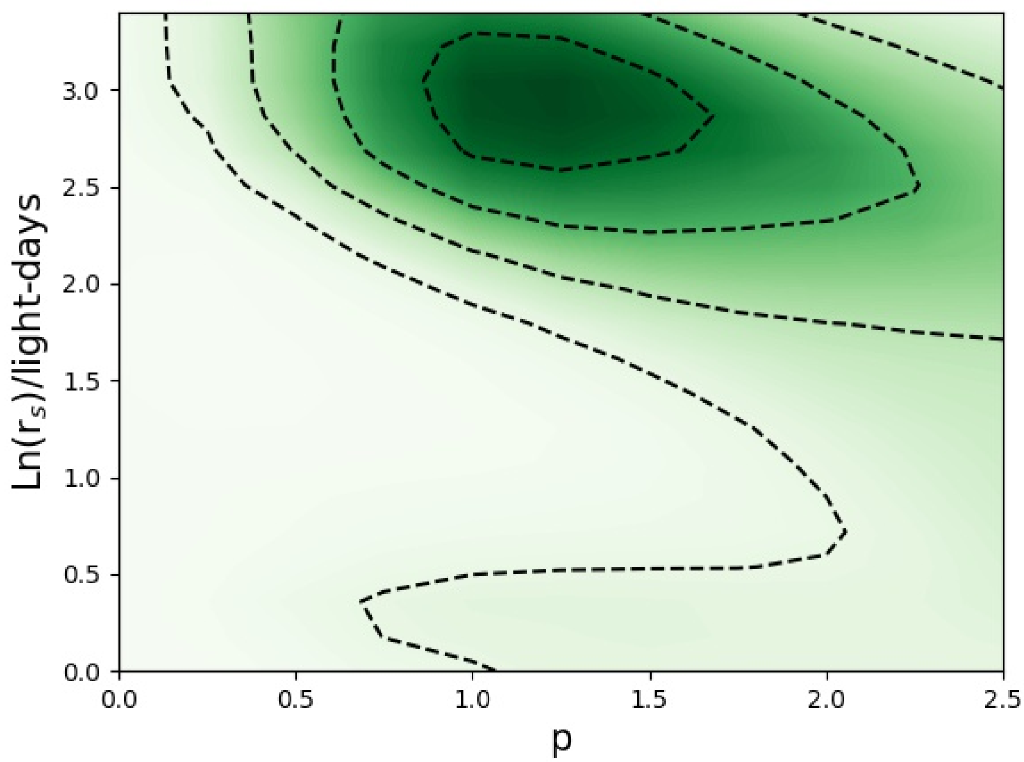

Figure 4.9: Probability density functions for SDSS1155+6346. The contours of probability are scaled in 0.5σ steps from the maximum.

4.1.6 HE2149-2745 results

This subsection is based on the publications: 'Probing the broad line region and the accretion disk in the lensed quasars HE0435-1223, WFI2033-4723 and HE2149-2745 using gravitational microlensing'. Motta, V., Mediavilla, E., ***Rojas, K.****, Falco, E., Jiménez-Vicente, J., Muñoz, J.A., 2017, ApJ 835, 132.*

HE 2149-2745 is a double system that was discovered by Wisotzki et al. (1996). The images A and B are separated by 1.70 arcseconds and are located at $z_S = 2.033 \pm 0.005$. The lens galaxy is at $z_L = 0.603 \pm 0.001$ (Eigenbrod et al. 2007). Chromatic microlensing was detected in spectra taken by Burud et al. (2002).

The spectra with continuum subtraction for the A and B images in the regions of the CIV, CIII], and MgII emission lines (Figure 4.10) match well, except for the absorption in CIV. Sluse et al. (2012) found in their spectra the same difference and attribute it to time-variable broad absorption together with a time delay. They found a chromatic difference that is attributed to dust extinction on image B and/or intrinsic variability combined with time delay of ~ 103 days.

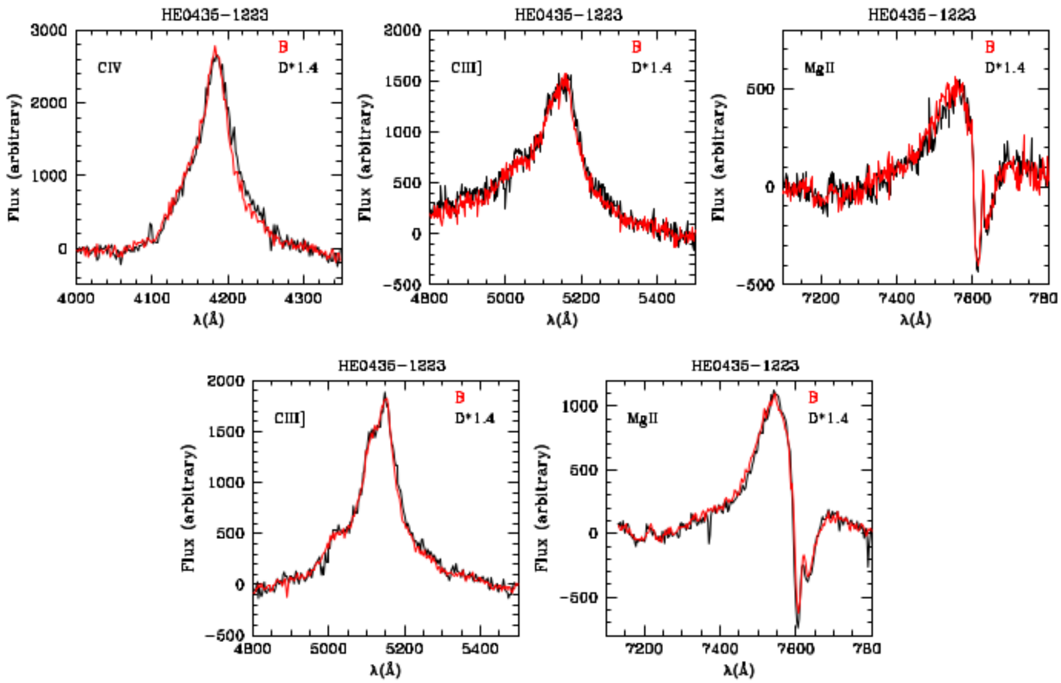

Figure 4.10: CIV, CIII], and MgII emission lines profile for HE2149-2745. The black line is the emission line without continuum for component B multiply by a factor (showed in the figure) to match with A image in red. Top: the VLT observed spectra. Bottom: deconvolved spectra by Sluse et al. (2012).

We compare our spectroscopic continua with CASTLES data (Figure 4.11,left). The differences using F555W and F814W bands shows that there is contamination by the lens galaxy. The contamination in the B spectra could be up to 60%, while in the deconvolved spectra it could be around 30%. For the following analysis we will use the broadband data to obtain the magnitude difference in the continuum.

The emission-line and continuum ratios for our data and literature data are shown in In Figure 4.11 (Table 4.6). The emission-line ratios show no dependence with wavelength, then there is no significantly extinction affecting the images. However, the magnitude difference in the continuum, show chromaticity, likely induced by microlensing (Figure 4.11 right, Table 4.7).

Using the chromaticity measurements, we estimate the size r_s and the slope p of the accretion disk. To compute the magnification maps we used the convergence

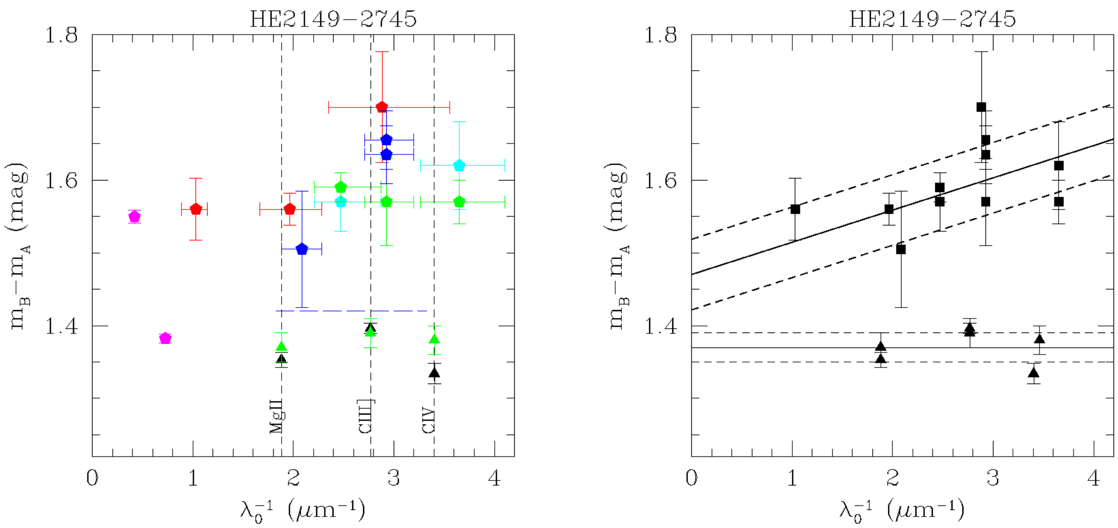

Figure 4.11: Magnitude difference m$_B$-m$_A$ vs. wavelength for HE2149-2745. Left: the magnitude difference in the core of the emission lines is represented by triangles: deconvolved spectra data by Sluse et al. (2012) in green, and VLT in black. The integrated continuum from broadband is represented by filled pentagons: CASTLE (red), Wisotzki et al. (1996) (light-blue), Lopez et al. (1998) (green), Fadely & Keeton (2011) (magenta), and Burud et al. (2002) (blue). The dashed blue line represent the relative magnification from spectra obtained by Burud et al. (2002). Right: Model fitted to the data. Squares represent the continuum and triangles the lines. Black line is the function fitted to the continua and the average for the emission lines. Dashed lines are the standard deviation for the continuum fit and the standard error of the mean for the emission lines.

Table 4.6: HE2149-2745 Magnitude differences

Region	λ (Å)	Window[a](Å)	$(m_B$-$m_A)^{\rm b}$(mag)	$(m_B$-$m_A)^{\rm c}$(mag)
continuum	4170	4000-4350	-0.11 ± 0.02	
	5140	5000-6200	-0.14 ± 0.01	-0.12 ± 0.02
	7560	8250-8650	-0.28 ± 0.02	-0.22 ± 0.01
Line	CIV λ1549	4170-4195	-0.37 ± 0.02	
	CIII] λ1909	5720-5830	-0.34 ± 0.01	-0.36 ± 0.01
	MgII λ2800	8480-8540	-0.47 ± 0.01	-0.37 ± 0.01

[a]Integration window

[b]VLT data

[c]Sluse et al. (2012)

and shear provides by Sluse et al. (2012): $\kappa_A = 0.31$, $\kappa_B = 1.25$, $\gamma_A = 0.32$, and $\kappa_B = 1.25$. From the probability distribution (Figure 4.11, right) we obtain r$_s$ = 8^{11}_{-5}

Table 4.7: HE2149-2745 Chromatic-Microlensing

λ (Å)	Δm^{a}(mag)
4380.0	0.26 ± 0.06
8140.0	0.19 ± 0.02
38000.0	0.15 ± 0.01

[a]Difference between the magnitude difference of the broadband data from CASTLE and L-band from Fadely & Keeton (2011), and the emission lines core from VLT, the reanalysis of Sluse et al. (2012), and K_s-band from Fadely & Keeton (2011): $(m_B\text{-}m_A)_{cont}$ - $(m_B\text{-}m_A)_{core}$.

light-days at $\lambda_{rest-frame}$ = 1310 Å and p = 0.4 ± 0.3.

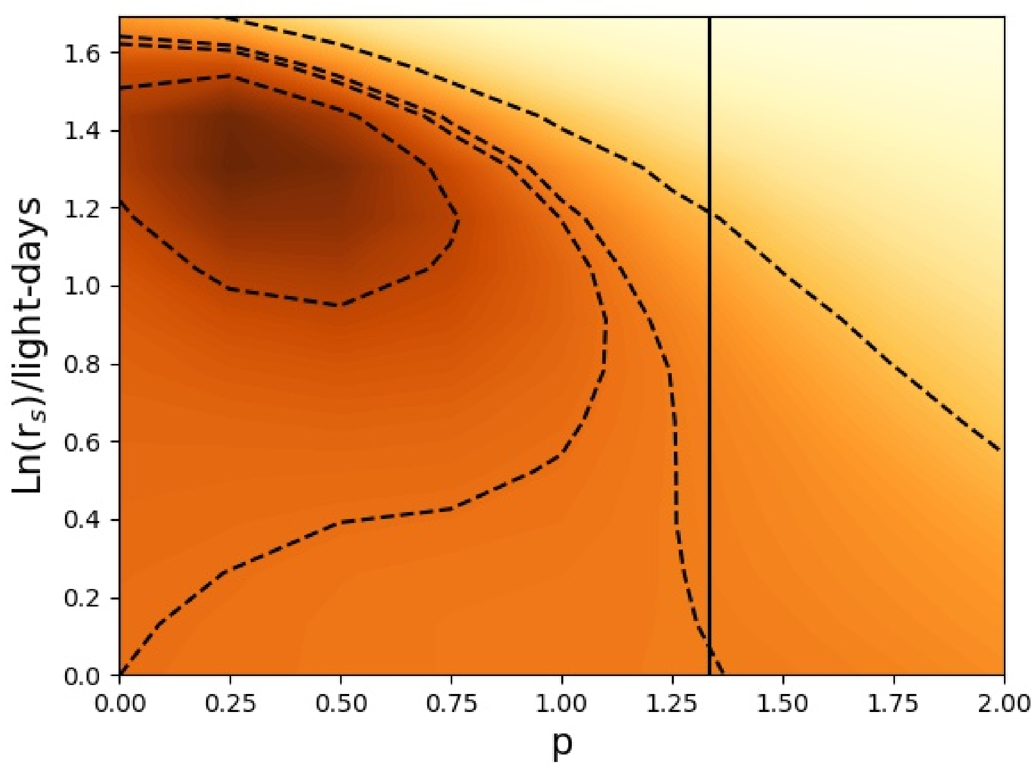

Figure 4.12: PDF obtained using the chromatic microlensing measurements for HE2149-2745. Contours correspond to 0.5σ, 1.0σ,1.5σ, 2.0σ. The solid line correspond to p=4/3 value predicted by Shakura & Sunyaev (1973).

4.1.7 SDSS0924+0219 results

This subsection is based on the article in preparation: 'Microlensing Analysis for SDSS0924+0219, Q1355-2257, and SDSS1029+2623' ***Rojas K.****, Motta V., Mediavilla E., Falco E., J. Jimenez-Vicente.*

This quadruple system was discovered by Inada et al. (2003) who calculated the quasar redshift at z_S=1.52 arc-seconds. The lens is an elliptical galaxy at z_L=0.39 (Ofek et al. 2006). We present VLT spectra (Figure 4.13) for C and B components which are separated 1.52". The line profiles show differences in the broad region likely produced by microlensing effect.

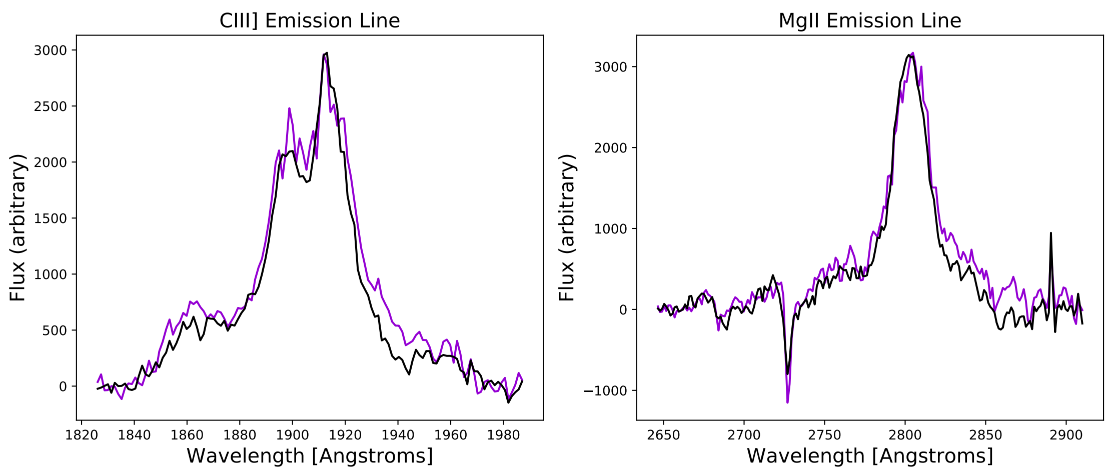

Figure 4.13: CIII] and MgII emission lines profiles without the continuum for SDSS0924+0219. In blue the A component and in black the B component multiplied by a factor of 1.38 (CIII]) and 1.33 (MgII) respectively.

We calculate the magnitude differences for the core of the emission lines and the continua for the spectra (Figure 4.14 and Table 4.8) and compared them with literature results. CASTLES and Keeton et al. (2006b) values are in agreement with ours, showing no microlensing effect in the epoch of those measurements (2003). We took as no-microlensing baseline the median value among the core of the lines, HST, and Keeton et al. (2006b) data: 0.34$\pm$0.02 mag. In our data we found Δm up to 0.2 mag at λ4800 but the difference decrease down to $\sim$ 0.06 at λ7800. We also see this trend in the literature data, but showing different chromatic variations for different epochs. The first epoch correspond to Inada et al. (2003) with data taken in 2001. The HST data (CASTLES and Keeton et al. (2006b)) were taken in 2003 and they all are in agreement with the measurements of the core of the emission lines, indicating that the continuum of each component is not affected by microlensing. Comparing Blackburne et al. (2011) (data taken between February 2007 and May 2008), Floyd et al. (2009) (data taken in March 2008) and our own data (observed in April 2008), we see a change in the slope of the continua. The points corresponding to g and r bands in Floyd et al. (2009) data show large differences compared to the other bands. Considering that the authors do not offer an explanation for this, that we are unable to re-analyze the data to confirm those measurements (Magellan telescopes have no public data archive), and that Blackburne et al. (2011) data show no such deviation around the same epochs, we decided to disregard them in our calculations.

Table 4.8: SDSS0924+0219 Magnitude differences

Region	λ (Å)	Window (Å)	m_C-m_B (mag)
continuum	4818	4530-5070	0.55 ± 0.01
	7067	6600-7500	0.42 ± 0.01
Line	CIII]	4808-4831	0.30 ± 0.02
	MgII	7034-7094	0.42 ± 0.01

The differences between the baseline and the continua obtained from different data sets are listed in Table 4.9. We analyzed the four continuum data sets (ours, Inada et al. (2003), Blackburne et al. (2011), and Floyd et al. (2009)) independently.

Table 4.9: SDSS0924+0219 Chromatic Microlensing

Data	λ (Å)	Δm (mag)
this work	4820.0	0.23 ± 0.04
	7816.0	0.06 ± 0.04
	16000.0	0.00 ± 0.06
Inada et al. (2003)	3545.0	-0.28 ± 0.08
	6231.0	-0.24 ± 0.07
	7625.0	-0.22 ± 0.06
Blackburne et al. (2011)	3600.0	0.80 ± 0.10
	9050.0	0.57 ± 0.06
	21500.0	0.02 ± 0.06
Floyd et al. (2009)	7625.0	0.33 ± 0.07
	10200.0	0.28 ± 0.06
	16500.0	0.15 ± 0.06

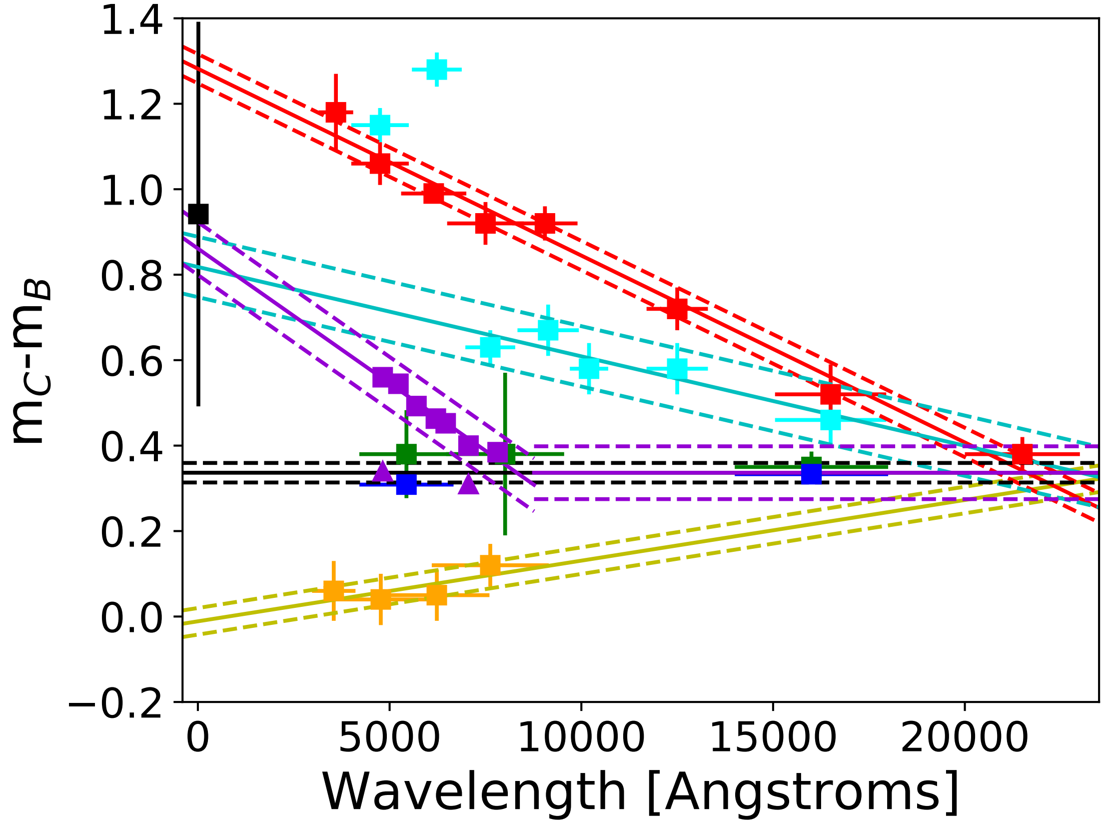

Figure 4.14: Magnitude differences m_C-m_B as a function of wavelength for SDSS0924+0219. Purple triangles are the emission line cores and the purple squares are the continuum calculated from VLT spectra. Yellow squares are the photometric data presented by Inada et al. (2003) for the bands: ugri. Green squares are the broad band continuum from CASTLES. Blue squares are Keeton et al. (2006b) measurements from HST bands F555W and F816W. Red squares are the relative photometry from u'g'r'i'z'JHK$_s$ bands in Blackburne et al. (2011). The black square is an X-ray measurement, taken in 2005, given by (Pooley et al. 2007). Cyan squares are photometric data showed by Floyd et al. (2009) in the bands: HJYz'i'r'g'. The black solid line is the median among the measurements of the line cores, CASTLES data and Keeton et al. (2006b) bands, the dashed lines represent the standard deviation around these points. The colored solid lines represent the best linear fit for each set of points, the dashed lines represent the standard deviation of the points.

The probability density function of r_s and p for the intersection among the four continuum data sets is presented in Figure 4.15. This distribution gives a size for the accretion disk of $r_s = 7^{+3}_{-2}$ light-days at λ3533Å and a value for the thermal profile $p = 0.7 \pm 0.2$ at 1σ. In general, previous studies found sizes for the accretion disk smaller than our estimation: $0.07 < r_{s,\lambda 2770} < 0.26$ light-days (Morgan et al. 2006), $r_{s,\lambda 3200} = 0.14$ light-days (Pooley et al. 2007), $r_{s,\lambda 2770} = 0.39^{+0.8}_{-1.2}$ light-days (Morgan et al. 2010), $r_{s,\lambda 8140} = 0.24$ light-days (Mosquera & Kochanek 2011), $r_{s,\lambda 3600} = 2^{+2}_{-1}$ light-days (Blackburne et al. 2011), $r_{s,\lambda 2500} = 0.62^{+0.6}_{-0.8}$ light-days (MacLeod et al. 2015), and $r_{s,\lambda 3540} = 4.7$ light-days (for all data) Floyd et al. (2009). This last estimation is in agreement with our result within error. From the thin disk theory (p=4/3) we will expect $r_s = 0.12$ light-days, assuming a black hole mass of $2.8 \times 10^8 M_\odot$ (Morgan et al. 2006). Floyd et al. (2009) estimate p=0.75 using only Magellan data and $0.8 < p < 17$ using all their data set, MacLeod et al. (2015) estimated $p = 2.17 \pm 2.17$. Our result (p=0.7 $\pm$ 0.2) is in agreement with Floyd et al. (2009) and also with the average slope found by Jiménez-Vicente et al. (2014) using a sample of 8 systems.

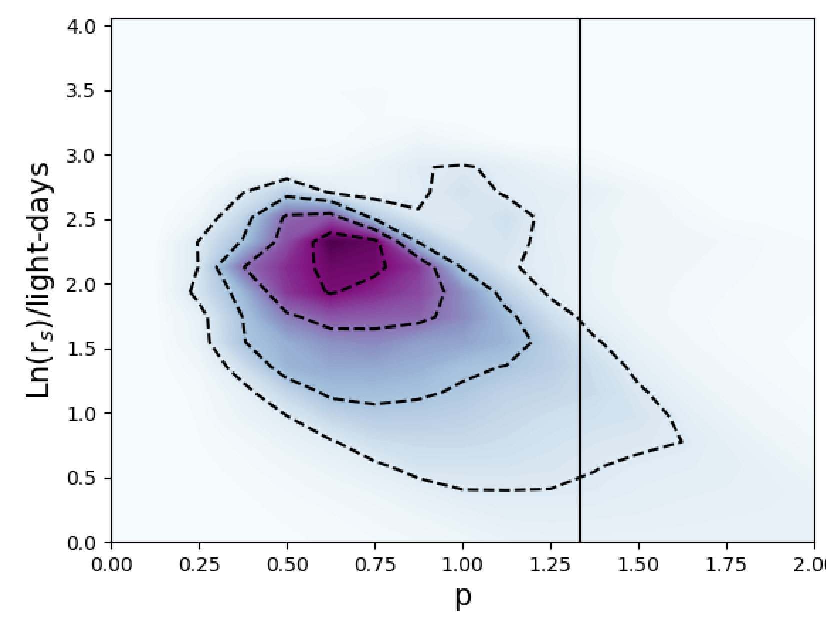

Figure 4.15: Combined probability density function for SDSS0924+0219. Contours correspond to 0.5σ, 1σ, 1.5σ, and 2σ respectively. The black solid line shows the value for p=4/3 (Shakura & Sunyaev 1973) for the thin disk model.

4.1.8 Q1355-2257 results

This subsection is based on the article in preparation: 'Microlensing Analysis for SDSS0924+0219, Q1355-2257, and SDSS1029+2623' ***Rojas K.****, Motta V., Mediavilla E., Falco E., J. Jimenez-Vicente.*

Discovered by Morgan et al. (2003) using HST data, it is a double lensed quasar with an image separation of 1.23 arc-seconds. The redshift of the quasar is z_S=1.37 (Morgan et al. 2003) and the redshift for the lens is z_L=0.70 (Eigenbrod et al. 2006).

We present VLT spectra for both images of the quasar (AB), and also a re-analysis of the deconvolved data presented by Sluse et al. (2012). The line profiles for both data sets (Figure 4.16) show differences in the wings that can be explained by microlensing in the BLR.

The magnitude difference for the core of the emission lines and the continua below are shown in the Figure 4.17 and table 4.10. The median value among the emission lines cores of our data, the deconvolved data set, and the values presented by Sluse et al. (2012) for the emission lines are taken as a baseline for no microlensing effect, with a value of 1.24 ± 0.05 mag. In general, there is a difference of at least 0.5mag between the baseline and the continua in our data, Sluse et al. (2012) deconvolved spectra, and Morgan et al. (2003) data, evidence of microlensing effect. Between $\lambda 3500\text{Å} - \lambda 6180\text{Å}$ we found chromatic microlensing, and for $\lambda > 6180\text{Å}$ the magnitude difference presents a change in the slope as also seen in the F814W and F160W broad-bands from CASTLES.

Table 4.10: Q1355-2257 Magnitude differences

Region	λ (Å)	Window (Å)	m_C-m_B (mag)
Continuum			
Our data	4523	4400-4764	1.73 ± 0.01
	6633	6050-7100	1.63 ± 0.01
Deconvolved data	4531	4378-4754	1.79 ± 0.01
	6608	6050-7030	1.60 ± 0.01
Line			
Our data	CIII]	4503-4543	1.30 ± 0.02
	MgII	6603-6663	1.22 ± 0.01
Deconvolved data	CIII]	4513-4546	1.30 ± 0.01
	MgII	6588-6628	1.52 ± 0.01

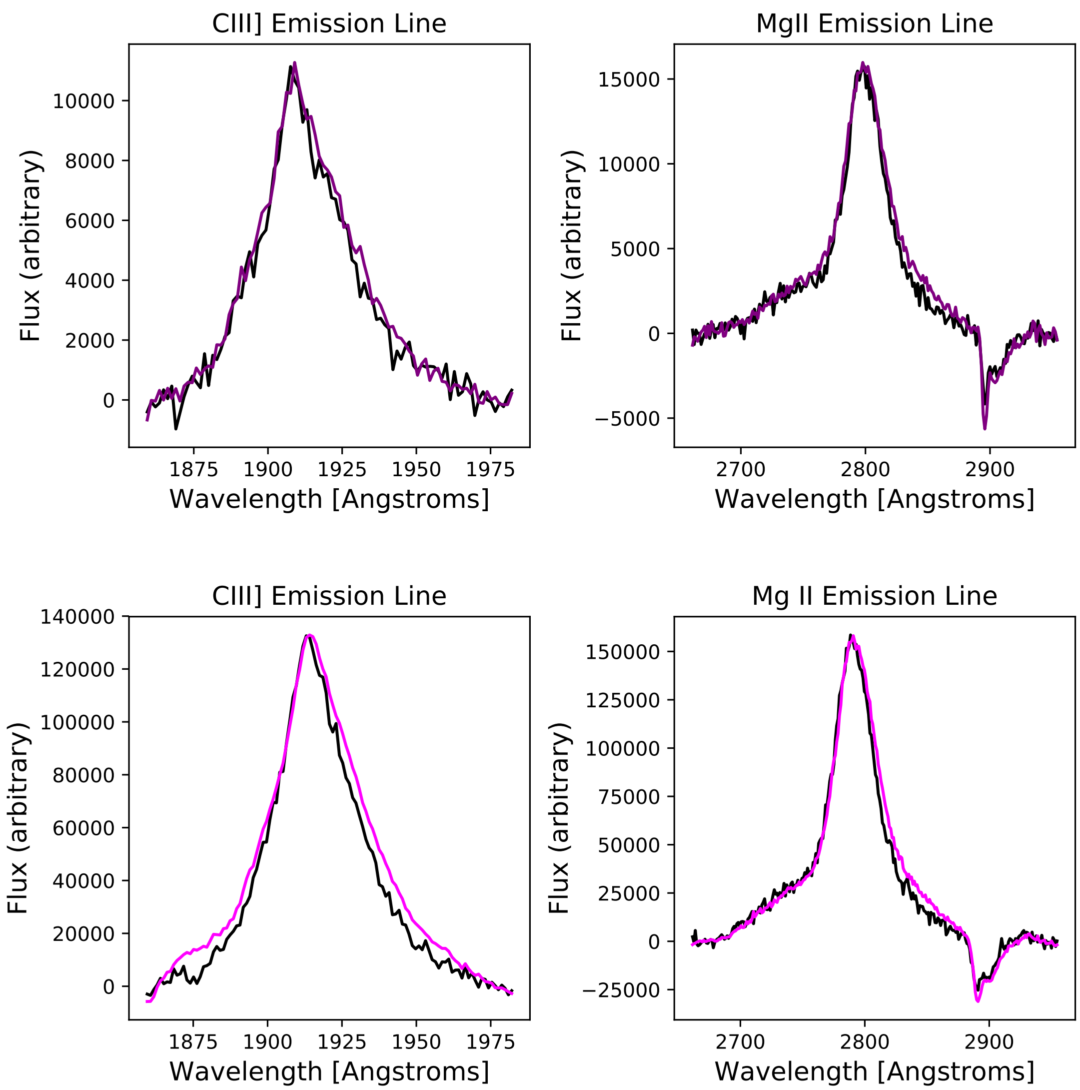

Figure 4.16: CIII] and MgII emission line profiles without the continuum for Q1355-2257 by this work (top panel) and the re-analysis of Sluse et al. (2012) spectra (bottom panel). Shown in purple/magenta is the A component and in black is the B component multiplied by a factor of 3.2 (CIII]), and 2.8 (MgII) for our data and 3.3 (CIII]), and 3.2 (MgII] for deconvolved data.

To explain the increase in $\Delta m > 0.42$ mag beyond $\lambda 7300$Å, we investigated the possible contamination by the lens galaxy in the nearby component B using the data provided by CASTLES. A 50% of flux contamination from the lens galaxy in the image B for the filter F816W gives a $\Delta m = -0.14$. The introduction of galaxy flux produced the opposite effect moving the $m_B - m_A$ difference to the

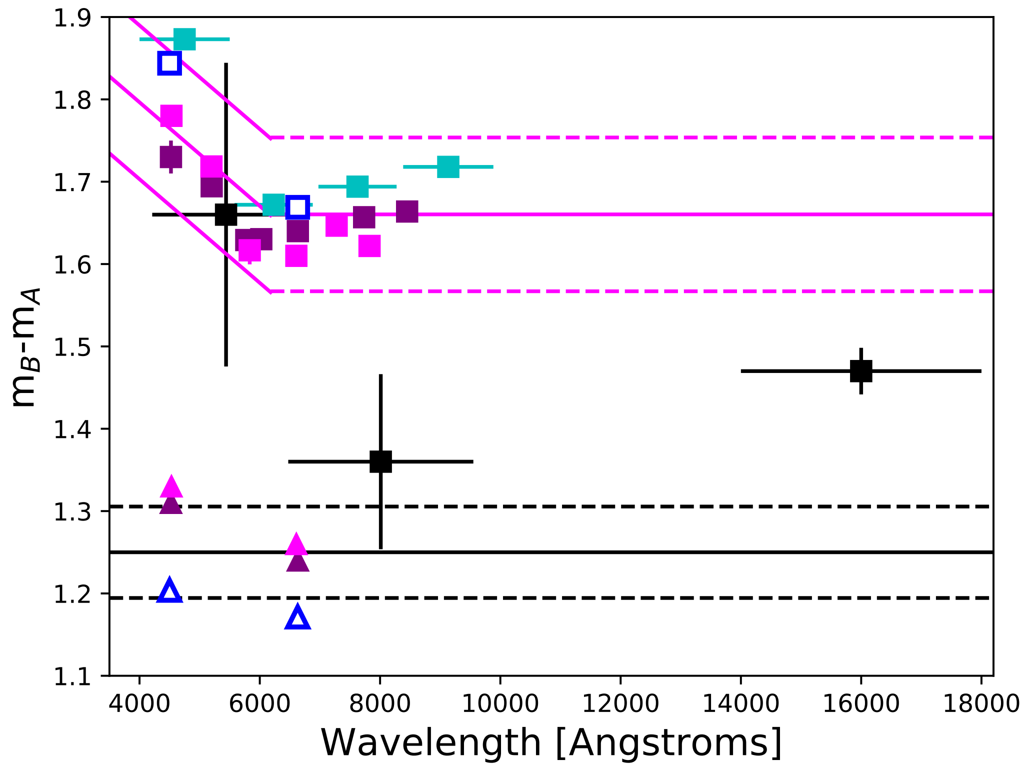

Figure 4.17: Magnitude differences m_B-m_A as a function of wavelength for Q1355-2257. Triangles are the emission line cores without the continuum, and squares are the continuum integrations. Purple symbols are the measurements obtained from our VLT spectra. Magenta symbols are the results obtained using the deconvolved data of Sluse et al. (2012), while the blue symbols are the estimation presented by the authors. Black squares are the continuum obtained from CASTLES. Cyan squares are the data for the g, r, i, and z bands in Morgan et al. (2003). The black solid line is the emission line median, and the dashed lines represent the standard deviation. The magenta solid line between $\lambda3500-\lambda7300$ Åis the best linear fit, and between $\lambda6180-\lambda18200$ is the median value for the points in each interval. The dashed lines represent the standard deviation.

direction of the lines instead of moving it towards to the continuum of our spectra. Another option is contamination by the quasar host galaxy, considering that HST data show a ring in the bands with the anomalous flux. As consequence, we used the data between $\lambda3500 - \lambda7300$ Å to analyze the chromatic microlensing effect. The differences between the baseline and the fitted continua are in Table 4.11.

As described in the section 4.1.3, we modeled the system using *Lensmodel* (Keeton 2001). We obtained the convergence and the shear for each image: $\kappa_A = 0.30$, $\gamma_A = 0.29$, $\kappa_B = 1.10$, $\gamma_B = 1.08$. These values are similar to those obtained by

Table 4.11: Q1355-2257 Chromatic-Microlensing

λ (Å)	Δm (mag)
4400.0	0.54 ± 0.05
6200.0	0.42 ± 0.20
7300.0	0.42 ± 0.05

Sluse et al. (2012). The probability density function of r_s and p (Figure 4.18) give us, at 1σ error, $r_s = 4^{+4}_{-2}$ light-days, and p = 1.1 ± 0.5 for the accretion disk. This is the first estimation of the size and p using chromatic microlensing for this system. From the thin disk theory (p=4/3) we would expect a size of r_s = 0.3 light-days, assuming a M_{BH}=1.1×10^9 $M_\odot$ (Sluse et al. 2012). Our estimated size is larger than the predicted, while the value for p is in agreement within errors. Compared with the results obtained for other systems (Rojas et al. 2014; Jiménez-Vicente et al. 2015b; Motta et al. 2017) we also obtain that the size of the accretion disk is generally larger than the predicted by the thin disk theory.

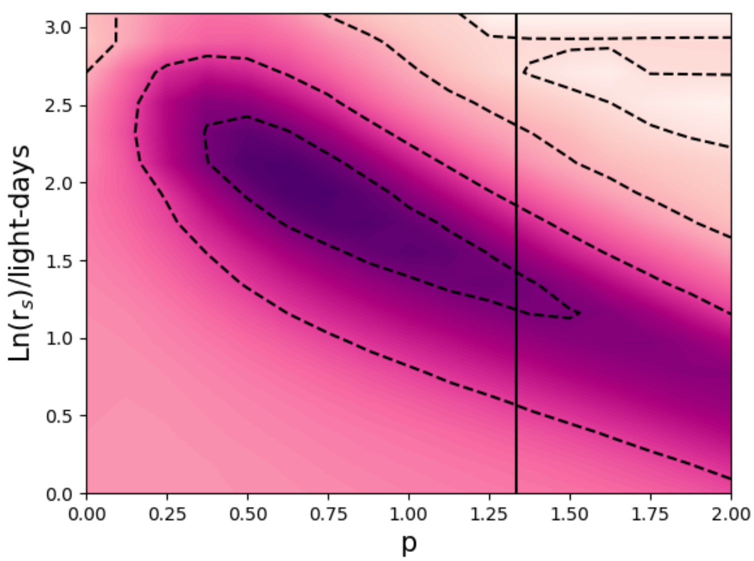

Figure 4.18: Probability density function for the chromatic microlensing measurements in Q1355-2257. Contours correspond to 0.5σ, 1σ, 1.5σ, and 2σ respectively. The black solid line shows the value for p by Shakura & Sunyaev (1973).

4.1.9 SDSS1029+2623 results

This subsection is based on the article in preparation: 'Microlensing Analysis for SDSS0924+0219, Q1355-2257, and SDSS1029+2623' **Rojas K.**, *Motta V., Mediavilla E., Falco E., J. Jimenez-Vicente.*

This system was discovered by Inada et al. (2006) with the source at z_s=2.197. It was thought to be a double system with a large separation between A and B (22.5 arc-seconds), but Oguri et al. (2008) discovered a third component separated 1.8 arc-seconds from the B component. The big separation between A and B is because the lens is a cluster of galaxies at z_l=0.58 (Oguri et al. 2008).

We present our own analysis for the spectra showed in Oguri et al. (2008). The line profiles (Figure 4.19) show strong absorptions in the case of Lyα and CIV. For that reason, we used small windows to integrate the line flux, and in the case of CIV, we split the analysis into two windows (Table 4.12).

Table 4.12: SDSS1029+2623 Magnitude differences

Region	λ (Å)	Window (Å)	m_C-m_B (mag)
continuum	3905	3640-4250	2.09 $\pm$ 0.03
	4900	4700-5200	1.84 $\pm$ 0.01
	4972	4700-5200	1.82 $\pm$ 0.01
	6103	5800-6420	1.67 $\pm$ 0.01
	8942	8300-9417	1.35 $\pm$ 0.02
Line	lyα	3890-3920	2.04 $\pm$ 0.04
	CIV (1)	4878-4923	1.88 $\pm$ 0.01
	CIV (2)	4960-4985	1.84 $\pm$ 0.02
	CIII	6083-6123	1.65 $\pm$ 0.02
	MgII	8925-8960	1.40 $\pm$ 0.02

The differences between the core of the emission line and the adjacent continuum are negligible (Figure 4.20), this is evidence of no microlensing effect in the spectra in that epoch (December 2007). The broad bands presented in Oguri et al. (2008) where taken in November 2006 (B), May 2007 (VRI), and January 2008 (g, and R) respectively. The B band follows the trend of the spectroscopic data, but the rest of the bands show an offset of $\sim$ 0.2 mag. The displacement is not attributed to microlensing variation in separate epochs because almost all broad band measurements from 2006-2007 are in agreement with those taken in 2008. To investigate whether

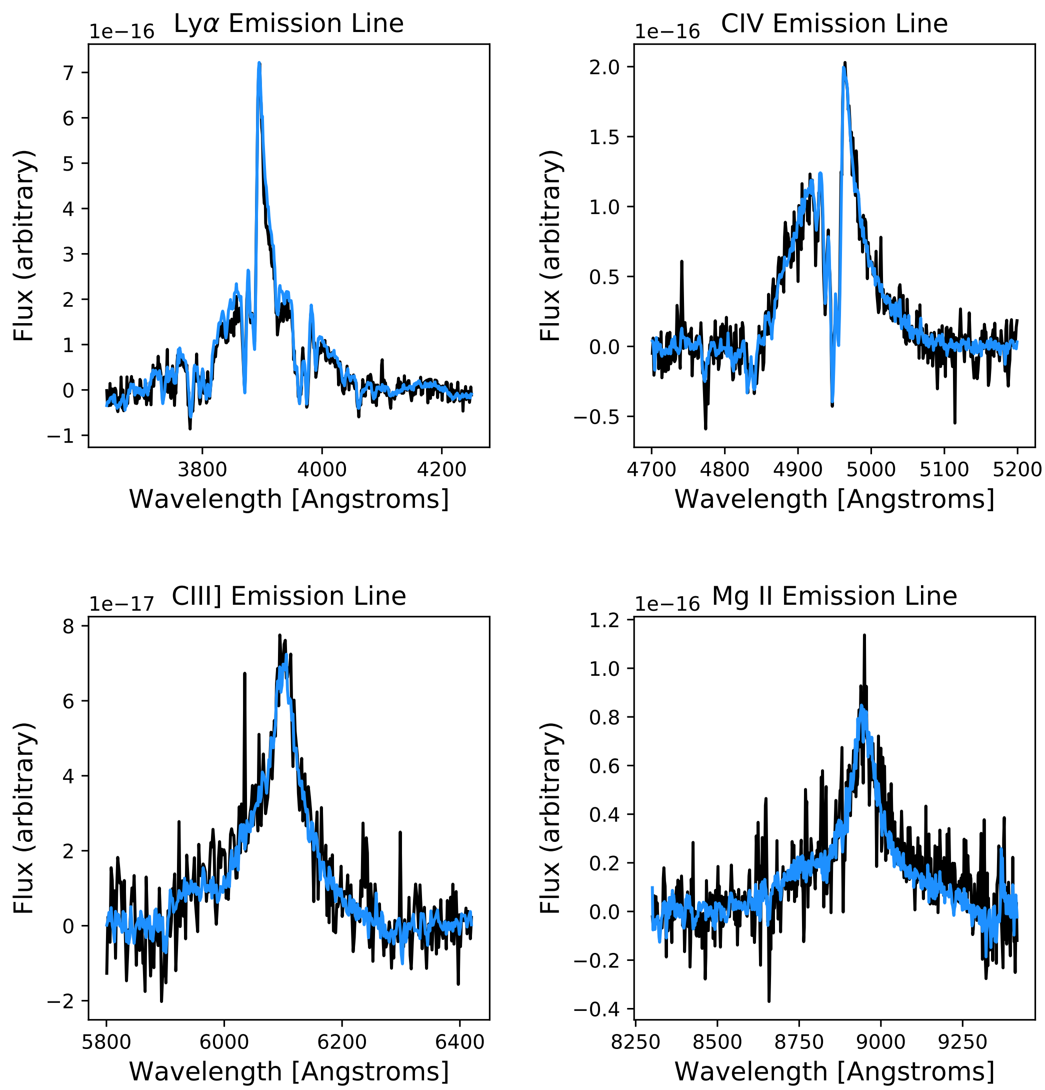

Figure 4.19: Ly α, CIII], CIV, and MgII emission lines profiles without the continuum for SDSS1029+2623. In blue the A component and in black the B component multiply by a factor of 6.0 (Ly α), 5.5 (CIII]), 4.8 (CIV), and 3.5 (MgII].

the emission lines are affecting the broad band measurements, we integrated the spectra in the same wavelength range of the V,R,I,g, and R bands. However, no shift is detected in the integrated continuum. A possible explanation is flux loss in the spectra (e.g. $\sim$10% in B component), producing a displacement in the data.

Figure 4.20 shows that the magnitude differences for both lines and continua decrease towards red wavelengths, which can be explained as dust extinction produced by a galaxy in the vicinity of C component (Oguri et al. 2013). The possibility of extinction was previously analyzed by Oguri et al. (2008), obtaining $\Delta E \sim 0.15$-0.2 using $R_V = 3.1$, and Ota et al. (2012), giving $\Delta E \sim 0.17$ at $z_l = 0.584$. We used the spectroscopic data to perform a new extinction analysis under the assumptions that the absorber is the galaxy in the vicinity of C component. Considering the absence of microlensing, we combine both the emission line and continuum magnitude differences to fit an extinction curve at the redshift of the lens. We present two cases, for the first one we left R_V as a free parameter and for the second one we fix $R_V = 3.1$, which corresponds to the value of our galaxy. The best fit parameters for the first case are: $\Delta M_0 = 1.1 \pm 0.1$, $\Delta E = 0.33 \pm 0.08$, and $R_V = 4.1 \pm 0.4$, with $\chi_{red} = 8.8$. For the second case the best fit parameters are: $\Delta M_0 = 1.25 \pm 0.03$, and $\Delta E = 0.17 \pm 0.01$, with $\chi_{red} = 11.8$. In the second case our results are in agreement with Oguri et al. (2008) and Ota et al. (2012).

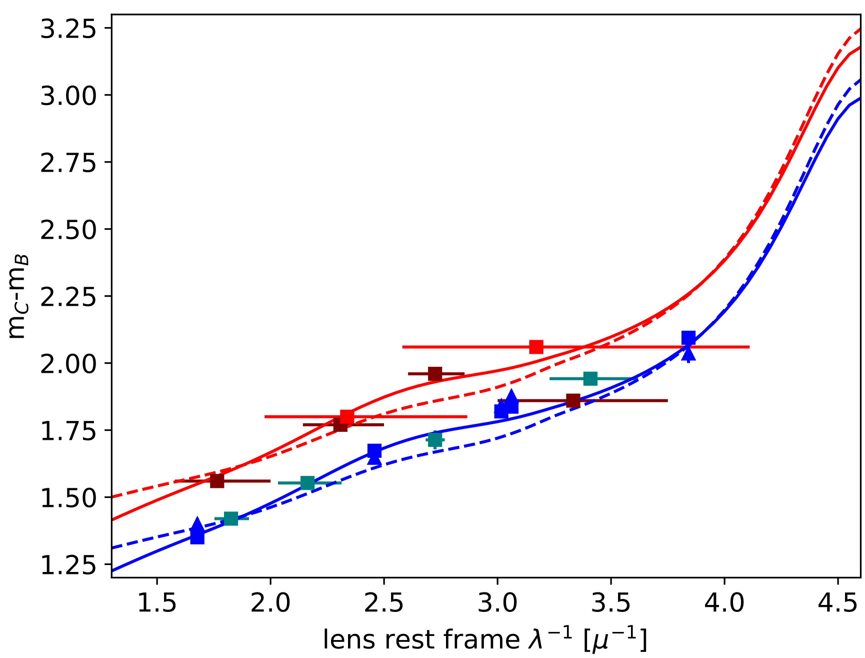

Figure 4.20: Magnitude differences $m_C - m_B$ as a function of wavelength in the lens rest frame for SDSS1029+2623. The triangles are the values for the emission line cores without continuum and the squares are the continuum integration from the spectra or band, depending of the data set. Blue and light blue symbols are measurements from the spectra. Data from Oguri et al. (2008) is plotted in red (bands g and R, taken in 2008 with Keck telescope) and in maroon (bands, B, V, R, and I, taken in 2006-2007 with UH88 telescope). The Blue solid line is the extinction curve fitted to the spectroscopic data. The Red solid line is the extinction curve displaced 0.18 magnitudes.

4.1.10 Conclusions

We used spectroscopic data in image pairs of the lensed quasars to study the flux anomalies in the systems: HE0047-1756 (AB), SDSS1155+6346 (AB), SDSS0924+0219 (BC), Q1355-2257(AB), and SDSS1029+2623(BC). Comparing the magnitude differences of the core of the emission lines with those of the continua we found chromatic microlensing in four of the five systems, thus, we estimate the accretion disk size and temperature profile, obtaining the following results:

HE0047-1756: $r_s = 5^{+6}_{-3}$ light days and p = 2.3 ± 0.8 at $\lambda_{rf} = 2045$ Å.

SDSS1155+6346: $r_s = 10^{+15}_{-6}$ light days and p = 1.5 ± 0.6 at $\lambda_{rf} = 1398$ Å.

HE2149-2745: $r_s = 8^{+11}_{-5}$ light days and p = 0.5 ± 0.3 at $\lambda_{rf} = 1310$ Å.

SDSS0924+0219: $r_s = 7^{+3}_{-2}$ light-days and $p = 0.7 \pm 0.2$ at $\lambda_{rf} = 3533$ Å.

Q1355-2257: $r_s = 4^{+4}_{-2}$ light-days and $p = 1.1 \pm 0.5$ at $\lambda_{rf} = 3533$ Å. This is the first estimation of the accretion disk size and temperature profile for this system.

In all of the cases the sizes estimated are larger than the predicted by the thin disk model (Shakura & Sunyaev 1973). The temperature profile (p index) in the case of HE0047-1756, SDSS1155+6346, and Q1355-2257 are consistent, within errors, with the predictions of the thin disk theory (p=4/3), but in the case of SDSS0924+0219 and HE2149-2745 are significantly smaller. Jiménez-Vicente et al. (2014) present an average estimation for these parameters using 10 image pairs from 8 lensed quasar, they obtained p=0.75 ± 0.2, and r_s=$4.5^{+1.5}_{-1.2}$ light-days. Our sizes estimations are in agreement within errors, with the average r_s presented in Jiménez-Vicente et al. (2014). However, for our systems we obtain that p is in agreement. To improve the estimation of r_s and p we need to increase the number of image pairs studied. A significant statistical analysis requires to increase the lens quasar sample.

Finally, in the case of SDSS1029+2623 we do not found evidence of microlensing or chromatic microlensing but we found extinction ($R_V = 3.1$, $\Delta E = 0.17 \pm 0.01$).

4.2 The effect of microlensing in quasar light-curves

This subsection is based on the publications:

*(1) 'COSMOGRAIL XVI: Time delays for the quadruply imaged quasar DES J0408-5354 with high-cadence photometric monitoring' F. Courbin, V. Bonvin, E. Buckley-Geer, C.D. Fassnacht, J. Frieman, H. Lin, P.J. Marshall, S.H. Suyu, T. Treu, T. Anguita, V. Motta, G. Meylan,E. Paic, M. Tewes, A. Agnello, D.C.-Y. Chao, M. Chijani, D. Gilman, **K. Rojas**, P. Williams, A. Hempel, S. Kim, R. Lachaume, et al. 2018, A&A, Volume 609, id.A71, 9 pp.*

*(2) COSMOGRAIL XVII: Time delays for the quadruply imaged quasar PG 1115+080. V. Bonvin, J. H. H. Chan, M. Millon, **K. Rojas**, F. Courbin, A. Hempel, S. Kim, R. Lachaume, M. Rabus, C. F. Chen, C. D. Fassnacht, E. Paic, M. Tewes, E. Buckley-Geer, J. Frieman, P.J. Marshall, G. Meylan, S.H. Suyu, T. Treu, T. Anguita, V. Motta, accepted for publication in MNRAS.*

*(3) Constraining the microlensing effect on time delays with new time-delay prediction model in H_0 measurements. Geoff C.-F. Chen, Christopher D. Fassnacht, James H. H. Chan, Vivien Bonvin, **Karina Rojas**, Martin Millon, Fred Courbin, Sherry H. Suyu, Kenneth C. Wong, Dominique Sluse, Tommaso Treu, Anowar J. Shajib, Jen-Wei Hsueh, David J. Lagattuta, John P. McKean. Submitted to MNRAS*

Time delay (Δt) in strong lensed quasars offers an independent measurement of the expansion rate of the Universe, called the Hubble Constant (H_0, see Section 2.2). This simple method have the potential to break the degeneracies in the estimation of cosmological parameters, and as it is an independent probe that do not depend on the nature of the matter, can solve the tension between the measurements provided by the Cosmic Microwave Background (CMB) using WMAP satellite ($H_0 = 70.0 \pm 2.2 kms^{-1}Mpc^{-1}$, Bennett et al. (2013)), using Planck satellite ($H_0 = 66.93 \pm 0.62 kms^{-1}Mpc^{-1}$, Planck Collaboration et al. (2016)), the Baryon Acoustic Oscillations (BAO) combined with CMB ($H_0 = 67.6 \pm 0.5 kms^{-1}Mpc^{-1}$, Alam et al. (2017)), the Dark Energy Survey combined with BAO ($H_0 = 67.2^{+1.2}_{-1.0} kms^{-1}Mpc^{-1}$, DES Collaboration et al. (2017)), and calibration of various distance indicators ($H_0 = 73.45 \pm 1.66 kms^{-1}Mpc^{-1}$, Riess et al. (2018)), where some values are in tension with the standard cosmological model (ΛCDM).

Time delay is related with H_0 by: $\Delta t \propto H_0^{-1}(1- < \kappa >)$ (see Equation 2.16), where κ is the mean surface density. This method, proposed by Refsdal (1964a), consist on measuring the time delays between the luminosity variation between different images of the lensed quasar. This imply a monitoring of months or even years, to be able to match the features in a light curve.

The COSmological MOnitoring of GRAvItational Lenses (COSMOGRAIL[4]) collaboration is aimed to measure high-precision time delays of known lensed quasars, using optical light curves in a 6-7 month of monitoring. Thus, to be able to recognize and match the different features of the quasar, an almost daily cadence is needed. The goal of measuring time delays with an accuracy below 3% is to obtain a precise value of H_0 and compare with the other independent probes mentioned before.

The monitoring observation started in 2016 using the instrument WFI at ESO MPIA 2.2m telescope, La Silla Observatory (PI: Courbin). I participated as an observer during the following runs: April 10th-12th 2017, April 2nd-10th 2018, June 28th-31th. Using these observations and combining with data from other telescopes we obtain complete light curves. To find the time delay we shift the light curves using PyCS[5]. So far, we have the estimations for two quadruple systems DESJ0408-5354 (Courbin et al. 2018) and PG1115+080 (Bonvin et al. 2017).

We estimate that the time delay for DESJ0408-5354 is: $\Delta t(AB) = -112 - 1 \pm 2.1$ days (1.8% precision), using only MPIA 2.2m data, and adding 1.2m Euler Swiss telescope we also obtain the delay with respect to D component: $\Delta t(AD) = -155.5 \pm 12.8$ days (8.2%) and $\Delta t(BD) = -42.4 \pm 17.6$ days (41%) (Courbin et al. 2018, see Figure 4.21). For PG1115+080 we combine our data with Mercator telescope at La Palma Observatory, Maidanak telescope in Uzbekistan (Tsvetkova et al. 2010), and the Hiltner telescope, WIYN[6], both in USA, the Nordic Optical Telescope (NOT) at La Palma Observatory, and the Du Pont telescope at Las Campanas Observatory (Schechter et al. 1997). We obtain: $\Delta t(AB) = 8.3^{+1.5}_{-1.6} days$ (1.8% precision), $\Delta t(AC) = 9.9^{+1.1}_{-1.1} days (11.1\%)$, and $\Delta t(BC) = 18.8^{+1.6}_{-1.6} days (8.5\%)$ (see Bonvin et al. 2018). Figure 4.22 shows the light curves, where A is the merged flux of A1 and A2 because both components are too close to perform a proper deconvolution.

Tie & Kochanek (2018a) have recently pointed out that microlensing could affect the accuracy of the time delay measurements. This is because when the accretion disk of the quasar is differently magnified by microlenses, an extra delay in the features

[4] www.cosmograil.org

[5] PyCS can be obtained from www.cosmograil.org

[6] University of Wisconsin–Madison, Indiana University, Yale University, and the National Optical Astronomy Observatories consortium telescope.

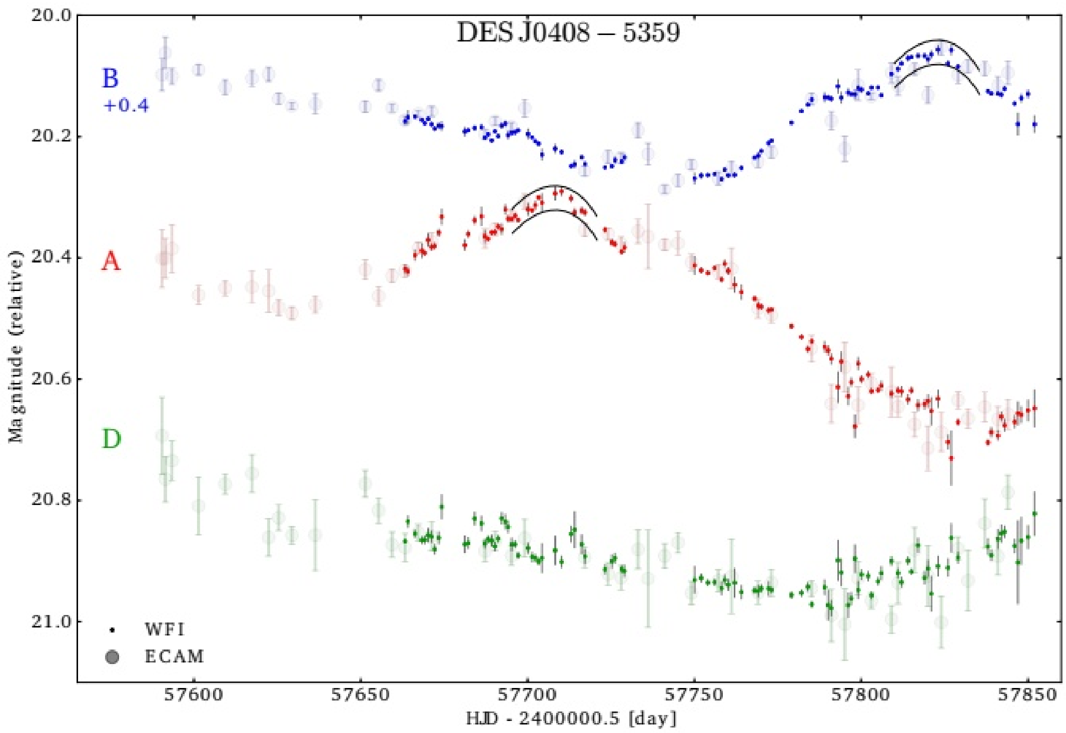

Figure 4.21: DESJ0408-5354 light curves obtained with R_c filter, taken from Courbin et al. (2018). Thin symbols are the observations obtained with MPIA 2.2m telescope and thicker symbols are the observations obtained with 1.2m Euler telescope. The solid black lines are showing the most distinguishable structure in A and B images that match the time delay between them.

of the quasar light curves could be introduced. We reproduced the procedure and analysis presented by Tie & Kochanek (2018a) for the systems RXJ 1131-1231 and HE0435-1223 and apply it to PG1115+080.

4.2.1 Method

We assumed a non-relativistic thin disk model (Shakura & Sunyaev 1973) to model the accretion disk, as in the previous section. The size of the emitting region at a rest frame wavelength (λ_{rf}) is:

$$R_0 = 9.7 \times 10^{15} \left(\frac{\lambda_{rf}}{\mu m}\right)^{4/3} \left(\frac{M_{BH}}{10^9 M_\odot}\right)^{2/3} \left(\frac{L}{\eta L_E}\right)^{1/3} cm, \tag{4.1}$$

where M_{BH} is the mass of the supermassive black hole, L/L_E is the luminosity in Eddington luminosity units, and η is the accretion efficiency. To consider an inclined

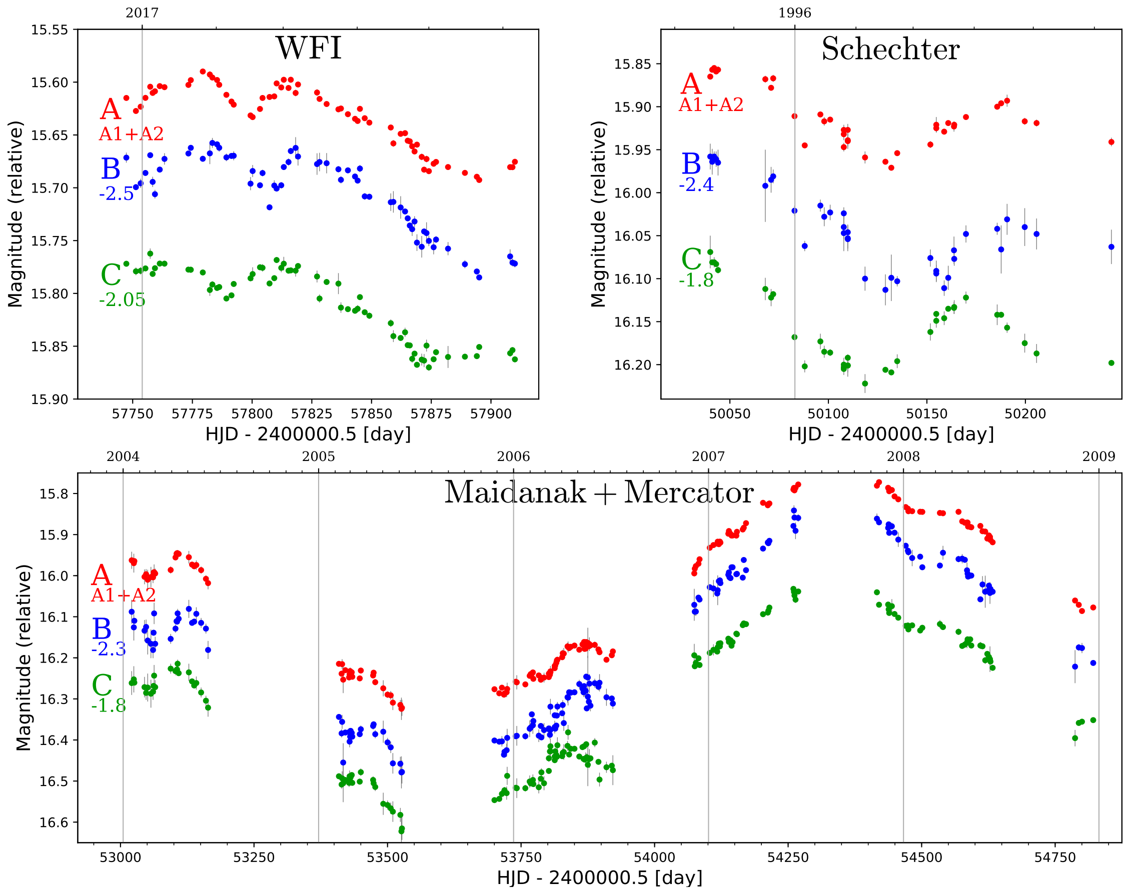

Figure 4.22: PG1115+080 light curves, taken from Bonvin et al. (2018). We present 4 data sets: WFI/MPIA 2.2m telescope data, Mercator, Schechter and Maidanak, this last two data sets where presented on Schechter et al. (1997) and Tsvetkova et al. (2010). Mercator and Maidanak data overlap during 2006 season. The A component is the integrated flux of the unresolved A1 and A2 images. B and C have been shifted in magnitud for visual purposes.

disk relative to the line of sight by an angle i and a position angle θ, we used the rotation matrix: (u, v, w)= R(cosθ cos i, sinθ, cosθ sin i). Then, when $i = 0$ we have a face-on disk.

We also add the effect of the lamp-post model (Cackett et al. 2007), where the temperature variations are correlated with the luminosity. I.e., the temperature changes are propagated along the disk from the center to the edge. This variations are lagged by the time that takes to go from the center to the edge, being longer for a large disk. The variable surface brightness is defined as:

$$G(\xi) = \frac{\xi exp(\xi)}{(exp(\xi)-1)^2}, \quad with \quad \xi = \left(\frac{R}{R_0}\right)^{3/4}\left(1-\sqrt{\frac{R_{in}}{R}}\right)^{-1/4}, \tag{4.2}$$

where $R > R_0$, and R_{in} is the inner edge of the disk (we considered $R_{in} = 0$ in these calculations). For a no microlensing case, we obtained the mean lag between the driving perturbation and the observed light curve: 5.04(1+z_s)R_0/c. On the other hand, when we have a microlensing magnification pattern, the region of the accretion disk will be non-uniformly magnified. To characterize the effect of microlensing we average the delays over $G(\xi)$ and weight them by the absolute value of the microlensing magnification map $M(u, v)$ projected in the source plane, where u and v are the observed coordinates in the lens plane. Then, the average microlensing time delay is:

$$< \delta t >= \frac{1+z_s}{c}\frac{\int dudvG(\xi)M(u,v)R(1+cos\ \theta sin\ i)}{\int dudvG(\xi)M(u,v)}. \tag{4.3}$$

To create the magnification maps we used GPU accelerated implementation of the inverse ray-shooting technique (Wambsganss et al. 1992; Vernardos et al. 2014). The maps have a size of 8192x8192 pixels, 20 R_E, a mean microlens mass of 0.3 $M_\odot$ and a Salpeter mass function as described in Kochanek (2004). These characteristics are the same as in Tie & Kochanek (2018a), in order to reproduce their results. We also used the model parameters described in there for RXJ1131-1231 and HE0435-1223, but we selected Chen et al. (2018) values for PG1115+080

To describe the disk, we considered the R-band (6586Å), $L/L_E = 0.1$, and $\eta = 0.1$, for all the systems. We studied four different inclination and position angle configurations. For RXJ 1131-1231 and HE 0435-1223 we selected the same presented in Tie & Kochanek (2018a): i) $i = 0°$, $PA = 0°$, ii) $i = 30°$, $PA = 0°$, iii) $i = 30°$, $PA = 45°$, vi) $i = 30°$, $PA = 90°$, and for PG1115+080 we followed Morgan et al. (2008), that used $i = 60°$, then we selected: i) $i = 0°$, $PA = 0°$, ii) $i = 60°$, $PA = 0°$, iii) $i = 60°$, $PA = 45°$, vi) $i = 60°$, $PA = 90°$, . Furthermore, we investigate the effect of the size of the accretion disk, considering three cases: $0.5R_0$, R_0, and $2R_0$. An example of a disk with a size R_0 and different inclinations and position angles is shown in Figure 4.23.

We implemented all the procedures described here, including the time delay maps

Table 4.13: Model parameters.

System	Image	κ	γ	κ_*/κ
RXJ 1131-1231	A	0.618	0.412	0.067
	B	0.581	0.367	0.060
	C	0.595	0.346	0.062
	D	1.041	0.631	0.159
HE 0435-1223	A	0.604	0.262	0.050
	B	0.734	0.395	0.080
	C	0.605	0.265	0.050
	D	0.783	0.427	0.093
PG 1115+080	A1	0.424	0.491	0.259
	A2	0.451	0.626	0.263
	B	0.502	0.811	0.331
	C	0.356	0.315	0.203

based on the magnification maps and the statistical analysis, in a simple script[7] available to the community.

4.2.2 Results for the reproduction of RXJ1131-1231 and HE0435-1223 time delay estimations

RXJ1131-1231 is a quadruple strong lens system with $z_s = 0.658$ and $z_l = 0.295$ (Sluse et al. 2003). The black hole mass is $(1.3 \pm 0.3) \times 10^8$ M$_\odot$ (Sluse et al. 2003; Dai et al. 2010). Using the equation 4.1, $R_0 = 7.34 \times 10^{14}$ cm (0.28 light-days) and the Einstein radii is $R_E = 2.52 \times 10^{16}$ (0.3/M$_\odot$) cm (equation. 2.29).

HE0435-1223 is also a quadruple system with $z_s = 1.689$ and $z_l = 0.46$ (Morgan et al. 2005; Ofek et al. 2006). The black hole mass is 0.5×10^9 M$_\odot$ (Mosquera & Kochanek 2011). The accretion disk size is 9.37×10^{14} cm (0.36 light-days), and $R_E = 3 \times 10^{16}$ (0.3/M$_\odot$) cm.

The magnification maps for each image in each system are presented in Figure 4.24 and Figure 4.27. Using the mean (and standard deviation) of the excess of microlensing time delay $< \delta t >$ for each magnification map and source position, we can infer the distribution of $< \delta t >$ for each image of the lensed quasar. We also subtracted the contribution produced by the lamp-post delay (5.04(1+z$_s$)R$_0$/c).

[7] *github.com/Krojas/MeanDelay/blob/master/meandelay.py*

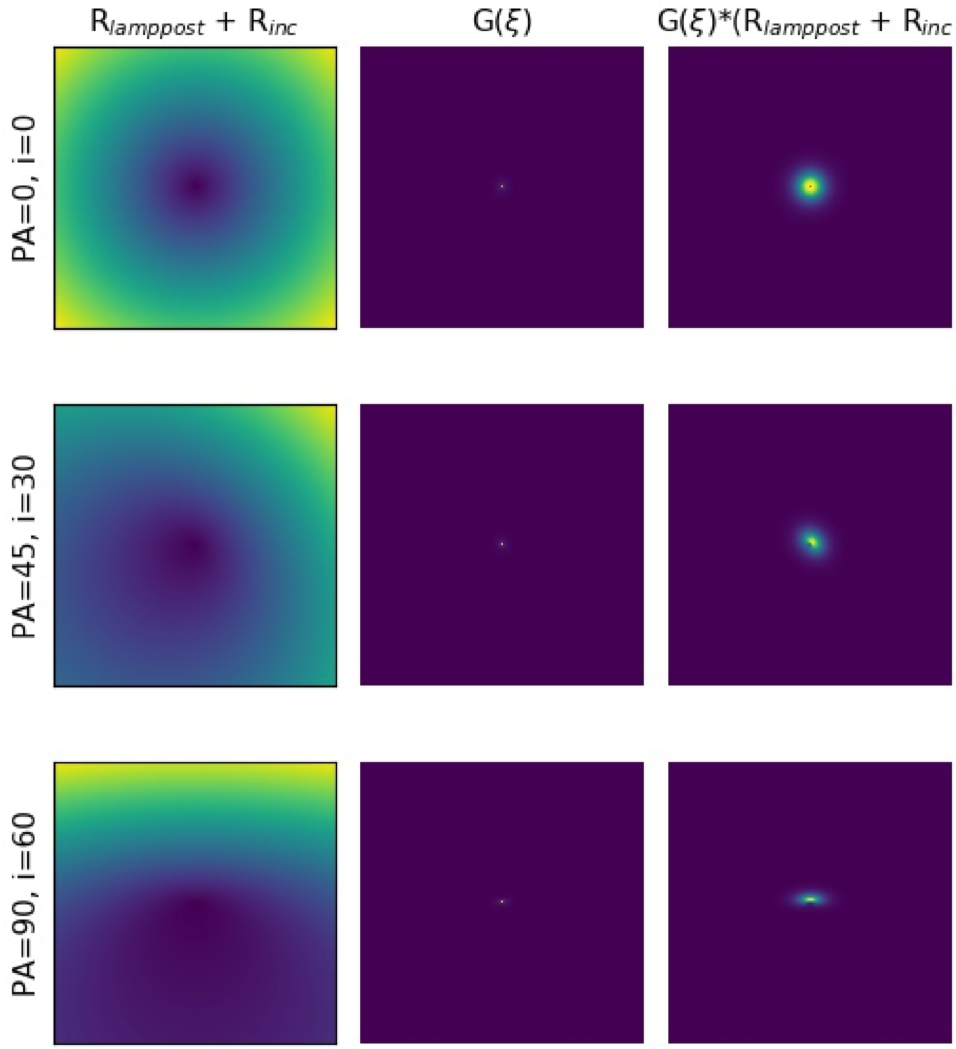

Figure 4.23: Examples of a disk of size R_0 with different position angles and inclinations. The columns represent (left to right): The representation of the disk using the lamp-post model and adding the effect of inclination, the variable surface brightness, and the multiplication of the two previous columns that represent the term $G(\xi)R(1 + cos\ \theta sin\ i)$ in Equation 4.3.

Our microlensing time delay estimations and Tie & Kochanek (2018a) results are presented in Table 4.14 and Figure 4.28. The cumulative distribution, using all the points in the map for a face on disk (first case) is presented in Figure 4.29 and for the cases ii), iii) and iv) in Figure 4.30 and Figure 4.31.

As Table 4.14 and Figure 4.28 show, we were able to reproduce the Tie &

Kochanek (2018a) results. Our values for the time delay are in agreement, within errors, with those presented in Tie & Kochanek (2018a). From these analysis, Tie & Kochanek (2018a) highlight several points: (1) the line of sight (LOS) delays from the disk inclination are symmetric with a mean delay around zero, while the R/c delay depends little on the inclination; (2) the total delay increase from PA 0° to 90°, this is because when the caustics are parallel to the long axis of the disk (PA=90°) it is easier to magnify regions with only one sign (positive or negative) of the delay; and (3) in general the delays are larger for larger sources.

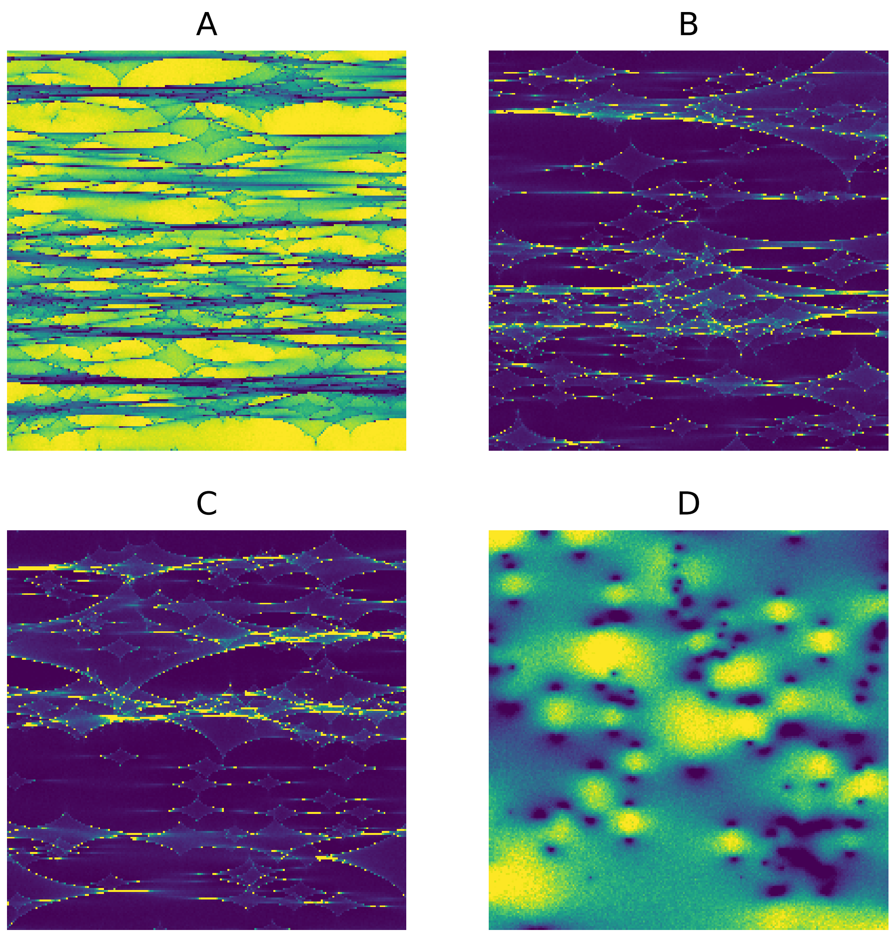

Figure 4.24: Magnification maps for the images A, B, C and D of RXJ1131-1231. The size is 8192x8192 pixel, 20 R_E, and the mean mass of the Salpeter distribution is $0.3M_\odot$

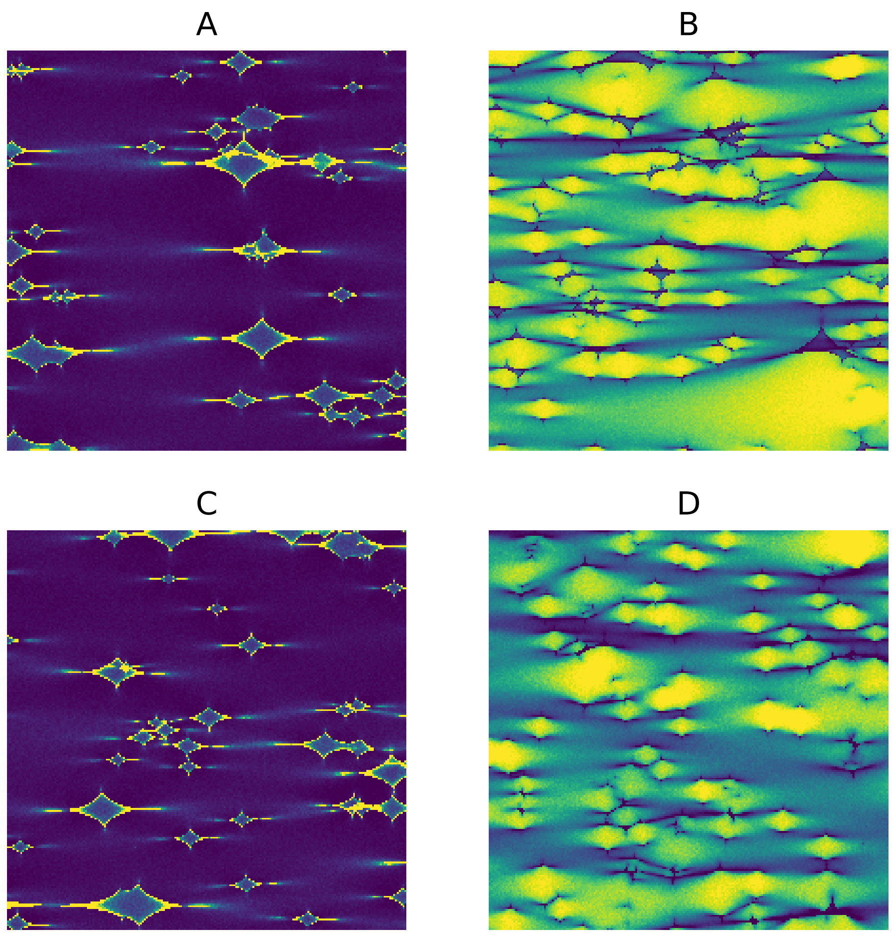

Figure 4.25: Magnification maps for the images A, B, C and D of HE0435-1223. The size is 8192x8192 pixel, 20 R_E, and the mean mass of the Salpeter distribution is $0.3M_\odot$

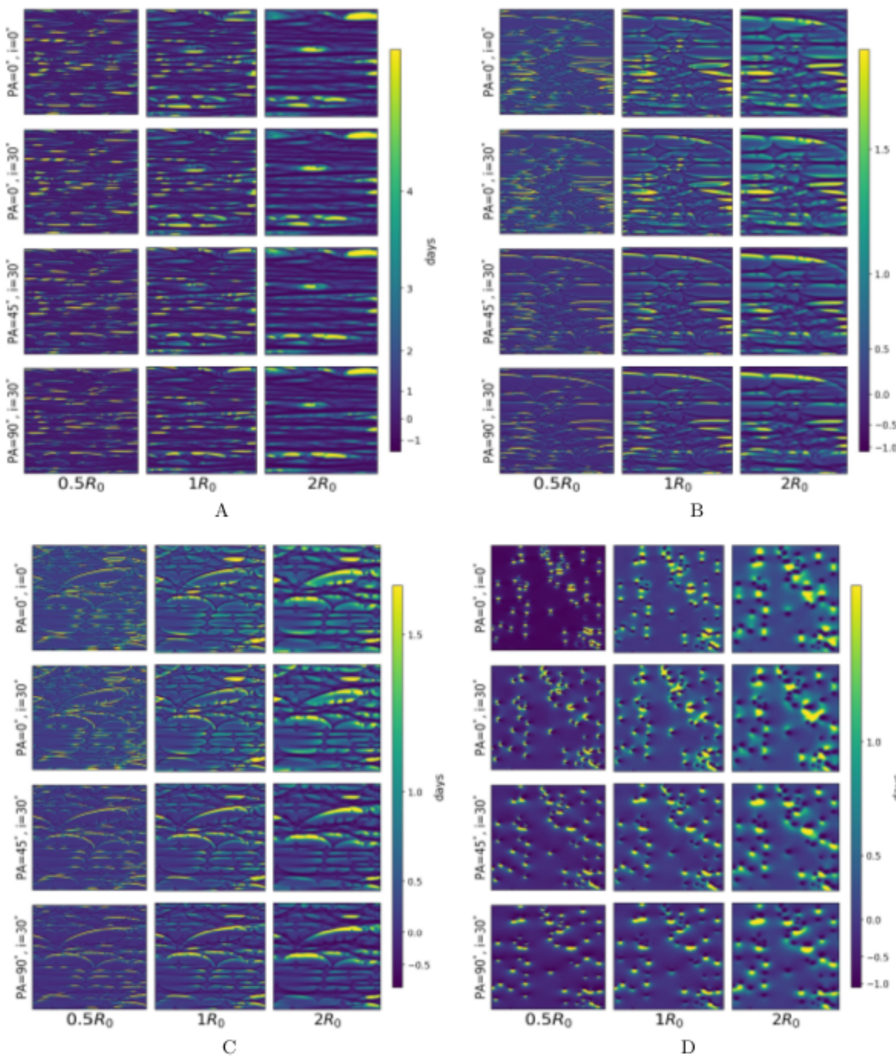

Figure 4.26: Time delay maps for RXJ1131-1231. For each image the top row is the face-on disk, and the other 3 rows are the $i = 30°$, $PA = 0°$, $i = 30°$, $PA = 45°$, $i = 30°$, $PA = 90°$, cases. Each column show a different size since left to right: $0.5\mathrm{R}_0$, $1.0\mathrm{R}_0$, $2.0\mathrm{R}_0$.

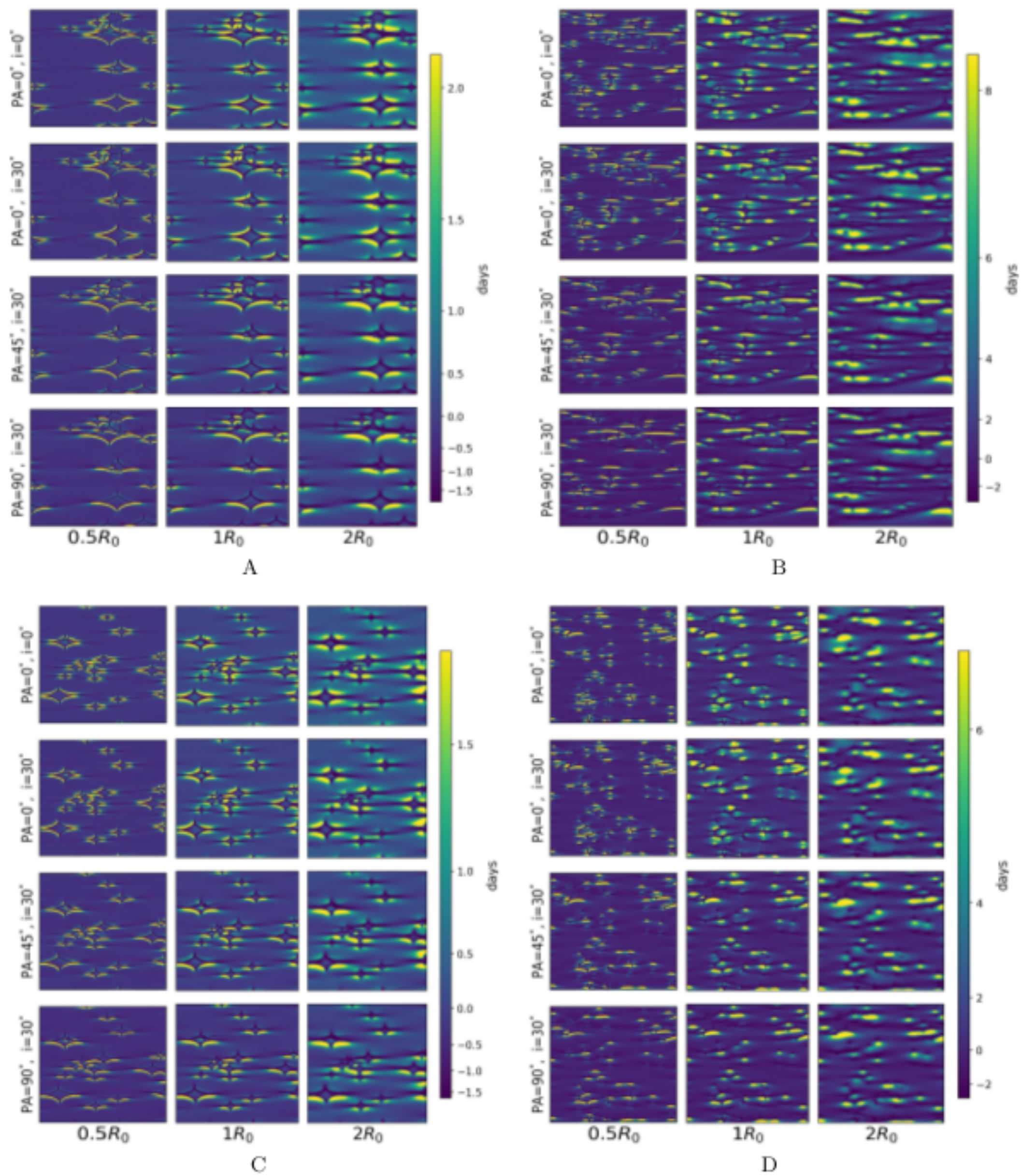

Figure 4.27: Time delay maps for HE0435-1223. For each image the top row is the face-on disk, and the other 3 rows are the $i = 30°$, $PA = 0°$, $i = 30°$, $PA = 45°$, $i = 30°$, $PA = 90°$, cases. Each column show a different size since left to right: $0.5\mathrm{R}_0$, $1.0\mathrm{R}_0$, $2.0\mathrm{R}_0$.

Table 4.14: Mean (dispersion) of microlensing time delay between the different images for RXJ 1131-1231 and HE0435-1223 obtained with our code and by Tie & Kochanek (2018a).

System	Size	PA (°)	i (°)	B-A (days)	C-A (days)	D-A (days)	C-B (days)	D-B (days)	D-C (days)
RXJ1131-1231	0.5 R_0	0	0	-0.124 (0.336)	-0.131 (0.331)	-0.144 (0.318)	-0.007 (0.15)	-0.02 (0.119)	-0.013 (0.103)
(this work)		0	30	-0.123 (0.338)	-0.13 (0.332)	-0.144 (0.32)	-0.007 (0.152)	-0.021 (0.124)	-0.014 (0.107)
		45	30	-0.117 (0.362)	-0.125 (0.355)	-0.139 (0.342)	-0.008 (0.17)	-0.022 (0.139)	-0.014 (0.12)
		90	30	-0.113 (0.396)	-0.121 (0.389)	-0.134 (0.373)	-0.008 (0.189)	-0.021 (0.154)	-0.013 (0.133)
	1.0 R_0	0	0	-0.287 (0.746)	-0.3 (0.731)	-0.314 (0.707)	-0.013 (0.349)	-0.027 (0.297)	-0.014 (0.257)
		0	30	-0.286 (0.747)	-0.299 (0.732)	-0.314 (0.711)	-0.013 (0.354)	-0.028 (0.309)	-0.015 (0.269)
		45	30	-0.281 (0.807)	-0.298 (0.79)	-0.314 (0.767)	-0.017 (0.391)	-0.033 (0.341)	-0.016 (0.299)
		90	30	-0.278 (0.887)	-0.297 (0.869)	-0.313 (0.842)	-0.019 (0.43)	-0.035 (0.373)	-0.016 (0.328)
	2.0 R_0	0	0	-0.53 (1.504)	-0.517 (1.483)	-0.496 (1.465)	0.013 (0.748)	0.034 (0.712)	0.021 (0.666)
		0	30	-0.525 (1.503)	-0.513 (1.481)	-0.497 (1.472)	0.012 (0.756)	0.028 (0.738)	0.016 (0.693)
		45	30	-0.532 (1.65)	-0.534 (1.628)	-0.521 (1.612)	-0.002 (0.835)	0.011 (0.803)	0.013 (0.757)
		90	30	-0.543 (1.817)	-0.555 (1.794)	-0.543 (1.769)	-0.012 (0.916)	0.0 (0.868)	0.012 (0.818)
RXJ1131-1231	0.5 R_0	0	0	-0.08 (0.27)	-0.08 (0.27)	-0.1 (0.25)	-0.0 (0.15)	-0.02 (0.11)	-0.02 (0.11)
(Tie & Kochanek		0	30	-0.08 (0.27)	-0.09 (0.27)	-0.1 (0.26)	-0.0 (0.15)	-0.02 (0.12)	-0.02 (0.11)
2018a)		45	30	-0.08 (0.3)	-0.08 (0.3)	-0.1 (0.28)	-0.0 (0.17)	-0.02 (0.13)	-0.02 (0.12)
		90	30	-0.07 (0.34)	-0.08 (0.33)	-0.09 (0.31)	-0.0 (0.18)	-0.02 (0.14)	-0.02 (0.13)
	1.0 R_0	0	0	-0.25 (0.68)	-0.27 (0.67)	-0.29 (0.64)	-0.01 (0.34)	-0.04 (0.28)	-0.02 (0.27)
		0	30	-0.25 (0.68)	-0.27 (0.68)	-0.29 (0.65)	-0.01 (0.35)	-0.04 (0.29)	-0.02 (0.28)
		45	30	-0.24 (0.74)	-0.26 (0.74)	-0.28 (0.71)	-0.01 (0.38)	-0.04 (0.32)	-0.02 (0.3)
		90	30	-0.24 (0.83)	-0.25 (0.81)	-0.27 (0.78)	-0.01 (0.42)	-0.04 (0.35)	-0.02 (0.33)
	2.0 R_0	0	0	-0.56 (1.57)	-0.61 (1.54)	-0.6 (1.51)	-0.04 (0.77)	-0.03 (0.71)	0.01 (0.65)
		0	30	-0.57 (1.57)	-0.61 (1.55)	-0.61 (1.53)	-0.05 (0.78)	-0.03 (0.74)	0.01 (0.68)
		45	30	-0.57 (1.72)	-0.61 (1.68)	-0.61 (1.66)	-0.04 (0.85)	-0.03 (0.79)	0.01 (0.72)
		90	30	-0.58 (1.88)	-0.62 (1.85)	-0.61 (1.82)	-0.04 (0.93)	-0.04 (0.86)	0.0 (0.78)
HE0435-1223	0.5 R_0	0	0	0.14 (0.426)	-0.001 (0.182)	0.07 (0.305)	-0.141 (0.424)	-0.07 (0.49)	0.071 (0.302)
(this work)		0	30	0.14 (0.433)	0.0 (0.187)	0.07 (0.312)	-0.14 (0.431)	-0.07 (0.498)	0.07 (0.31)
		45	30	0.134 (0.48)	0.002 (0.204)	0.07 (0.353)	-0.132 (0.479)	-0.064 (0.558)	0.068 (0.351)
		90	30	0.128 (0.532)	0.002 (0.224)	0.067 (0.396)	-0.126 (0.531)	-0.061 (0.623)	0.065 (0.395)
	1.0 R_0	0	0	0.434 (1.097)	-0.004 (0.417)	0.249 (0.825)	-0.438 (1.092)	-0.185 (1.304)	0.253 (0.818)
		0	30	0.43 (1.115)	-0.001 (0.427)	0.248 (0.838)	-0.431 (1.109)	-0.182 (1.322)	0.249 (0.83)
		45	30	0.424 (1.214)	0.003 (0.466)	0.255 (0.933)	-0.421 (1.208)	-0.169 (1.453)	0.252 (0.925)
		90	30	0.414 (1.331)	0.003 (0.51)	0.251 (1.039)	-0.411 (1.325)	-0.163 (1.604)	0.248 (1.031)
	2.0 R_0	0	0	0.916 (2.51)	-0.017 (0.915)	0.544 (2.021)	-0.933 (2.492)	-0.372 (3.075)	0.561 (1.999)
		0	30	0.905 (2.53)	-0.005 (0.933)	0.55 (2.037)	-0.91 (2.512)	-0.355 (3.097)	0.555 (2.015)
		45	30	0.943 (2.717)	0.001 (1.007)	0.59 (2.193)	-0.942 (2.694)	-0.353 (3.324)	0.589 (2.165)
		90	30	0.969 (2.971)	0.0 (1.1)	0.615 (2.403)	-0.969 (2.945)	-0.354 (3.639)	0.615 (2.371)
HE0435-1223	0.5 R_0	0	0	0.12 (0.42)	0.0 (0.2)	0.05 (0.31)	-0.12 (0.42)	-0.07 (0.48)	0.05 (0.31)
(Tie & Kochanek		0	30	0.12 (0.43)	0.0 (0.21)	0.05 (0.31)	-0.13 (0.43)	-0.07 (0.49)	0.05 (0.31)
2018a)		45	30	0.12 (0.47)	0.0 (0.23)	0.05 (0.35)	-0.12 (0.48)	-0.07 (0.54)	0.05 (0.35)
		90	30	0.11 (0.52)	0.0 (0.25)	0.05 (0.39)	-0.11 (0.52)	-0.07 (0.6)	0.05 (0.39)
	1.0 R_0	0	0	0.38 (1.06)	0.0 (0.47)	0.21 (0.8)	-0.37 (1.05)	-0.17 (1.24)	0.2 (0.8)
		0	30	0.38 (1.07)	0.0 (0.49)	0.2 (0.81)	-0.38 (1.07)	-0.17 (1.25)	0.2 (0.82)
		45	30	0.37 (1.16)	0.0 (0.54)	0.2 (0.91)	-0.37 (1.17)	-0.17 (1.38)	0.19 (0.91)
		90	30	0.36 (1.28)	0.0 (0.59)	0.18 (1.01)	-0.35 (1.28)	-0.17 (1.52)	0.19 (1.02)
	2.0 R_0	0	0	0.83 (2.38)	0.01 (1.08)	0.65 (2.0)	-0.83 (2.38)	-0.17 (2.92)	0.65 (2.01)
		0	30	0.85 (2.42)	0.0 (1.1)	0.65 (2.03)	-0.83 (2.42)	-0.19 (2.96)	0.65 (2.04)
		45	30	0.85 (2.64)	0.01 (1.21)	0.64 (2.24)	-0.83 (2.64)	-0.2 (3.25)	0.64 (2.25)
		90	30	0.85 (2.87)	0.0 (1.32)	0.61 (2.48)	-0.84 (2.89)	-0.23 (3.57)	0.62 (2.5)

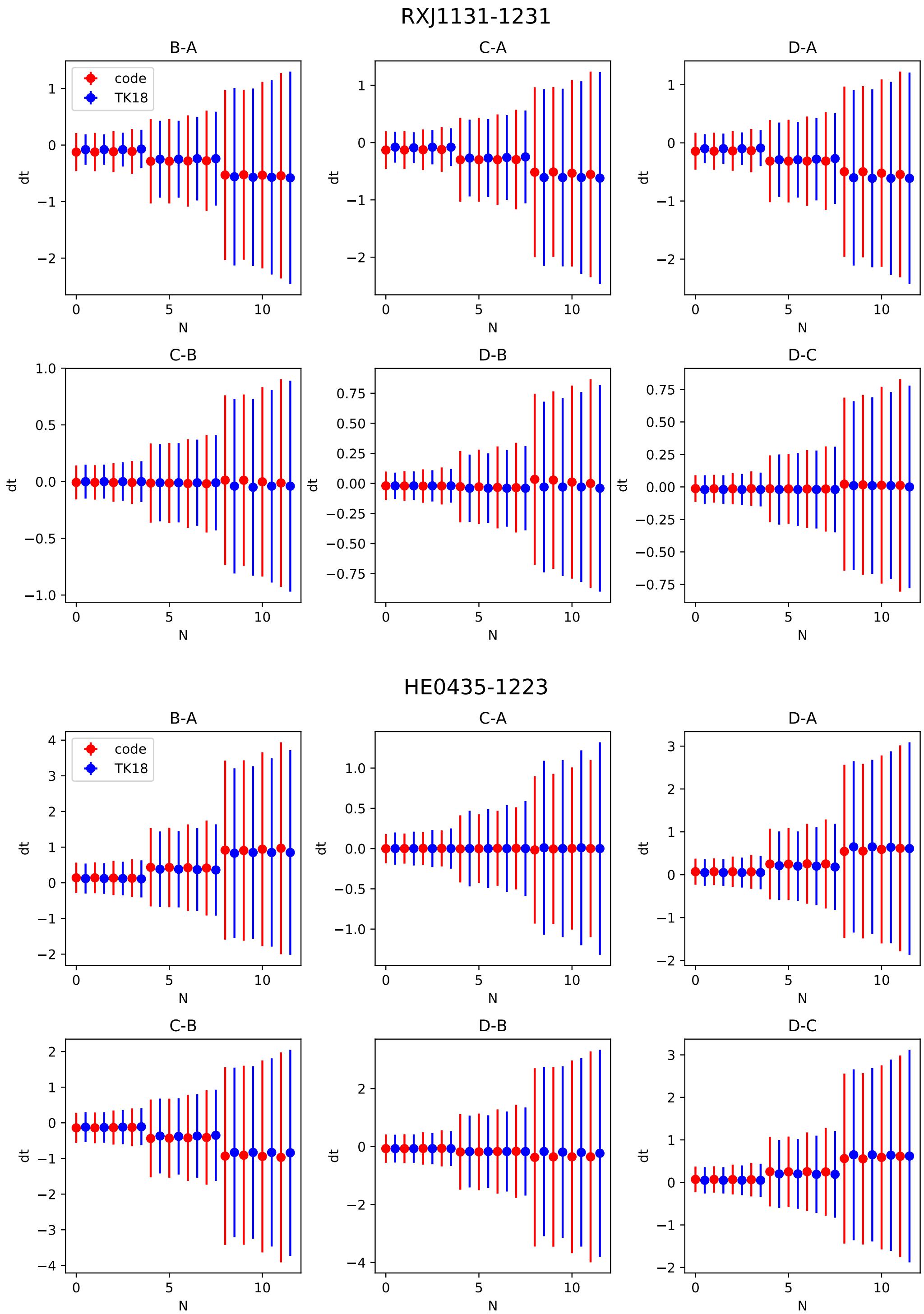

Figure 4.28: Graphical comparison of the values obtained by this work (red) and Tie & Kochanek (2018a) (blue). The x axis is an arbitrary number, the axis y is the mean delay and the error is the standard deviation.

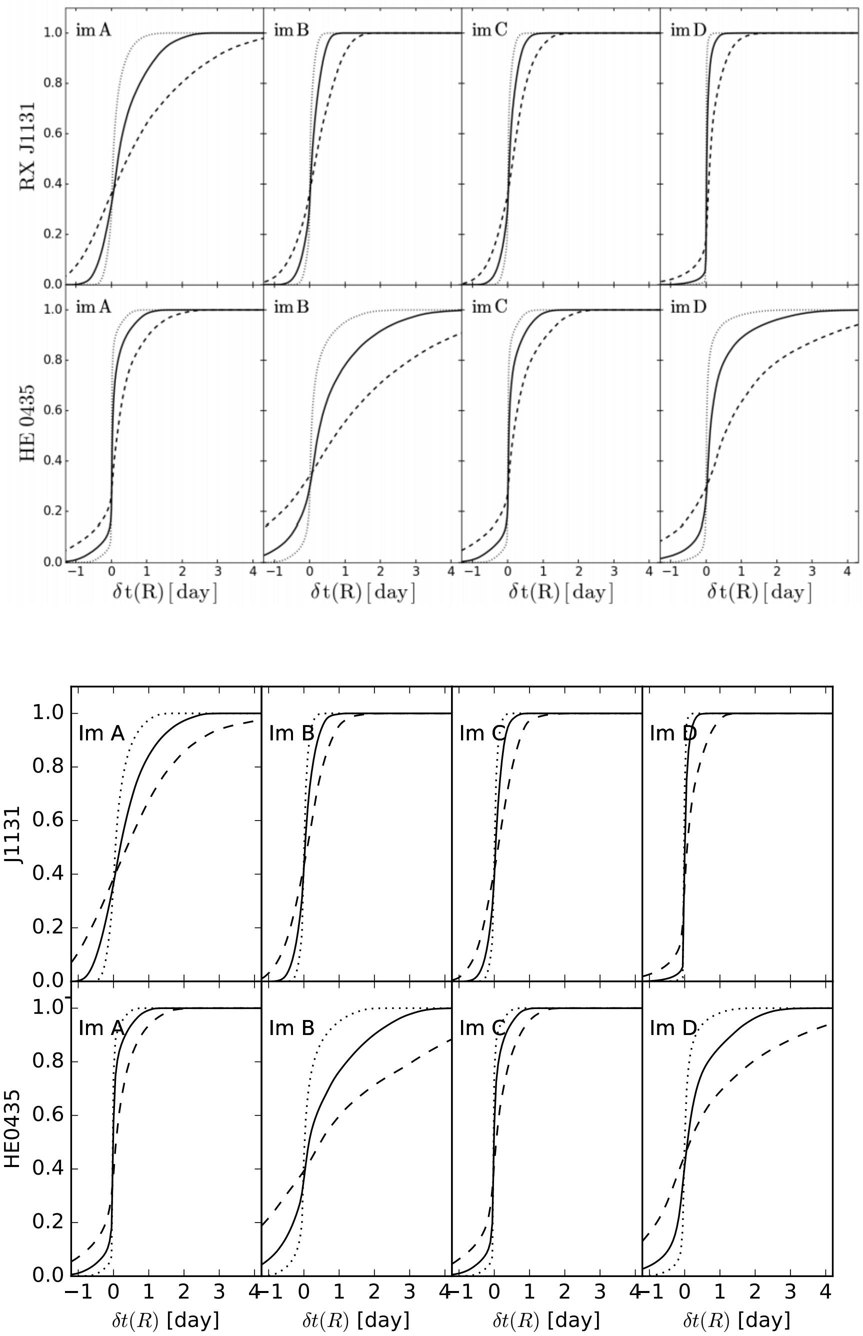

Figure 4.29: Cumulative distribution of microlensing time delays for a face-on disk (i=0, PA=0) for the systems RXJ 1131-1231 and HE0435-1223. Top: plot presented in Tie & Kochanek (2018a). Bottom: Our results, we follow the same line style that in Tie & Kochanek (2018a), where: solid line (R_0), dashed line (2 R_0), dotted line (0.5 R_0).

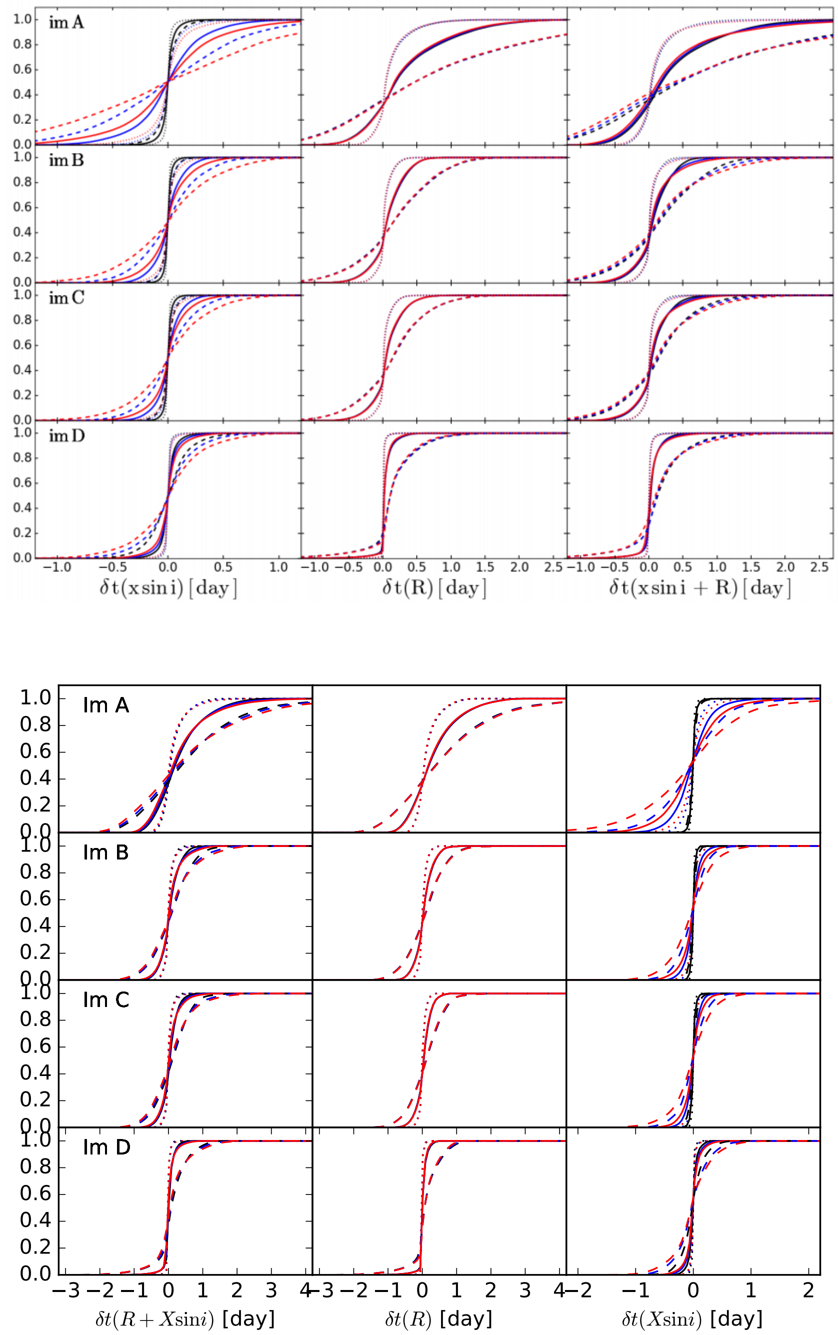

Figure 4.30: Cumulative distribution for RXJ 1131-1231 microlensing time delays estimated with our code using a 30° inclined disk. Top: plot presented in Tie & Kochanek (2018a). Bottom: Our results, for the columns we plot the different component of delay, from right to left: the LOS inclination, R/c, and the combination of both. We follow the same symbols that are in Tie & Kochanek (2018a): The different disk position angles are represented by color: black (PA=0°), blue (PA=45°), and red (PA=90°). The different line styles represent the three different sizes: solid line (R_0), dashed line (2 R_0), dotted line (0.5 R_0).

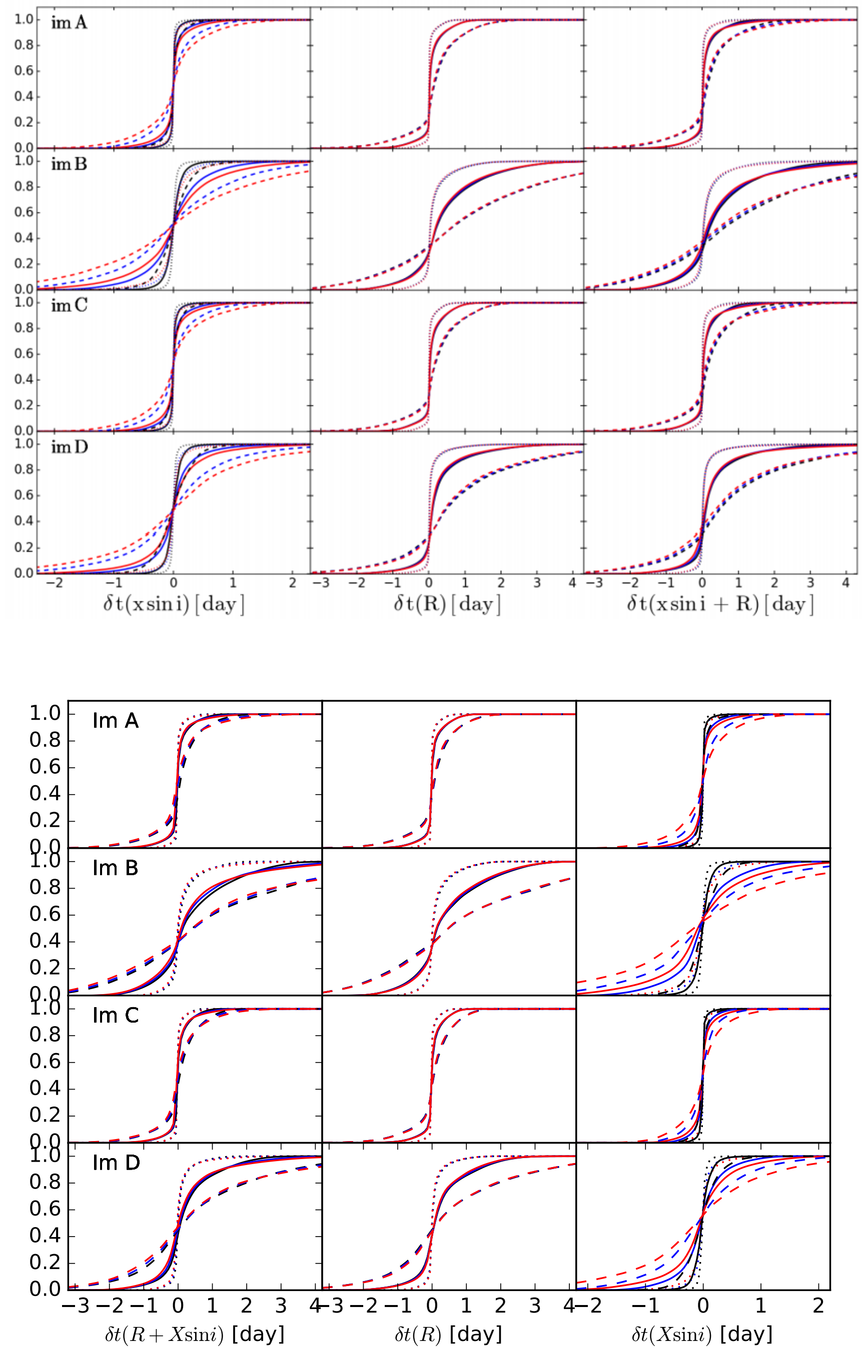

Figure 4.31: Cumulative distribution for HE0435-1223 microlensing time delays. Top: plot presented in Tie & Kochanek (2018a). Bottom: Our results, we follow the same code symbols that in Figure 4.30

4.2.3 Light curve examples

An extra procedure is presented in Tie & Kochanek (2018a), to illustrate the microlensing effect on time delays. Then, to reproduced it we used the Damped Random Walk (DRW) model to simulate the driving light curve for a quasar. We used the python module astroML (Vanderplas et al. 2012; Ivezić et al. 2014). To implement this part of the software we set the time scale $\tau = 90$ days, and the fraction variability in 15%. The lags produced in the light curve are defined by $t_{lag} = (1 + z_s)(R - x \;\; sin \;\; i)/c$, where the flux contribution is $f(t - t_{lag})G(\xi)$. This creates a snapshot of the brightness of the accretion disk at a given time.

We created a light curve of 120 days for RXJ 1131-1231, as in Tie & Kochanek (2018a), and we used the magnification map for image A. We selected two points in the map with different magnification (Figure 4.32). The central position of the image is around the central pixel: (1918,4475) and (5845,6583). The light curves convolved with each region are called LC1 and LC2 respectively. We study two cases: a) a face-on disk (PA=0°, inc=0°), b) an inclined disk (PA=45°, inc=30°). To obtain the microlensing effect on the light curve we multiply the flux contribution with the region of our magnification map.

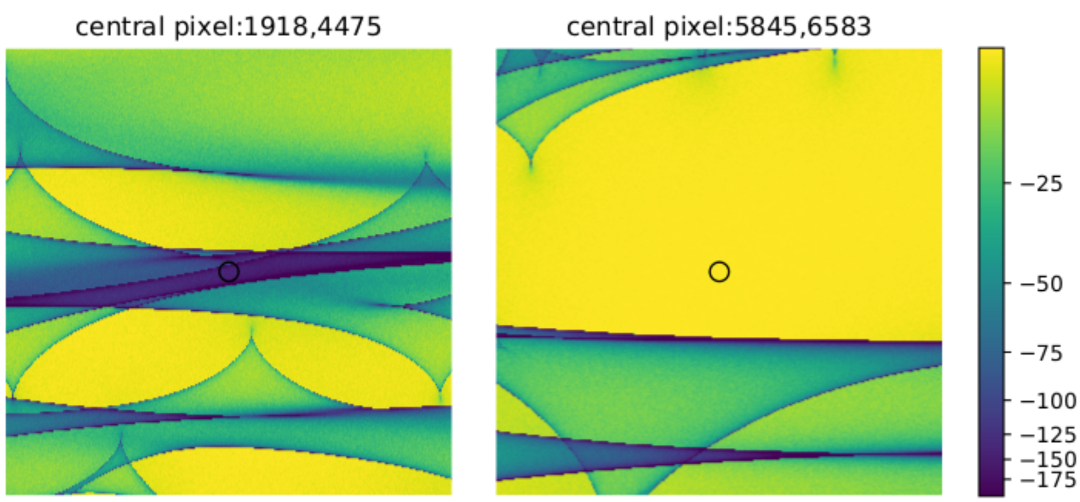

Figure 4.32: Magnification map sections of 1000x1000 pixels around pixel (1918,4475) and (5845,6583). The central circle indicates the center of the image.

In Figure 4.33 we show the effect of microlensing in the light curves. This effect is produced by the disk surface brightness changes through time that are weighted by the microlensing pattern.

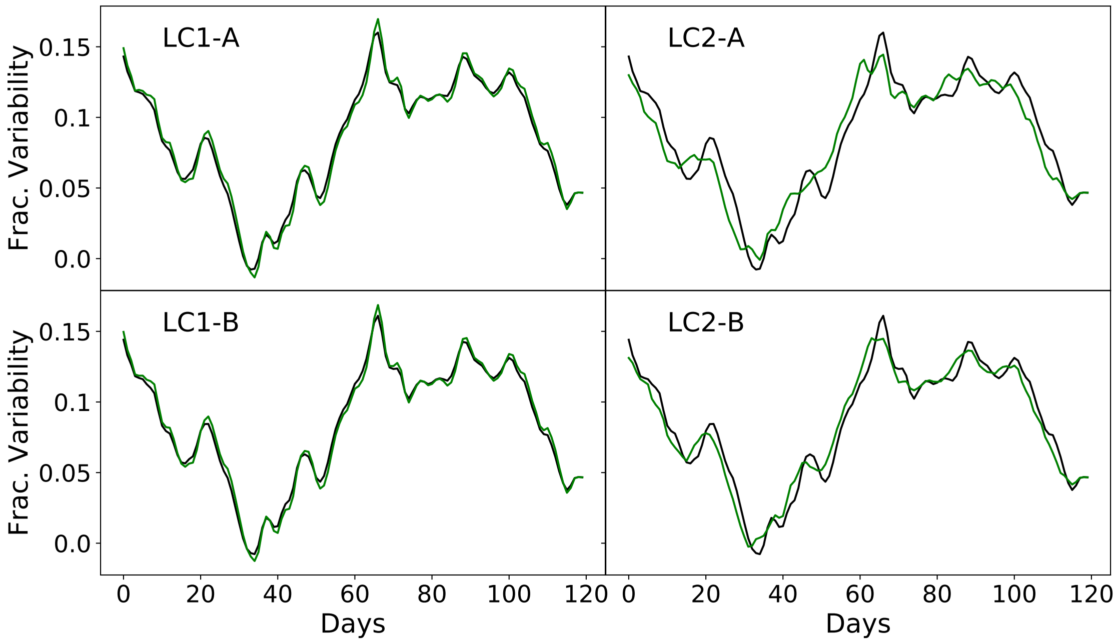

Figure 4.33: Simulated light curve for the lensed quasar RXJ1131-1231. The top panels are for a face-on disk, and the bottom ones are for a 30° inclined disk and 45° position angle. The black solid line represents no-microlensing and the green one is the curve affected by microlensing.

4.2.4 PG1115+080

The second lensed quasar discovered, PG1115+080 is also a quadruple Weymann et al. (1980), where the lensed quasar is at z_s=1.722 and the lens galaxy at z_l=0.311. It is part of a small group of galaxies (Kundic et al. 1997; Tonry 1998). The two bright images have a separation of only ~0.5 arc-seconds and are named A1 and A2. We used the black hole mass estimation of 1.2×10^9 $M_\odot$ made by Peng et al. (2006). To estimate the size of the accretion disk R_0=1.629×10^{15} cm at λ6517.25 $\mathring{A}$ (WFI R_c filter) and the Einstein radii R_E=3.618×10^{16} cm.

We monitored the system with WFI/ESO MPIA 2.2m telescope between December 2016 and July 2017 (Figure 4.22). We study the influence of microlensing time delay on the recent estimated time delays in the images (Bonvin et al. 2018). We start by building magnification maps for A1, A2, B and C (Figure 4.34) as specified in Section 4.2.1 and using the parameters listed in Table 4.13. We use four cases for the disc configuration: i) $i = 0°$, $PA = 0°$, ii) $i = 60°$, $PA = 0°$, iii) $i = 60°$, $PA = 45°$, vi) $i = 60°$, $PA = 90°$, and three different sizes for the disk: 0.5 R_0, 1 R_0, and 2 R_0. The inclination in this case was selected following Morgan et al. (2008). We compute the time delay maps using Equation 4.3 and the description in Section 4.2.1 (Figure 4.35).

Figure 4.36 presents the 16th, 50th, and 84th percentiles of the inferred microlensing time delay distribution. The mean and standard deviation are good approximations only if we have a Gaussian distribution. As Tie & Kochanek (2018a), we also found that for bigger disks the delay produced is larger. The 50th, 16th and 84th percentiles for each image are presented in Table 4.15. To obtain a merged value for A we convolved the A1 and A2 distributions and rescaled the result by a factor 2. In the worst cases, the mean delay for each pair is $< dt >_{AB}$~$0.3^{+4.4}_{-4.5}$ days, $< dt >_{AC}$~$0.6^{+2.3}_{-2.7}$ days, and $< dt >_{BC}$~$0.6^{+2.9}_{-3.8}$ days.

The average microlensing time delay values are small enough to not significantly affect our measured time delays ($\Delta t(AB) = 8.3^{+1.5}_{-1.6}$ days, $\Delta t(AC) = 9.9^{+1.1}_{-1.1}$ days, and $\Delta t(BC) = 18.8^{+1.6}_{-1.6}$ days). Then, we decided against propagating the microlensing delay distributions to the time delay measurements mainly because this estimations are based on strong assumptions that can not be verified experimentally yet. Specifically, the study of chromatic microlensing on lensed quasars, for example, finds an average value for the temperature profile index p=0.8 ± 0.2 (Jiménez-Vicente et al. 2014), which is significantly smaller than the prediction of the thin disk theory. Also accretion disk sizes estimations using chromatic microlensing (Rojas et al. 2014; Motta et al. 2017) and reverberation mapping (Edelson et al. 2015; Lira et al. 2015; Fausnaugh et al. 2016) do not agree with the theory. Then, further work is needed (e.g. larger samle of well studied systems) to determine the real effect and amplitude of microlensing in the estimation of time delays.

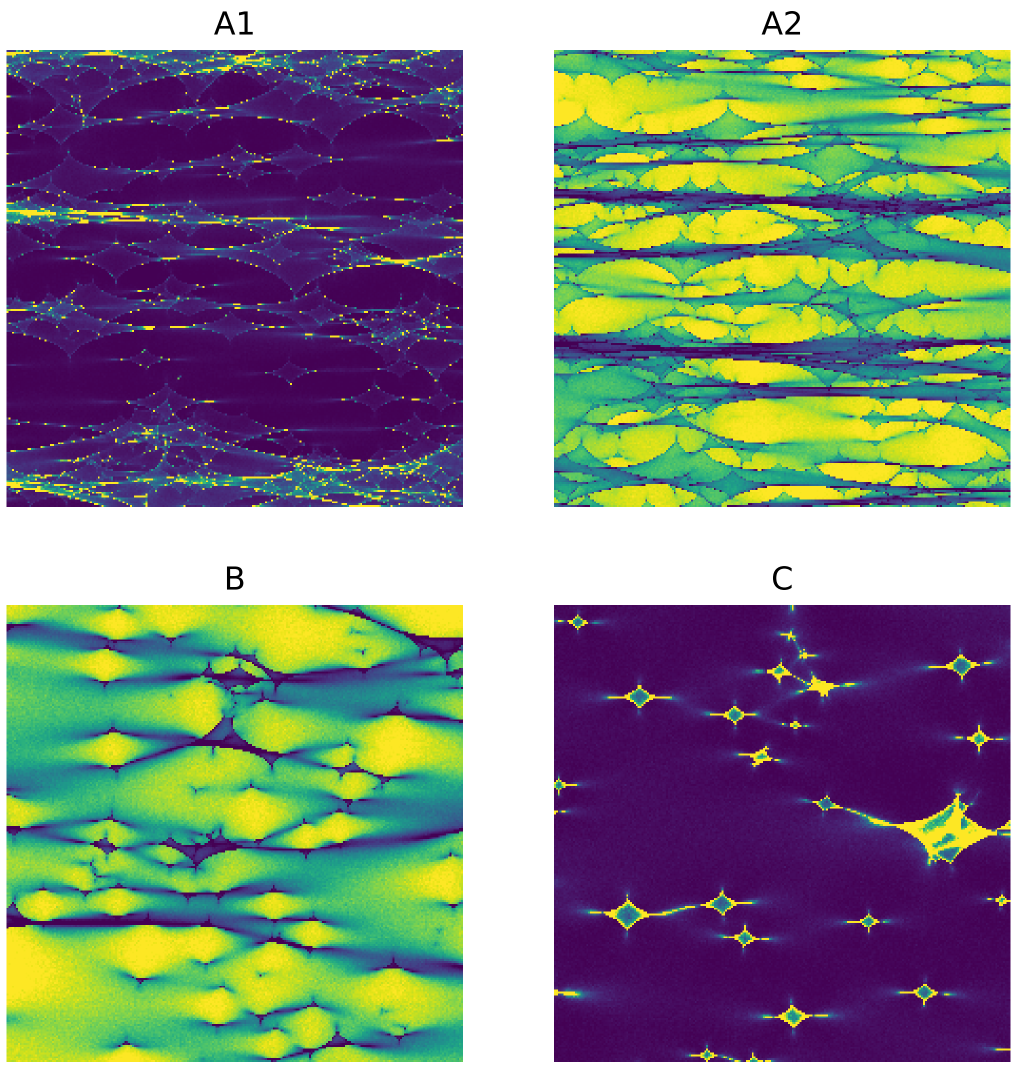

Figure 4.34: Magnification maps for the images A1, A2 B, and C of PG1115+080. The size is 8192x8192 pixel, 20 R_E, and the mean mass of the Salpeter distribution is $0.3M_\odot$

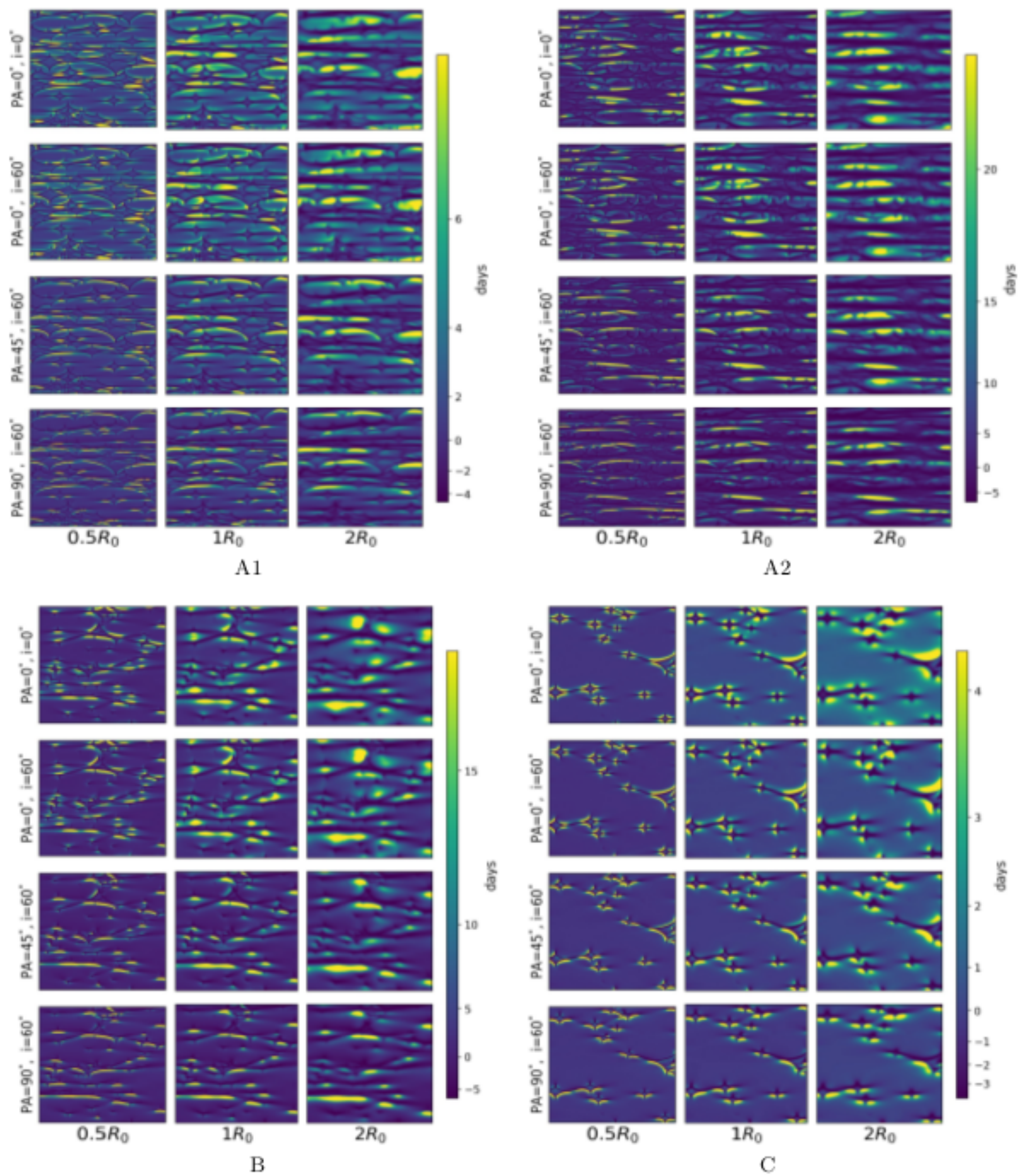

Figure 4.35: Time delay maps for PG1115+080. For each image the top row is the face-on disk, and the other 3 rows are the $i = 60°$, $PA = 0°$, $i = 60°$, $PA = 45°$, $i = 60°$, $PA = 90°$, cases. Each column shows a different size since left to right: $0.5\mathrm{R}_0$, $1.0\mathrm{R}_0$, $2.0\mathrm{R}_0$.

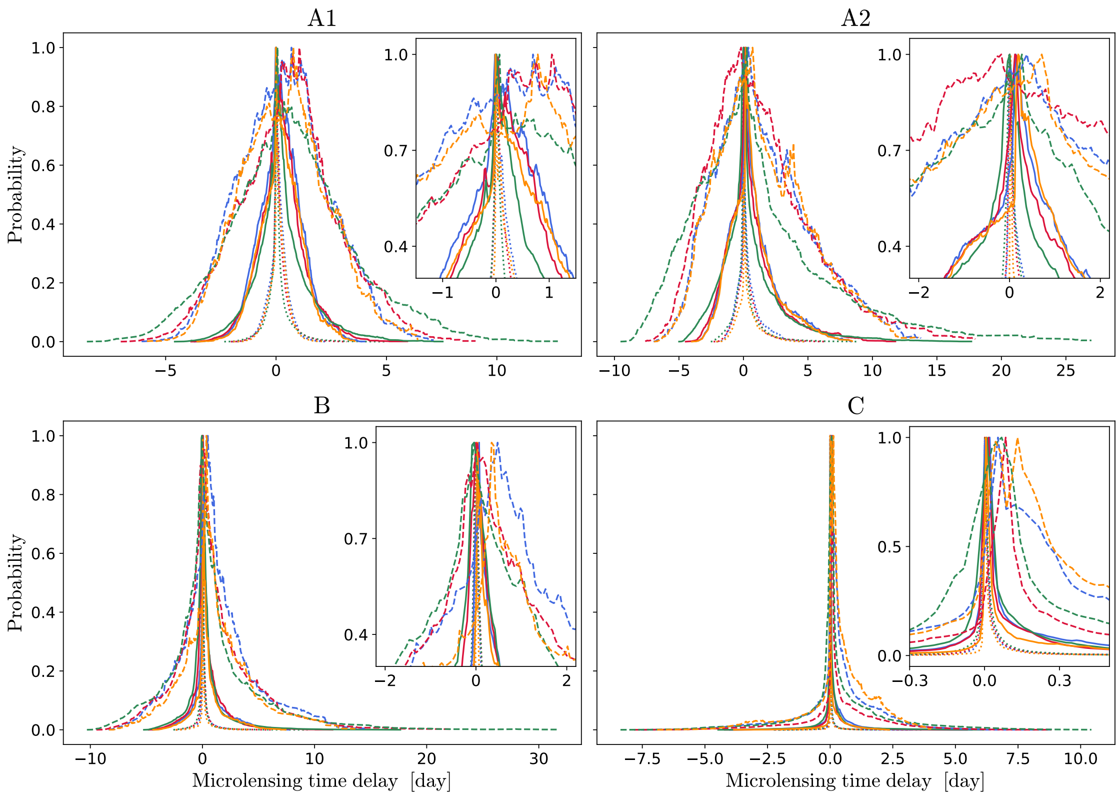

Figure 4.36: Distribution of microlensing time delay, taken from Bonvin et al. (2018). Each color represents an angle configuration case: $i = 0°$, $PA = 0°$ (yellow), $i = 60°$, $PA = 0°$ (blue), $i = 60°$, $PA = 45°$ (red), $i = 60°$, $PA = 90°$ (green). The different line styles represent the size for the accretion disk: $0.5R_0$ (dotted), R_0 (solid), $2R_0$ (dashed).

Table 4.15: 16th, 50th, 84th percentiles from the microlensing time delay distribution of each image and the difference for image pairs for PG1115+080

R_0	i	PA	A1	A2	A	B	C	AB	AC	BC
0.5	0	0	$0.09^{+0.36}_{-0.35}$	$0.12^{+0.92}_{-0.47}$	$0.14^{+0.49}_{-0.34}$	$0.05^{+0.39}_{-0.08}$	$0.01^{+0.11}_{-0.01}$	$-0.07^{+0.55}_{-0.59}$	$-0.13^{+0.40}_{-0.54}$	$-0.04^{+0.25}_{-0.46}$
0.5	60	0	$0.08^{+0.38}_{-0.34}$	$0.13^{+0.93}_{-0.49}$	$0.14^{+0.51}_{-0.34}$	$0.04^{+0.38}_{-0.09}$	$0.00^{+0.12}_{-0.01}$	$-0.07^{+0.55}_{-0.62}$	$-0.13^{+0.41}_{-0.56}$	$-0.04^{+0.25}_{-0.46}$
0.5	60	45	$0.07^{+0.38}_{-0.33}$	$0.09^{+0.85}_{-0.47}$	$0.11^{+0.50}_{-0.33}$	$0.03^{+0.31}_{-0.12}$	$0.00^{+0.10}_{-0.02}$	$-0.08^{+0.53}_{-0.60}$	$-0.11^{+0.40}_{-0.55}$	$-0.03^{+0.24}_{-0.38}$
0.5	60	90	$0.02^{+0.44}_{-0.31}$	$0.03^{+0.82}_{-0.52}$	$0.06^{+0.54}_{-0.37}$	$0.02^{+0.24}_{-0.19}$	$0.00^{+0.09}_{-0.04}$	$-0.05^{+0.56}_{-0.67}$	$-0.05^{+0.45}_{-0.60}$	$-0.01^{+0.29}_{-0.33}$
1.0	0	0	$0.22^{+0.90}_{-0.90}$	$0.41^{+1.94}_{-1.39}$	$0.36^{+1.06}_{-0.85}$	$0.24^{+1.35}_{-0.62}$	$0.04^{+0.51}_{-0.09}$	$-0.05^{+1.54}_{-1.49}$	$-0.27^{+1.00}_{-1.24}$	$-0.17^{+0.96}_{-1.54}$
1.0	60	0	$0.21^{+0.92}_{-0.93}$	$0.38^{+2.02}_{-1.38}$	$0.34^{+1.12}_{-0.85}$	$0.21^{+1.44}_{-0.63}$	$0.04^{+0.46}_{-0.14}$	$-0.03^{+1.60}_{-1.53}$	$-0.26^{+1.04}_{-1.27}$	$-0.17^{+0.97}_{-1.58}$
1.0	60	45	$0.22^{+0.96}_{-0.90}$	$0.28^{+2.09}_{-1.37}$	$0.30^{+1.19}_{-0.88}$	$0.13^{+1.28}_{-0.56}$	$0.03^{+0.43}_{-0.14}$	$-0.11^{+1.52}_{-1.59}$	$-0.26^{+1.08}_{-1.34}$	$-0.10^{+0.99}_{-1.44}$
1.0	60	90	$0.13^{+1.19}_{-0.92}$	$0.09^{+2.36}_{-1.54}$	$0.19^{+1.45}_{-0.98}$	$0.05^{+1.10}_{-0.69}$	$0.03^{+0.38}_{-0.17}$	$-0.12^{+1.64}_{-1.86}$	$-0.14^{+1.23}_{-1.58}$	$-0.02^{+1.12}_{-1.31}$
2.0	0	0	$0.42^{+2.04}_{-2.02}$	$0.99^{+4.28}_{-3.00}$	$0.82^{+2.29}_{-1.85}$	$0.83^{+3.17}_{-2.25}$	$0.26^{+1.21}_{-0.75}$	$0.10^{+3.63}_{-3.43}$	$-0.53^{+2.24}_{-2.66}$	$-0.57^{+2.68}_{-3.56}$
2.0	60	0	$0.38^{+2.09}_{-2.04}$	$1.00^{+4.40}_{-3.03}$	$0.80^{+2.34}_{-1.86}$	$0.80^{+3.35}_{-2.34}$	$0.22^{+1.25}_{-0.82}$	$0.07^{+3.76}_{-3.52}$	$-0.59^{+2.29}_{-2.73}$	$-0.62^{+2.87}_{-3.75}$
2.0	60	45	$0.60^{+2.16}_{-2.22}$	$0.74^{+4.57}_{-3.18}$	$0.76^{+2.49}_{-1.98}$	$0.53^{+3.69}_{-2.23}$	$0.15^{+1.50}_{-0.67}$	$-0.09^{+3.96}_{-3.68}$	$-0.44^{+2.47}_{-2.93}$	$-0.29^{+2.90}_{-3.96}$
2.0	60	90	$0.58^{+2.74}_{-2.48}$	$0.20^{+5.93}_{-3.73}$	$0.57^{+3.22}_{-2.36}$	$0.21^{+3.95}_{-2.44}$	$0.11^{+1.58}_{-0.72}$	$-0.30^{+4.43}_{-4.50}$	$-0.34^{+2.96}_{-3.68}$	$-0.03^{+3.43}_{-4.16}$

4.2.5 Conclusions

COSMOGRAIL monitors lensed quasars using the 2.2m telescope to obtain accurate estimations of the time delay between images. The final goal is to provide a new and precise value for the Hubble constant with an alternative technique to those employed so far (i.e, CMB, SNIa, BAO, etc.).

Until now, we estimated the time delay for two quadruple systems: DESJ0408-5354 $\Delta t(AD) = -155.5 \pm 12.8$ days (8.2%), and $\Delta t(BD) = -42.4 \pm 17.6$ days (41%) (Courbin et al. 2018), and PG1115+080 $\Delta t(AB) = 8.3^{+1.5}_{-1.6}$ days (1.8% precision), $\Delta t(AC) = 9.9^{+1.1}_{-1.1}$ days (11.1%), and $\Delta t(BC) = 18.8^{+1.6}_{-1.6}$ days (8.5%) (Bonvin et al. 2018).

Tie & Kochanek (2018a) showed that microlensing can differently magnify the accretion disk of the quasar introducing an extra delay in the light curves. Following their method, we successfully reproduced their results for RXJ1131-1231 and HE0435-1223. We also used this method to investigate the microlensing time delay impact on the time delay estimations for PG1115+080. We found that, in the worst case, the time delay estimation will be affected by $\sim 0.6 \pm 4$ days. As the estimations relies on astrophysical assumptions that are not well studied yet (e.g. the thin disk accretion disk by Shakura & Sunyaev (1973)), in the small sample available, we decided against using it in our final time delays estimations. Thus, further analysis with a larger sample are needed to characterize the impact of microlensing time delay.

4.3 Search for new lens quasar systems

Cosmological application of quasar strong lensing are limited by the size of the sample ($\sim$100). Most of the results, presented in this thesis, will benefit from a statistical large sample.

The STRong-lensing Insights into Dark Energy Survey (STRIDES) collaboration aims to find new strong gravitational lensed quasars in the Dark Energy Survey (DES) footprints. The search have been also extended to Sloan Digital Sky Survey (SDSS), the VLT Survey Telescope ATLAS (VST-ATLAS), and GAIA. At this moment $\sim$30 new lensed quasars have been confirmed in the frame of this search. This research is developing the tools to prepare automatic searchs for those systems in the upcoming surveys (LSST, Euclid). In the next sections we present the selection methodology and the current strategy to confirm the candidates.

4.3.1 The candidate selection

Candidate selection is done by different methods to avoid false positives/negatives. The idea is that a bona fide candidate will be found with different methods, while more exotic ones might not appear in all of them. In general, the combination of quasar images and lensing galaxy place this object in a particular location in the color-magnitude diagram. Thus, most of the methods include a pre-selection based on colors to exclude galaxies and stars, and morphology to distinguish between point-like sources and extended sources.

Our group of candidates are selected using different machine learning techniques like neural networks (ANNs) and mixture models. The ANNs used as input the photometry and the multi-band morphology from the catalogues. This method produces probabilities for each object to belong to different kind of classes, then the candidates are selected with cuts from the output probabilities. The complete method is explained in Agnello et al. (2015a) and applied in Agnello et al. (2015b) and Agnello et al. (2018b). The mixture models describe the lensed quasar population and the contaminants as a superposition of K probability density functions (PDFs), then, each Gaussian profile is associated to a different class of object. By fitting the Gaussian PDFs is possible to obtain the probability associated to a particular object that belongs to each K class. The specific details of this method and the selection of classes can be found in Ostrovski et al. (2017); Williams et al. (2018); Anguita et al.

(2018).

After this initial selection, most of the techniques (Agnello et al. 2018b; Williams et al. 2018; Anguita et al. 2018) use a visual inspection to exclude obvious contaminant like galaxies, quasars with a bright host, quasar-galaxy line-of-sight alignment, isolated quasars or galaxies, and pairs of object with inconsistent colors.

As a last step, the candidates are modeled as a combination of point sources and an extended one. Based on those results, the candidates are ranked from "good candidates" to "less probable", for the individual details in this step see Agnello et al. (2015b); Ostrovski et al. (2017); Williams et al. (2018); Agnello et al. (2018b); Anguita et al. (2018).

4.3.2 Candidate confirmation

To finally confirm the candidates as gravitational lensed quasars they must have some characteristics. Ideally (see Schneider et al. 1992), those characteristics are: (1) at least 2 point-like images nearby on the sky, (2) the flux image ratios are the same in different spectral bands, (3) all the images are at the same redshift, (4) emission line fluxes and shapes should be similar in all the images, (5) a possible lens in vicinity with a redshift smaller than the images, (6) temporal correlated variations in the different images.

From an observational point of view, the conditions (2), (4), and (6) might not be satisfied due to different phenomena like microlensing, dust extinction and time delay. The conditions (1), (3), and (5) are essential and we need imaging and spectral observations to confirm them.

The high resolution campaign to confirm the candidates was done with the SOuthern Astrophysical Research telescope (SOAR). We use the SOAR Adaptive Optics Module (SAMI) instrument in z-band, where we obtain a seeing ∼0.4"-0.6". As the lensed quasar images in general have small separations ($<$ 1.0 arc-second), the high resolution is important to be able to separate the components of the quasar and confirm condition (1). The z-band have been selected because of the higher probability of detecting the lens galaxy and a possible Einstein Ring produced by the quasar host galaxy (confirming the condition (5)). In Figure 4.37 we see an example of a system observed with SOAR, where we see four components of the quasar, two lens galaxies, and a faint ring. At this moment we had 7 observing runs and I participated in 5 of them: November 30th to December 2nd, June 27th-29th, December 3rd-5th (PI. V. Motta), and June 24-26, December 6th-8th (PI. T. Treu).

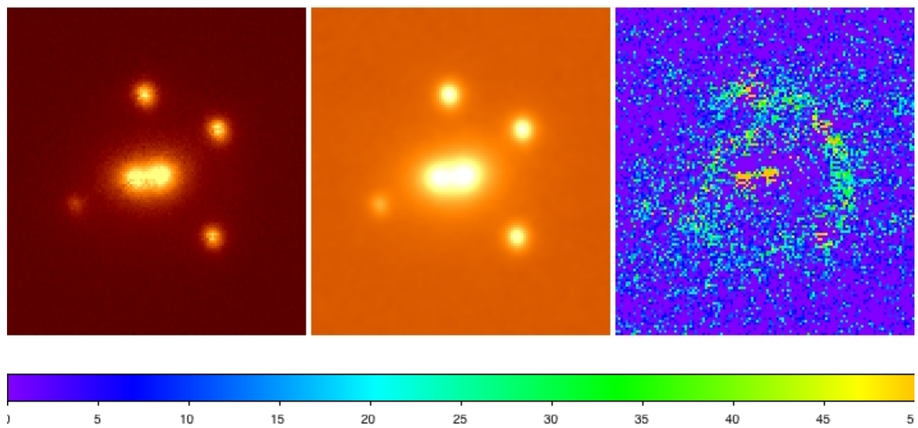

Figure 4.37: SOAR z-band images for a quasar lens system. From left to right: z-band image, model of the system, subtraction between the image and the model where we show a faint ring as a residual.

Finally, to confirm condition (3) we need spectroscopy. Spectra have been taken using EFOSC2 on NTT, La Silla telescope, confirming several systems published by Agnello et al. (2018a, 2017); Williams et al. (2018); Anguita et al. (2018)

At this moment, DES J0408-535 is the first DES system with an extensive analysis. It was discovered by Lin et al. (2017) in the DES Year 1 (Y1), consist on 4 images of the same quasar at z_s=2.375, and a central galaxy at z_l=0.597, and second foreground galaxy (G2) next to B image. Agnello et al. (2017) present a gravitational lens model made for the system, where the C component is predicted to be blended with the G2 lens galaxy. Finally, as I mentioned in section 4.2, we followed-up this system with 2.2m telescope to obtain the time delays between the images (Courbin et al. 2018).

The results of the 2016 STRIDES follow-up campaign shows that, from 117 targets observed, 7 were confirmed as lenses, 7 as nearly identical quasars (NIQs) and 27 are inconclusive. For those classified as NIQs, we need more data and analysis to understand why the lines do not match exactly at the same wavelength. One possible explanation is microlensing affecting the BLR. In the case of the inconclusive targets, we need more data to observe the lens galaxy and confirm its redshift and/or separate the components of the quasar. Thus, 2016 follow up campaign yield a success rate between 6-35%, which is a good rate taking in account that the selection

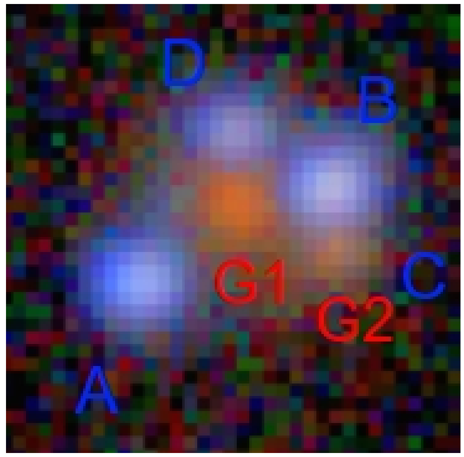

Figure 4.38: DES gri color composite image of DES0408-5354. In blue are the A, B, C and D components of the quasar, and in the red lens galaxies.

in purely photometric and there is no spectroscopic pre-selection. Finally, with the 2017 campaign, there are around 30 new gravitational lens system confirmed but we are still going through the candidate list. Several follow-up observations are being carried out (HST imaging, higher S/N spectra taken with x-shooter/VLT) to further investigate the confirmed systems.

Chapter 5

Results for the dynamical analysis in groups and clusters

In this chapter we present the results of the dynamical analysis of the galaxy groups SL2S J02140-0535, and SL2S J085207-034315, and the cluster of galaxies Abell 1703. The results for SL2S J02140-0535 were presented in Verdugo et al. (2016), and the results for Abell 1703 will be published in Motta et al. in prep.

The most massive structures in our Universe that are gravitationally bound are cluster of galaxies. These systems are located in the nodes of the cosmic web (Frenk et al. 1996; Springel et al. 2005; Jauzac et al. 2012), and can be used to probe cosmological parameters. For example, comparing the observed number density of galaxy clusters with the cosmological predictions or using the mass-to-light ratio we can estimate the dark and baryonic matter content.

The mass distribution in a galaxy can be described using a Navarro, Frenk & White profile (NFW, Navarro et al. 1996, 1997), but the distribution at larger scales (groups and cluster) have not been well studied yet. The methods to study the mass distribution, like X-ray emission, dynamics and strong lensing have their own limitations. To estimate the mass distribution with X-rays and dynamics we must assume that the systems are in a virial state, something that is generally not true. Strong lensing is free of this assumption, but it is limited to a small projected radii (inside the Einstein ring radius, where the arcs are formed) and only can constrain the two-dimensional projected mass density. To overcome the limitations of each technique in the mass distribution measurements, we presented in Verdugo et al.

(2016) a method that combine the dynamics of the galaxy members with strong lensing modeling.

In this work we present confirmed members and the estimation of velocity dispersion for 2 groups of galaxies (SL2S J02140-0535 and SL2S J08521-0343), and for the cluster of galaxies Abell 1703. In the case of SL2S J02140-0535 the combined analysis to measure the mass distribution is already published in Verdugo et al. (2016). For the other systems further analysis are needed to publish the results.

5.1 Observations and data reduction

The Strong Lensing Legacy Survey[1] (SL2S) used the Canada France Hawaii Telescope Legacy Survey[2] (CFHTLS) to search for new strong lensing systems. The first compilation of lens candidates at the scale of groups of galaxies is shown in More et al. (2012). Group of galaxies are the most common structures in the Universe, cover an intermediate range of masses, between galaxies and clusters, but there is no clear boundary (Tully 2015). Thus, it is assumed that the common range of masses for a group is between $\sim 10^{13}$ $M_{\odot}$ - $\sim 10^{14}$ $M_{\odot}$. This compilation was made searching for gravitational arcs in the survey giving the name to the sample SL2S-ARCS (SARCS).

To obtain the member candidates we created a photometric redshift catalog using the T0005 release of CFHTLS, (November 2008), we include the galaxies within ± 0.01 of the redshift of the main lens galaxy. The color of the galaxies in the catalog are $(g\text{-}i)_{lens}$ -0.15 < g-i < $(g\text{-}i)_{lens}$ + 0.15 (i.e. the red sequence), where $(g\text{-}i)_{lens}$ is the color of the brighter galaxy within the Einstein radius.

We obtained spectra using the spectrograph FORS2 at VLT, Paranal Observatory, for SL2S J02140-0535, and SL2S J08521-0343 (PI V. Motta 086.A-0412). We used the GRISM 300I and exposure time of 2×1300 seconds for each mask. The data were taken on December of 2012.

The masks were reduced using the ESO Recipe Execution Tool (EsoRex), the Common Pipeline Library (CPL), and the Optimal Spectrum Extraction Package (OSEP) in IDL.

In the case of Abell 1703 we selected as targets the brightest objects with SDSS

[1]http://www-sl2s.iap.fr/
[2]http://www.cfht.hawaii.edu/Science/CFHLS/

colors roughly along the red sequence. We used DOLORES/TNG spectra at La Palma Observatory (PI F. Gastaldello). Five multi-slits masks were designed, each of them with 20 slits. The dates of observation of each mask are: 2010-10-28 (M1), 2010-05-16 (M2), 2010-11-26 (M3), 2011-01-03 (M4), and 2011-01-09 (M5). The total integration time for each mask was 1800 seconds. The data reduction follow the standard procedures and include bias subtraction, flat correction, wavelength calibration, and spectra extraction.

5.2 Method

5.2.1 Redshift measurements

To obtain the redshift of each observed galaxy we used the Radial Velocity Package for IRAF (RVSAO, Kurtz & Mink 1998). The package use template spectra of galaxies with known velocity dispersions and cross-correlate them to our spectra using features like the emission and absorption lines. The velocity dispersion and its error is provided in km s^{-1}, which is related to the redshift as $z = V_{disp}/c$, where c=300000 km s^{-1}, is the speed of light. The reliability of the results are given by the R value, which depends on the amplitude of the cross correlation peak. The result with the higher R value is the best one.

We classify the redshift estimation quality in three categories: "secure" for those with more than 2 absorption/emission lines detected (Figure 5.1), "questionable" for those with two or less absorption/emission lines, and "unknown" for those with no identified features.

5.2.2 Member selection and velocity dispersion

To select the members we adopted the formalism described in Wilman et al. (2005). We initially assumed that the cluster is located at the redshift of the main lens galaxy (z$_l$), which is the cD galaxy in case of clusters. The initial observed-frame velocity dispersion is given by:

$$\sigma(v)_{obs} = V_i(1 + z_l) \quad km \quad s^{-1}, \tag{5.1}$$

where V$_i$ is the initial velocity dispersion, which is initially set at 500 km s^{-1} for

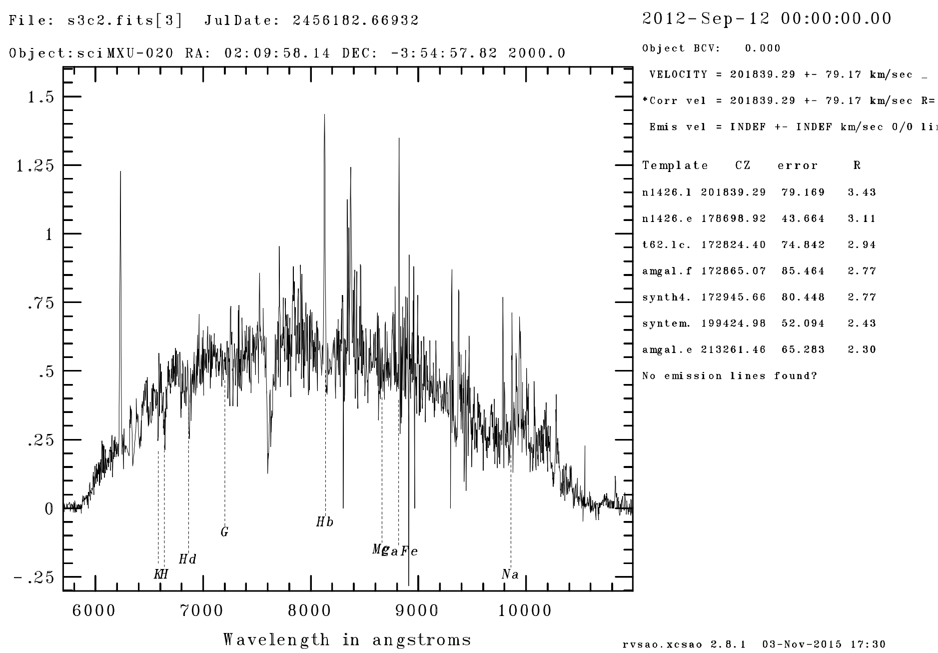

Figure 5.1: Galaxy spectrum fitted using RVSAO where H K, and Hd absorption lines, and OII emission lines are visible. We see the template list with their corresponding velocity dispersion, error and the R value.

groups and 3000 km s^{-1} for clusters. The potential members are those galaxies enclosed in a cylinder whose size is given by the maximum redshift shell (δz_{max}), and the maximum spatial distance ($\delta\theta_{max}$). These two quantities are defined as:

$$\delta z_{max} = \frac{2\sigma(v)_{obs}}{c}, \tag{5.2}$$

$$\delta\theta_{max} = 206265" \frac{c\delta z_{max}}{b(1+z_l)H(z)D_\theta(z)}, \tag{5.3}$$

where c is the speed of light, b is the the axis ratio of the cylindrical linking volume selected as b=3.5 in this work (Muñoz et al. 2013), H(z) is the Hubble constant at z, D_θ(z) is the angular diameter distance at z. Then, we compute a new observed velocity dispersion using a biweight estimator (Beers et al. 1990), taking into account only the possible candidates. With this new $\sigma(v)_{obs}$ we calculate new sizes for the cylinder, and all the galaxies within the new limits are the confirmed members of the group or cluster. Using the redshifts of the final members, and the biweight estimator, we re-calculate the redshift and we obtain the line of sight velocity dispersion

($\sigma(v)_{los}$) for the lens.

To compute the confidence interval in the estimation of $\sigma(v)_{los}$ we used the statistic test bootstrap (Efron 1979) that relies on random sampling with replacement. We used the Python package astroML (Vanderplas et al. 2012; Ivezić et al. 2014) and we bootstrapped our sample 10000 times.

5.2.3 NFW mass density profile

As was described in section 2.5.2 NFW profile describe the mass density profile through the characteristic density (ρ_s) and the scale radius (r_s). The virial radius r_{200} is defined as the radius of a spherical volume inside of which the mean density is 200 times the critical density (ρ_{crit}) at the given redshift z, then:

$$M_{200} = 200 \times (4\pi/3) r_{200}^3 \rho_{crit} = 100 H^2 r_{200}^3 / G. \tag{5.4}$$

The scale radius is related to the the virial radius (r_{200}) through the concentration: $c_{200} = r_{200}/r_s$. It has been found that the 3D concentration for strong lensing clusters is ∼18% higher than the one for typical clusters with similar masses (Hennawi et al. 2007; Limousin et al. 2013), although it is still not clear if the strong lensing clusters are more elongated or are just more concentrated thus being more likely to produce strong lensing arcs.

The mass within a radius r, considering a NFW mass density profile for the halo, is:

$$M(r) = 4\pi r_s^3 \rho_s \left[ln(1 + r/r_s) - \frac{r/r_s}{1 + r/r_s} \right]. \tag{5.5}$$

In this work we made the dynamical model with the code Modelling Anisotropy and Mass Profiles of Observed Spherical Systems (MAMPOSSt, Mamon et al. 2013). This code performs a maximum likelihood fit of the distribution of galaxies in the projected phase space (projected radii and LOS velocity). The strong lensing model was made using LENSTOOL[3] (Jullo et al. 2007). This software use a Bayesian Monte Carlo Markov Chain (MCMC) method to obtain the most likely model parameters. To combine the strong lensing and dynamical constraints we incorporate the MAMPOSSt likelihood routine into LENSTOOL.

[3]LENSTOOL software is publicly available at *https://projets.lam.fr/projects/lenstool/wiki*

5.3 Dynamical analysis for SL2S groups of galaxies.

The groups analyzed in this work come from SARCS sample (see Section 5.1) and are now confirmed groups of galaxies.

5.3.1 SL2S J02140-0535 results

This group is located at z_{spec}= 0.44 was reported by Cabanac et al. (2007). It shows three arcs surrounding three galaxies (Figure 5.2), where G1 is the brightest galaxy. The arc A is composed by two merging images, the arc B is associated with A and the arc C is a single image. The arcs A and B are at z_{spec}=1.017 ± 0.001 and C at z_{spec}=1.628 ± 0.001 (Verdugo et al. 2016).

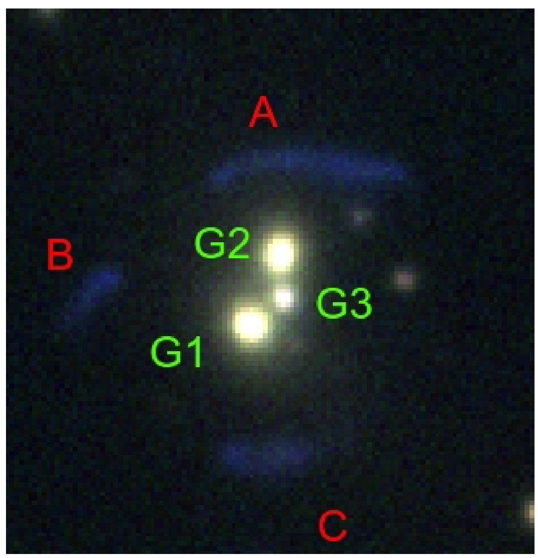

Figure 5.2: SL2S J02140-0535 CFHTLS false color image. The zoom of 23”×23” show the arcs and central galaxies. A, B and C are the arcs and G1, G2, and G3 are the three galaxies within the arcs.

Alard (2009) studied the group using strong lensing, Limousin et al. (2009) using strong and weak lensing and Muñoz et al. (2013) made a dynamical analysis. From the dynamical analysis, 16 galaxies where confirmed as members of the group with a line-of-sight velocity dispersion of $\sigma(v)_{los} = 364^{+60}_{-137}$.

We observed a total of 42 new spectra, where 11 were categorized as “secure”. We join this new sample with the confirmed candidates by Muñoz et al. (2013) to

Table 5.1: Galaxies members of the group SL2S J02140-0535.

RA [deg]	DEC [deg]	z
33.550777	-5.551144	0.4438 ± 0.0001
33.536942	-5.582868	0.4430 ± 0.0002
33.533779	-5.592632	0.4446 ± 0.0002
33.53043	-5.594814	0.4474 ± 0.0002
33.519188	-5.601521	0.4459 ± 0.0002
33.515137	-5.577593	0.4442 ± 0.0001
33.512367	-5.573329	0.4440 ± 0.0001
33.500538	-5.558484	0.4459 ± 0.0002
33.484375	-5.623324	0.4436 ± 0.0002
33.479259	-5.613928	0.4435 ± 0.0002
33.546135	-5.607511	0.4436 ± 0.0001
33.540424	-5.584474	0.4427 ± 0.0001
33.512676	-5.596797	0.4473 ± 0.0002
33.548912	-5.61646	0.4426 ± 0.0003
33.533501	-5.59193	0.4446 ± 0.0002
33.527908	-5.597961	0.4443 ± 0.0002
33.543442	-5.557844	0.4424 ± 0.0001
33.555248	-5.621617	0.4471 ± 0.0003
33.563099	-5.561144	0.4465 ± 0.0001
33.475819	-5.62775	0.4438 ± 0.0002
33.510559	-5.596503	0.4442 ± 0.0001
33.514061	-5.595108	0.4455 ± 0.0002
33.51992	-5.569031	0.4449 ± 0.0002
33.521729	-5.574636	0.4462 ± 0.0002

do the dynamical analysis. We obtained 24 secure members and $\sigma(v)_{los} = 562 \pm 60$ km s^{-1}, in good agreement with Muñoz et al. (2013) results. All the members are shown in Figure 5.3 and their redshifts are in Table 5.1.

In Verdugo et al. (2016) we showed this dynamical analysis, together with a new strong lensing model to investigate the mass density profile of the group using a NFW profile (see in 5.2.3). From the dynamical analysis we obtained a scale radius r_s=184^{+209}_{-60} kpc and from strong lensing r_s=199^{+135}_{-91} kpc. The concentration c_{200} was unconstrained. Doing a combined dynamics + strong lensing analysis it was possible constraint both parameters: r_s=82^{+44}_{-17} kpc and $c_{200} = 10.0^{+1.7}_{-2.5}$. Then, the combined analysis reduced the errors and yield a better constraint of the model, being also in

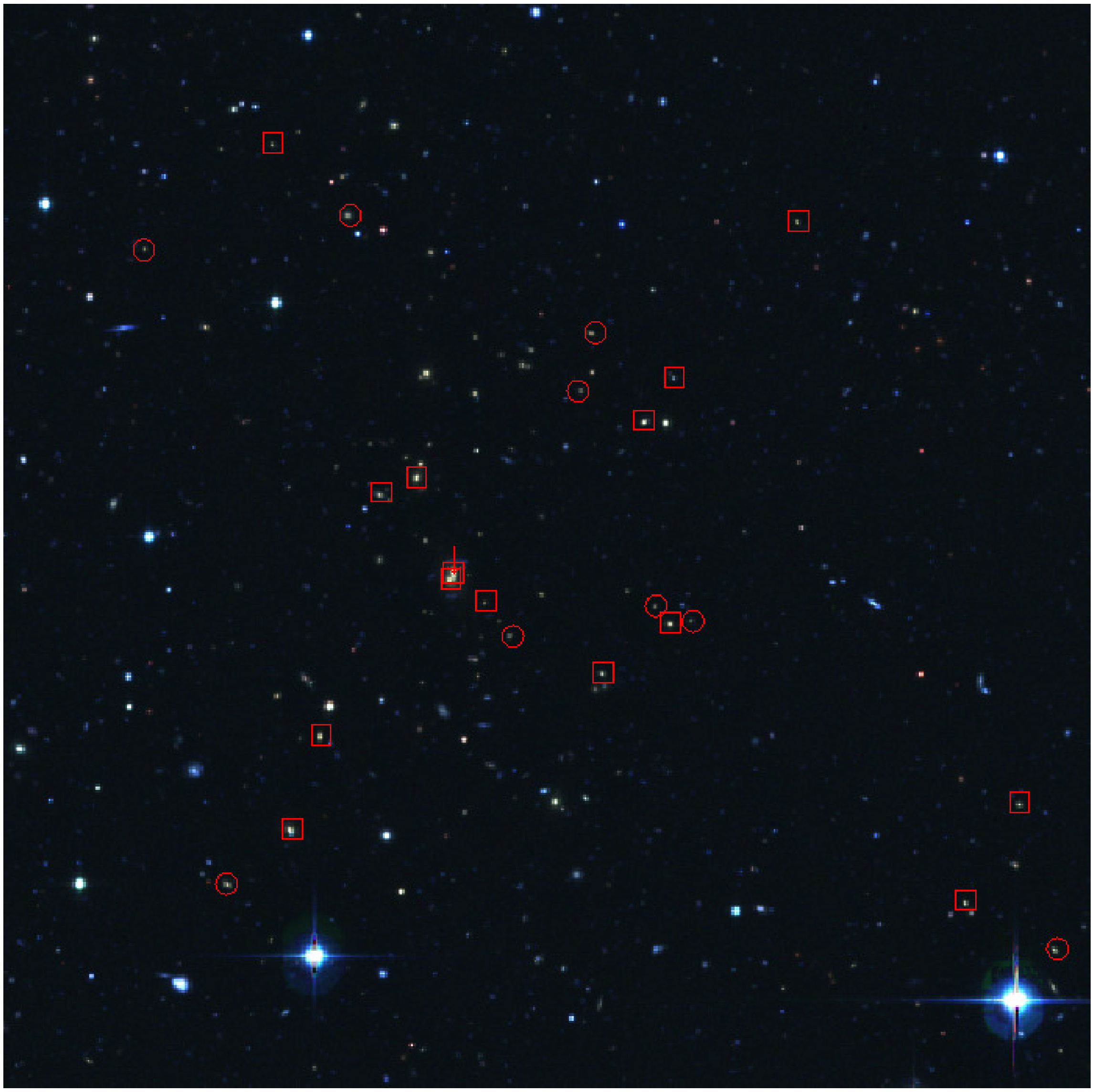

Figure 5.3: CFHTLS false color image for SL2S J02140-0535. The red squares and circles show the location of the 24 confirmed members of the group, the squares are the galaxies reported by Muñoz et al. (2013), and the circles are the new observed galaxies. The size of the field is $7' \times 6'$.

good agreement with previous studies using weak lensing (Verdugo et al. 2011; Foëx et al. 2013; Lieu et al. 2016).

The main result is summarized in Figure 5.4 that show the comparison between the combined analysis with the results obtained from previous studies. Up to ∼1Mpc the combined models overlap with Verdugo et al. (2011), this is consistent with the small number of galaxies at radii larger than 1Mpc. Then, dynamical constraints at larger scale are not strong. On the other hand weak lensing can be over estimated because assumed a singular isothermal sphere to calculate the mass. The estimation of masses using Foëx et al. (2013) work at 1Mpc and 0.5Mpc are also showed in the plot and agree with the mentioned measurements. As a comparison, we also used the estimation from Lieu et al. (2016) but, as the work derived a cluster concentration lower from the mass-concentration relation derived from N-body, there are discrepancies in the results. This is solved by doing our own fit to their data, considering $c_{200} = 10$.

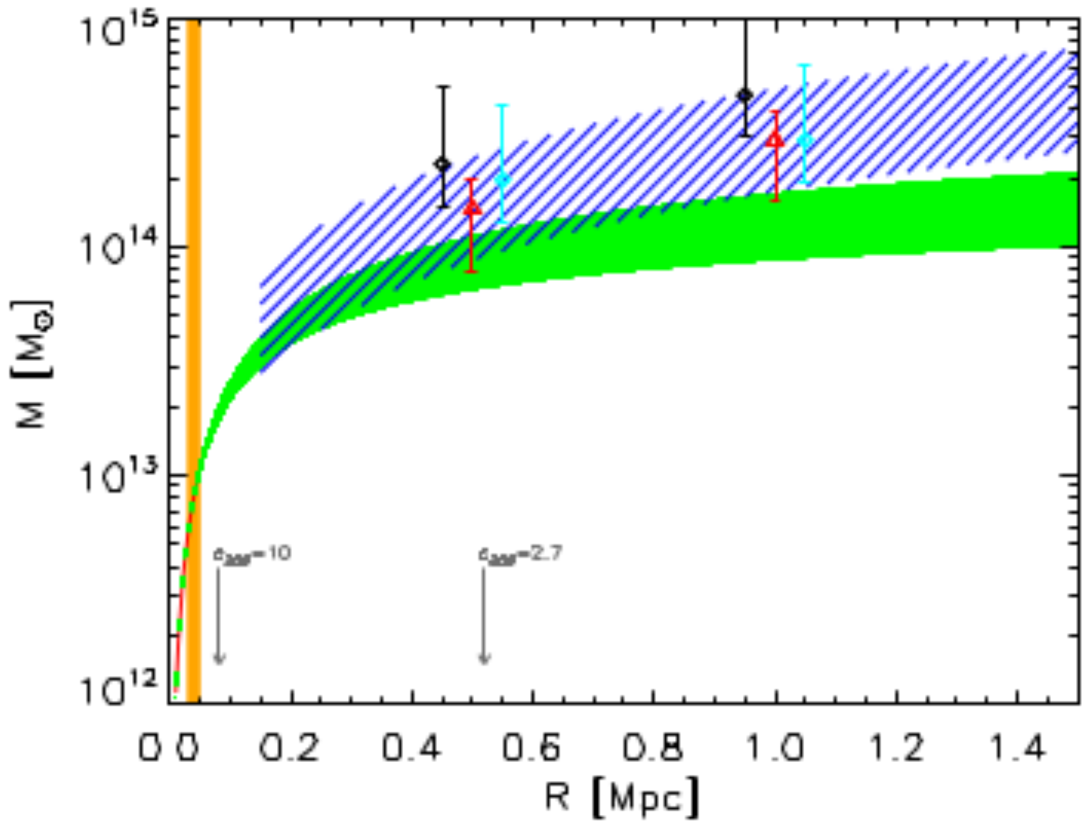

Figure 5.4: Projected mass (2D) as a function of the radius, taken from Verdugo et al. (2016). The green area is the mass profile within 1σ error for the strong lensing + dynamics model. The dashed blue area is the mass profile within 1σ error for the weak lensing model by Verdugo et al. (2011). The orange area is the region where the arcs lie. The red triangles are the weak lensing estimation presented by Foëx et al. (2013). The black diamonds, shifted -0.05 in R, show the prediction by Lieu et al. (2016). Cyan diamonds, shifted +0.05 in R, are the estimation by Lieu et al. (2016) considering c_{200}=10.

5.3.2 SL2S J08521-0343 results

This group is located at z_{phot}=0.48 (More et al. 2012). It is composed by two galaxies with two lensed arcs (Figure 5.5). The redshift of the arcs is still not known because their spectra do not show any clear feature like absorption or emission lines (Verdugo et al. 2014).

Foëx et al. (2013) show a weak lensing and optical analysis for the best SARCS candidates. For SL2S J08521-0343 they estimated $\sigma_{SIS} = 561^{+116}_{-155}$ km s^{-1} derived from the shear profile, $R_E = 5.2^{+3.6}_{-3.3}$ arc-seconds from σ_{SIS}, and luminosity derived from the bright red galaxies of $L = 0.84 \pm 0.08 \times 10^{12}$ $L_\odot$ using and aperture of 0.5 Mpc and $L = 1.51 \pm 0.16 \times 10^{12}$ $L_\odot$ using and aperture of 1 Mpc. Verdugo et al. (2014) presented a SIE model for the group using LENSTOOL code (Kneib 1993; Jullo et al. 2007) using HST data. It is not clear if both arcs belong to the same source, then in the model they assumed that the arcs are different systems and the arc A is used to perform the optimization. The best fitted parameters are $\epsilon = 0.30 \pm 0.03$ (ellipticity), $\theta = 157.0 \pm 0.6$ degrees (ellipticity position angle), and $R_E = 5.2 \pm 0.1$ arc-seconds in agreement with Foëx et al. (2013).

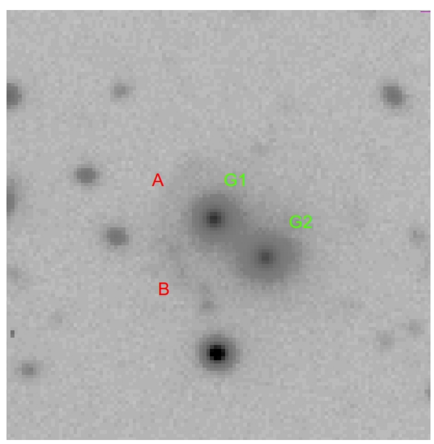

Figure 5.5: SL2S J08521-0343 VLT G-band image with a zoom of 32"×32". The arcs are label as A and B and the central galaxies are G1 and G2.

We observed a total of 66 galaxy spectra where 33 where categorized as "secure". Applying the method described in subsection 5.2.2, we obtain a total of 10 members and $\sigma(v)_{los} = 601^{+38}_{-94}$ km s^{-1}, in good agreement with Foëx et al. (2013), and a mean redshift between the members of $z_{mean} = 0.44$, which is not in agreement with the photometric redshift (z_{phot}=0.48) reported in More et al. (2012). The list of the galaxy members and the spatial distribution are in Table 5.2 and Figure 5.6, respectively.

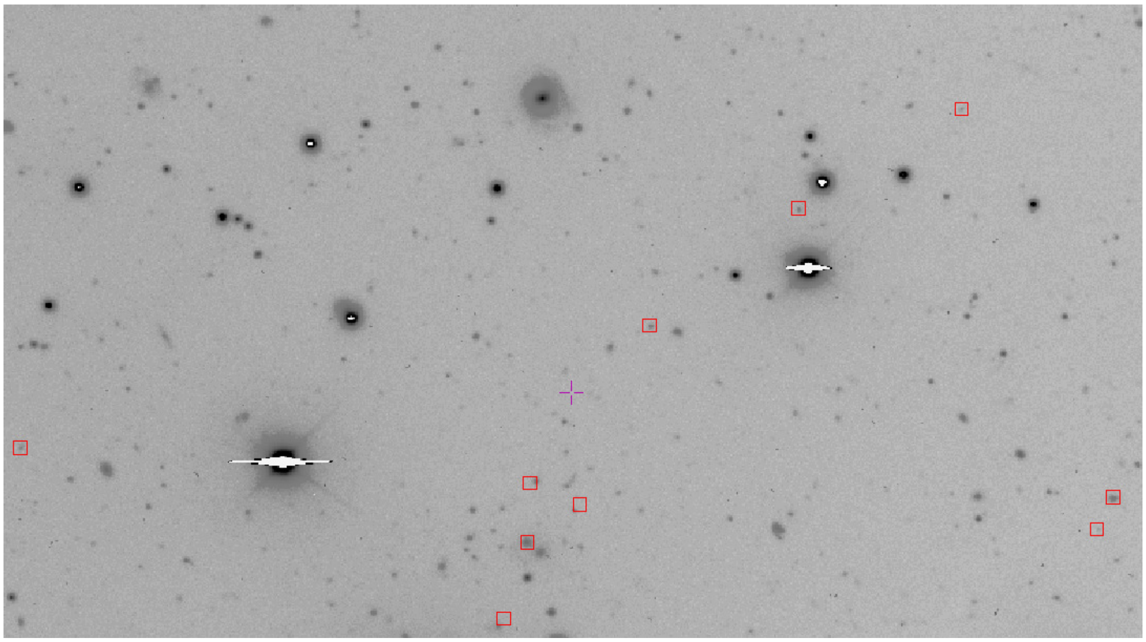

Figure 5.6: VLT g-band image for SL2S J08521-0343. The red squares mark the galaxies member of the group. The field have a size of $6' \times 3'$.

Table 5.2: Galaxies members of the group SL2S J08521-0343.

RA [deg]	DEC [deg]	z
133.0214	-3.705386	0.4451 ± 0.0001
133.0265	-3.718297	0.4401 ± 0.0001
133.0300	-3.716725	0.4397 ± 0.0003
133.0303	-3.720942	0.4380 ± 0.0002
133.0669	-3.714097	0.4373 ± 0.0002
133.0107	-3.697000	0.4412 ± 0.0002
132.9989	-3.689819	0.4438 ± 0.0001
133.0320	-3.726447	0.4402 ± 0.0003
132.9891	-3.720075	0.4458 ± 0.0002
132.9880	-3.717825	0.4417 ± 0.0002

5.4 Abell 1703 results

Abell 1703 is one of the richest clusters discovered by Abell (1958) at redshift z=0.28. It shows a dominant central giant elliptical galaxy and strong gravitational lensing features (Figure 5.7). Limousin et al. (2008) identified 13 strong image systems. Richard et al. (2009) updated the model with 16 multiple systems and fitted a generalize NFW profile obtaining a best fit with a logarithmic slope of $\alpha = 0.92 \pm 0.04$, concentration $c_{200} = 4.7 \pm 0.4$ and scale radius $r_s = 476 \pm 45$ kpc.

Bayliss et al. (2013) showed a dynamical analysis of 16 cluster including Abell 1703. Using the MMT telescope they observed 182 galaxies candidates in 2012. To obtain the candidates, first they selected their targets from the spectroscopic catalog using a by-eye-guess of the cluster redshift, then they computed an initial estimate using the bi-weight location and scale of the velocity distribution for all redshifts within +-0.02, and within a projected physical radius $<$ 1.5 Mpc. They found 42 members, estimated the cluster redshift z = 0.277 and a velocity dispersion $\sigma(v)_{los}$ = 1380 km s^{-1}. All Bayliss et al. (2013) members are shown with red circles in Figure 5.8.

We observed a total of 98 galaxies candidates for the cluster with Telescopio Nazionale Galileo (TNG). We join our candidates with the complete sample of 182 galaxies of Bayliss et al. (2013). First, we applied a spatial cut of 9.5 arc-minutes ($\sim$3Mpc) taking the cD galaxy as center. Then we selected the members of the cluster as was described in the method section. We obtained 95 galaxies as confirmed members of the cluster, the cluster redshift z=0.275, and the velocity dispersion $\sigma(v)_{los} = 1261 \pm 60$ km s^{-1}. These values are in agreement with those found by Bayliss et al. (2013).

The joint analysis (dynamics and strong lensing) for this cluster is being carried out (Verdugo et al. in prep.).

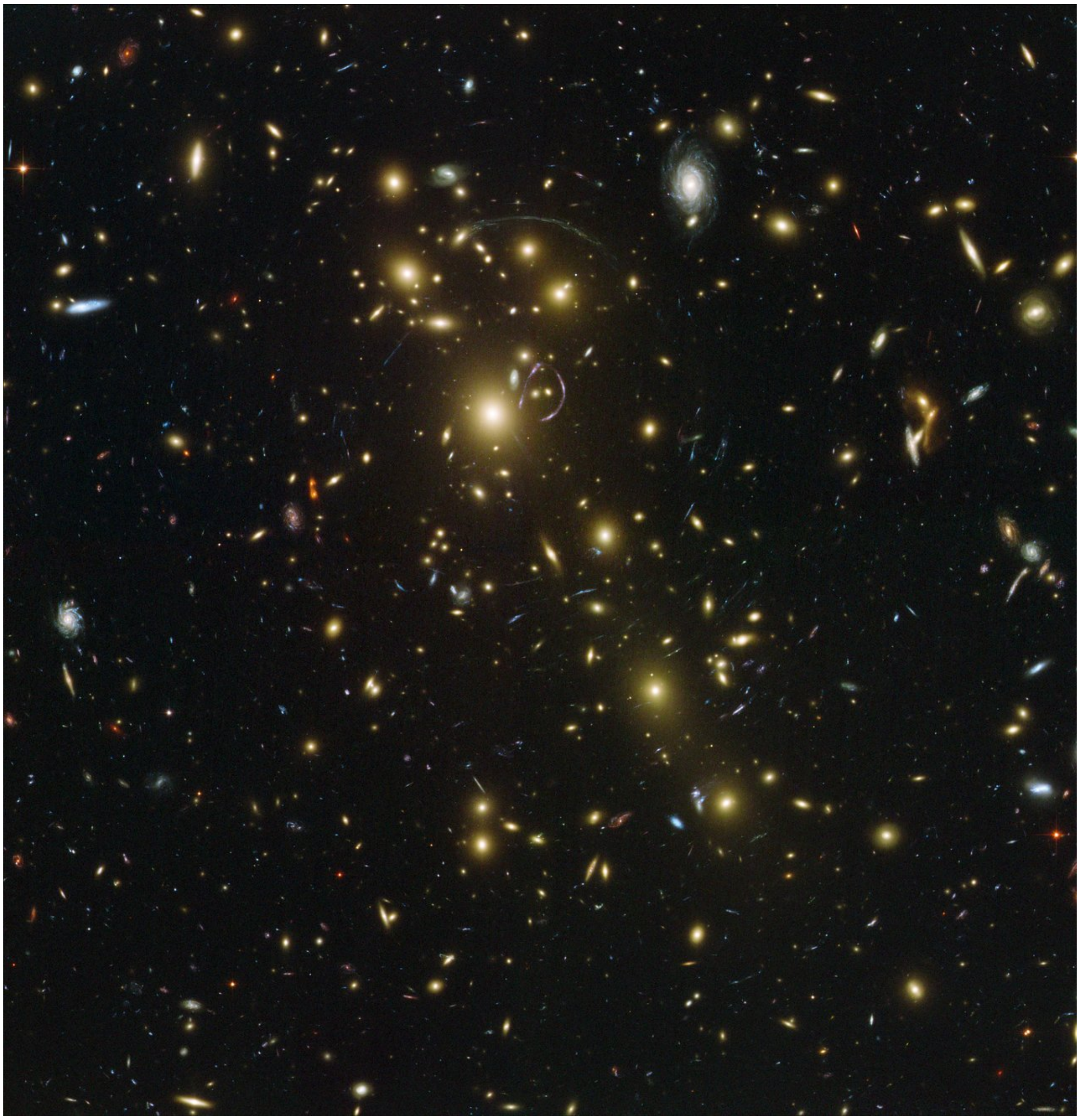

Figure 5.7: HST false color image of Abell 1703. This image was taken from HST website[5]. We see several blue arcs. The size of the image is $3.5' \times 3.5'$.

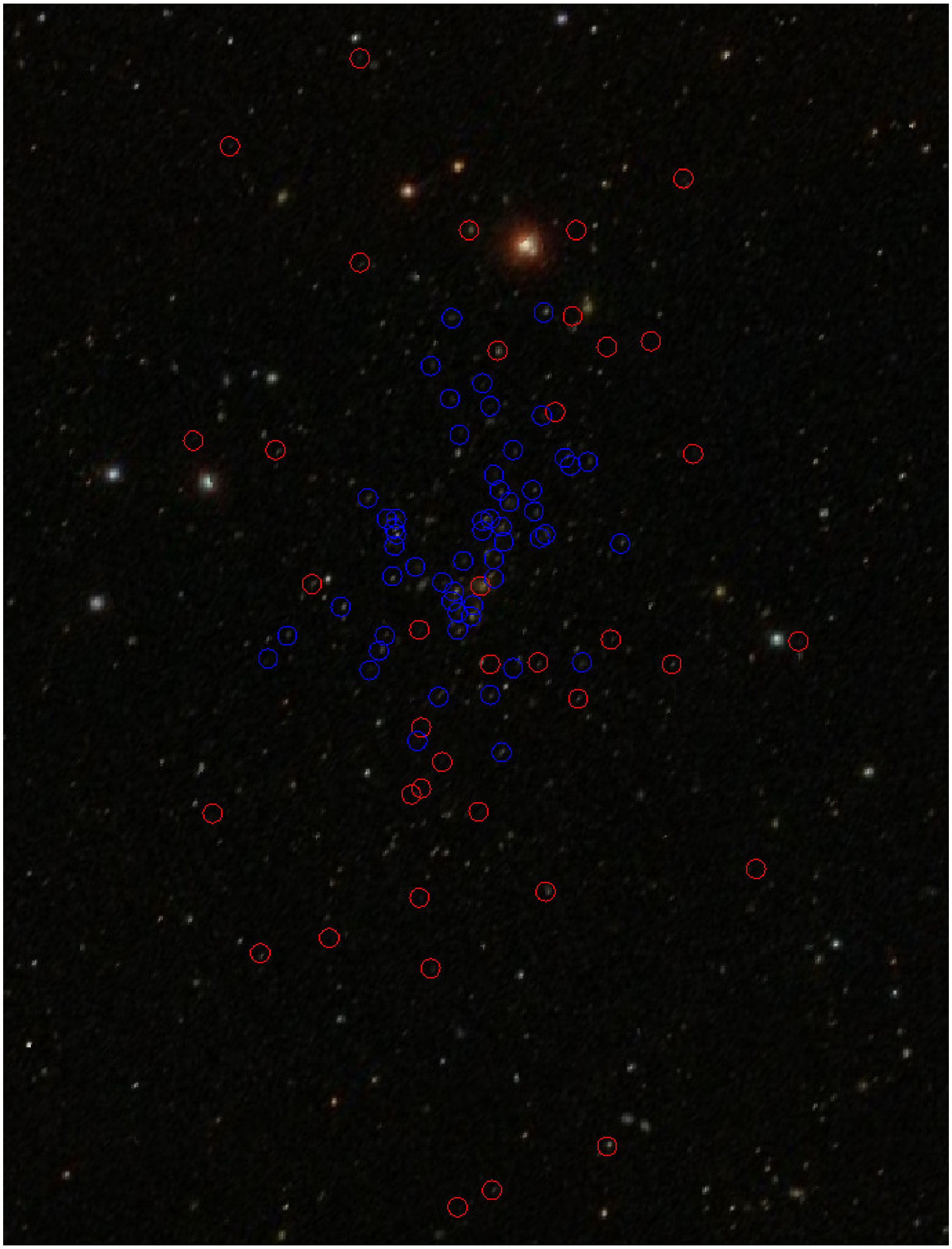

Figure 5.8: SDSS false color image for the cluster Abell 1703. In red circles are the members confirmed by Bayliss et al. (2013) and in blue circles are the members confirmed by this work. The size of the field is $13' \times 18'$

5.5 Conclusions

We analyzed spectroscopic data to confirm new members for the group of galaxies SL2S J02140-0535 and SL2S J085207-034315, and for the galaxy cluster Abell 1703.

SL2S J02140-0535 was previously analyzed by Muñoz et al. (2013). Using our new spectra, we increased the number of confirmed members to a total of 24, and estimated $\sigma(v)_{los}$ = 562 ± 60 km s^{-1}. Verdugo et al. (2016) used these results to present the first combined analysis using dynamics and strong lensing to study the mass distribution profile in groups and clusters. The combined analysis gets a better constraint on the NFW parameters, obtaining a scale radius $r_s = 83^{+44}_{-17}$ kpc and a concentration $c_{200} = 10.0^{+1.7}_{-2.5}$.

In the case of SL2S J085207-034315 the FORS2/VLT data are the first attempt to confirm members and obtain the redshift of the arcs. We confirm 10 members, $\sigma(v)_{los} = 601^{+38}_{-94}$ km s^{-1}, and confirm the redshift of the lens at z=0.44.

Abell 1703 is a cluster located at z=0.28. A first dynamical analysis was made by Bayliss et al. (2013). We obtained 98 new spectra and confirmed 53 member galaxies more, having now a total of 95 members. We estimate a velocity dispersion $\sigma(v)_{los}$ = 1380± km s^{-1} and the redshift is z=0.275.

For SL2S J085207-034315 and Abell 1703 we plan to extend the combined analysis using dynamics and strong lensing to study the mass distribution profile of this systems as we already did for SL2S J02140-0535. In the case of SL2S J085207-034315 further analysis are needed, for example to confirm the redshift of the arcs. For Abell 1703 the analysis are already on its way and will be presented in Verdugo et al. in prep.

Chapter 6

Conclusions

In this PhD thesis I studied different structures that are affected or produced by gravitational lens effect:

(1) I analyzed galactic microlensing light curves from the VISTA Variables in the Vía Láctea survey (VVV). In Section 3.1 we presented the results published in Minniti et al. (2015), where we showed the first microlensing event detected in the survey. This microlensing event was detected in the field of the globular cluster NGC 6553. I fitted the event using a simple single-lens model with and without blending. The CMD suggests that the source star is located in the bulge at a distance D_s=8–9 kpc. To estimate the mass we assumed that the lens is a member of NGC 6553 at a distance of D_l=6 kpc, giving a lens mass M=1.5–3.5 $M_\odot$, which corresponds to a heavy remnant as a black hole.

In Section 3.2 we presented the results of a search of microlensing events in the VVV tiles b309 and b296. Using the variability index η and a visual inspection we obtained 9 light curves classified in the ”secure” and ”probable” regions, where five of them were discovered by this survey. The cross-match with OGLE database provides 88 objects in tile b309 and 45 in tile b296, where only 14 were detected in our light curves. We analyzed a total of 19 light curves, 15 of them in b309 and 4 of them in b296. Using a simple single-lens model, 8 of the events yield well constrain parameters. For those events with OGLE counterparts (14), only 5 events show good agreement with the parameters estimated by OGLE at 3σ error, but only VVV-b309-m002 and VVV-b296-m002 show well constrained parameters. Most of the VVV events with OGLE counterpart show light curves that are incomplete due to the heterogeneous cadence of the survey.

We analyzed the proper motions and color-magnitude diagrams to located the source stars of the events found by our method. Combining the information of PM and CDM we found that the source stars of VVV-b309-m001, VVV-b309-m006 and VVV-b296-m003 are located in the bulge, while VVV-b309-m002 and VVV-b309-m003 are likely located in the red clump. As only VVV-b309-m002 showed well constrained parameters of the microlensing fit, we estimate a probable range of masses for the lens star. Assuming that the source is in the red clump ($D_s^{RC} = 7.8 \pm 0.06$ kpc), the lens is a disk star located between D_l = 2–6 kpc, and the transverse velocity is 220 km s^{-1}, we obtained M=0.5–0.7 $M_\odot$ (Rojas et al. submitted to the MNRAS).

The VVV survey has been designed to study variable stars, but we found a 90% of the events detected by OGLE, including 5 events discovered in this search. Fourteen percent of the total sample (19 events) present parts of the microlensing event that are well fitted by a simple single lens model. Thus, even with VVV have low and heterogeneous cadence our microlensing search is successful, and will be extended to other tiles.

(2) In Chapter 4 I presented the analysis of microlensing effect in quasars with two main objectives: to investigate the inner structure of the quasar and to explore the effect of microlensing in the estimation of time delays.

The first objective is presented in Section 4.1. I used single-epoch spectra of lensed quasars to analyze perturbations produced by microlensing, chromatic microlensing or extinction. I presented image pairs of lensed quasars: HE0047-1756 (AB), SDSS1155+6346 (AB) (Rojas et al. 2014), HE2149-2745 (AB) (Motta et al. 2017), SDSS0924+0219 (BC), Q1355-2257 (AB), and SDSS1029+2623 (BC), (Rojas et al. in prep (b)). We compared the magnitude differences of the core of the emission lines with the underlying continua to study flux anomalies.

We found dust extinction in SDSS1029+2623 spectra but not evidence of microlensing or chromaticity. We estimated a high extinction of ΔE=0.33 ± 0.08 (R_v=4.1 ± 0.4), but using R_v=3.1 we found ΔE=0.17 ± 0.01, that is in agreement with previous studies.

In the other 5 systems we found chromatic microlensing effect, therefore we estimated the size and the temperature profile of the accretion disk for each case: $r_s = 5^{+6}_{-3}$ light days, p = 2.3 ± 0.8 (λ_{rf} = 2045 Å, HE0047-1756); $r_s = 10^{+15}_{-6}$ light days, p = 1.5 ± 0.6 (λ_{rf} = 1398 Å, SDSS1155+6346); r$_s$ = 8^{+11}_{-5} light days, p = 0.5 ± 0.3 (λ_{rf} = 1310 Å, HE2149-2745); $r_s = 7^{+3}_{-2}$ light-days, $p = 0.7 \pm 0.2$ (λ_{rf} = 3533 Å, SDSS0924+0219); $r_s = 4^{+4}_{-2}$, $p = 1.1 \pm 0.5$ (λ_{rf} = 3533 Å, Q1355-2257). The sizes estimated for these systems are larger than the values predicted by the thin disk model (Shakura & Sunyaev 1973). On the other hand, the temperature profile estimation in the case of HE0047-1756, SDSS1155+6346, and Q1355-2257 is in agreement with the prediction (p=4/3), within errors, while we obtained values significantly smaller in the case of HE2149-2745 and SDSS0924+0219. In most of the cases we obtained similar results than previous estimations using other datasets. However, for Q1355-2257 this is the first estimation of the accretion disk size and temperature profile for this system (Rojas et al. in prep (b)).

Jiménez-Vicente et al. (2014) presented a join study of 10 lensed quasar image pairs to obtain an average size (r$_s$=$4.5^{+1.5}_{-1.2}$) and temperature profile (p=0.75 ± 0.2). Our estimated sizes are in agreement with this average size, while only HE2149-2745 and SDSS0924+0219 are in agreement with the average temperature profile.

To do a significant statistical analysis of the size and temperature profile of the accretion disk we need to increase the number of image pairs, in this work we showed the results for 5 new image pairs, i.e. none of them are in the analysis of Jiménez-Vicente et al. (2014).

The second objective is presented in Section 4.2. I presented the time delay calculations for DESJ0408-5354 and PG1115+080, in the frame of COSMOGRAIL collaboration. Furthermore, to evaluate the effect of microlensing in the estimation of the time delays I successfully reproduced the work of Tie & Kochanek (2018a) and implemented the algorithm in two codes available to the community. The first code allows us to quantify the mean microlensing effect affecting each component of the quasar[1] (Section 4.2.2), and the second one allows us to illustrate the effect of microlensing on light curves depending where the disk is located on the magnification map[2] (Section 4.2.3). We applied this analysis to PG1115-080 (Bonvin et al. 2018; Chen et al. 2018), and we found that, in the worst cases, microlensing will affect the time delay estimation in: $< dt >_{AB} \sim 0.3^{+4.4}_{-4.5}$ days, $< dt >_{AC} \sim 0.6^{+2.3}_{-2.7}$ days, and $< dt >_{BC} \sim 0.6^{+2.9}_{-3.8}$ days. As this estimations relies in not well studied assumptions, e.g. the thin disk model, we decided against using it in our final time delays estimations.

[1]the code can be found in $https://github.com/Krojas/Mean\_Delay$

[2]this code can be found in https://github.com/Krojas/Micro_LC

Further studies are needed to propagate the microlensing time delay to the time delay measurements. For instance, we need a better understanding of the accretion disk model and a larger sample to finally use the precise time delay measurements to estimate the Hubble constant.

The STRIDES group is working to increase the lensed quasar sample. In Section 4.3 I presented some of the discoveries made by this collaboration, where I participated as observer during 5 runs in SOAR telescope. All the techniques implemented to search for the lens quasars have been developed in preparation for the large amount of data that are going to provide the new telescopes (LSST and Euclid).

(3) We performed a dynamical analysis for the lens galaxy groups SL2S J02140-0535 and SL2S08521-0343, and the lens galaxy cluster Abell 1703. For all of the systems I presented the confirmation of members using new spectroscopic candidates, and the velocity dispersion measurement.

For SL2S J02140-0535 we confirmed 24 members and measured $\sigma(v)_{los} = 562 \pm 60$ km s^{-1}. We used this information to perform a combined analysis using dynamics and strong lensing. This analysis provides better constraints of the mass density profile of the lens. Using a NFW, we obtained a scale radius $r_s = 83^{+44}_{-17}$ and a value for the concentration $c_{200}=10^{+2}_{-3}$ (Verdugo et al. 2016).

For SL2S 085207-034315 we confirmed 10 members at z=0.44 and $\sigma(v)_{los} = 601^{+38}_{-94}$ km s^{-1}. In the case of Abell 1703, we confirmed 95 galaxy members and estimated a $\sigma(v)_{los} = 1380 \pm 60$ km s^{-1}. The dynamical analysis of Abell 1703 will be presented in Motta et al. in prep. A combined analysis to study the mass distribution will be carry out on SL2S 085207-034315 and Abell 1703 and will be presented in Verdugo et al. in prep.

Agradecimientos

Quiero agradecer en primer lugar a la Dr. Verónica Motta, directora de mi tesis, quien me motivó y guió durante todos estos años.

A los profesores del Instituto de Física y Astronomía de la Universidad de Valparaíso (IFA), cada uno de ellos me entregó diversas herramientas esenciales, educativas y humanas, para sobrevivir en el mundo de la astronomía.

Agradecer al comité, Eric Jullo y Dante Minniti, por su tiempo y sus valiosos comentarios que ayudaron a mejorar este trabajo.

A mis amigos y compañeros en esta aventura del doctorado, los días de trabajo no habrían sido lo mismo sin su compañía. En especial agradecer a Nicolás Medina cuya enorme paciencia, cariño, apoyo y motivación fueron fundamentales durante este camino.

A mi familia que siempre me ha apoyado en cada uno de mis pasos. En especial a mi madre, Rosa Olate, que desde pequeña me motivó a perseguir mis sueños. También a mis amigos fuera del mundo científico por estar siempre a mi lado a pesar de la distancia.

Finalmente agradecer a quienes financiaron este trabajo, becas de doctorado FIB-UV 2015/2016 y Becas de Doctorado Nacional CONICYT 2017 folio 21170166. Tambíen agradecer al programa LSSTC Data Science Fellowship por la gran oportunidad de perfeccionar mis conocimientos.

Bibliography

Abe, F., Bennett, D. P., Bond, I. A., et al. 2004, Science, 305, 1264

Abell, G. O. 1958, ApJS, 3, 211

Acebron, A., Jullo, E., Limousin, M., et al. 2017, MNRAS, 470, 1809

Agnello, A., Grillo, C., Jones, T., et al. 2018a, MNRAS, 474, 3391

Agnello, A., Kelly, B. C., Treu, T., & Marshall, P. J. 2015a, MNRAS, 448, 1446

Agnello, A., Lin, H., Buckley-Geer, L., et al. 2017, MNRAS, 472, 4038

Agnello, A., Lin, H., Kuropatkin, N., et al. 2018b, MNRAS

Agnello, A., Treu, T., Ostrovski, F., et al. 2015b, MNRAS, 454, 1260

Alam, S., Zhu, H., Croft, R. A. C., et al. 2017, MNRAS, 470, 2822

Alard, C. 2009, A&A, 506, 609

Alcock, C., Allen, W. H., Allsman, R. A., et al. 1997, ApJ, 491, 436

Alcock, C., Allsman, R. A., Alves, D. R., et al. 2000, ApJ, 542, 281

Alonso-García, J., Dékány, I., Catelan, M., et al. 2015, AJ, 149, 99

Alonso-García, J., Mateo, M., Sen, B., et al. 2012, AJ, 143, 70

Alves-Brito, A., Barbuy, B., Zoccali, M., et al. 2006, A&A, 460, 269

Anguita, T., Schechter, P. L., Kuropatkin, N., et al. 2018, ArXiv e-prints

Barbuy, B., Bica, E., & Ortolani, S. 1998, A&A, 333, 117

Bate, N. F., Floyd, D. J. E., Webster, R. L., & Wyithe, J. S. B. 2008, MNRAS, 391, 1955

Bayliss, D., Zhou, G., Penev, K., et al. 2013, AJ, 146, 113

Beers, T. C., Flynn, K., & Gebhardt, K. 1990, AJ, 100, 32

Bennett, C. L., Larson, D., Weiland, J. L., et al. 2013, ApJS, 208, 20

Blackburne, J. A., Pooley, D., Rappaport, S., & Schechter, P. L. 2011, ApJ, 729, 34

Bolton, A. S. 2004, in , 1479

Bonnarel, F., Fernique, P., Bienaymé, O., et al. 2000, A&AS, 143, 33

Bonvin, V., Chan, J. H. H., Millon, M., et al. 2018, ArXiv e-prints

Bonvin, V., Courbin, F., Suyu, S. H., et al. 2017, MNRAS, 465, 4914

Braibant, L., Hutsemékers, D., Sluse, D., Anguita, T., & García-Vergara, C. J. 2014, A&A, 565, L11

Browne, I. W. A., Wilkinson, P. N., Jackson, N. J. F., et al. 2003, MNRAS, 341, 13

Burud, I., Courbin, F., Magain, P., et al. 2002, A&A, 383, 71

Cabanac, R. A., Alard, C., Dantel-Fort, M., et al. 2007, A&A, 461, 813

Cabanac, R. A., Fort, B., Gavazzi, R., & Sl2S Team. 2006, 329

Cackett, E. M., Horne, K., & Winkler, H. 2007, MNRAS, 380, 669

Calchi Novati, S., Gould, A., Udalski, A., et al. 2015, ApJ, 804, 20

Calchi Novati, S., Paulin-Henriksson, S., An, J., et al. 2005, A&A, 443, 911

Chang, K. & Refsdal, S. 1979, Nature, 282, 561

Chang, K. & Refsdal, S. 1984, A&A, 132, 168

Chantry, V., Sluse, D., & Magain, P. 2010, A&A, 522, A95

Chen, G. C.-F., Fassnacht, C. D., Chan, J. H. H., et al. 2018, ArXiv e-prints

Chwolson, O. 1924, Astronomische Nachrichten, 221, 329

Clowe, D., Bradač, M., Gonzalez, A. H., et al. 2006, APJ, 648, L109

Collier, S. J., Horne, K., Kaspi, S., et al. 1998, ApJ, 500, 162

Congdon, A. B. & Keeton, C. R. 2005, MNRAS, 364, 1459

Courbin, F., Bonvin, V., Buckley-Geer, E., et al. 2018, A&A, 609, A71

Dai, X., Kochanek, C. S., Chartas, G., et al. 2010, ApJ, 709, 278

Dalton, G. B., Caldwell, M., Ward, A. K., et al. 2006, in , 62690X

Davis, A. N., Huterer, D., & Krauss, L. M. 2003, MNRAS, 344, 1029

DES Collaboration, Abbott, T. M. C., Abdalla, F. B., et al. 2017, ArXiv e-prints

Dominik, M. 2010, General Relativity and Gravitation, 42, 2075

Dressler, A. & Shectman, S. A. 1988, AJ, 95, 985

Eddington, A. S. 1919, The Observatory, 42, 119

Edelson, R., Gelbord, J. M., Horne, K., et al. 2015, ApJ, 806, 129

Efron, B. 1979, Ann. Statist., 7, 1

Eigenbrod, A., Courbin, F., & Meylan, G. 2007, A&A, 465, 51

Eigenbrod, A., Courbin, F., Meylan, G., et al. 2008, A&A, 490, 933

Eigenbrod, A., Courbin, F., Meylan, G., Vuissoz, C., & Magain, P. 2006, A&A, 451, 759

Eigenbrod, A., Courbin, F., Vuissoz, C., et al. 2005, A&A, 436, 25

Einstein, A. 1936, Science, 84, 506

Emerson, J. P., Irwin, M. J., Lewis, J., et al. 2004, in proc. SPIE, Vol. 5493, Optimizing Scientific Return for Astronomy through Information Technologies, ed. P. J. Quinn & A. Bridger, 401–410

Evans, N. W. & Belokurov, V. 2002, APJ, 567, L119

Fadely, R. & Keeton, C. R. 2011, AJ, 141, 101

Fadely, R., Keeton, C. R., Nakajima, R., & Bernstein, G. M. 2010, ApJ, 711, 246

Falco, E. E., Impey, C. D., Kochanek, C. S., et al. 1999, ApJ, 523, 617

Falco, E. E., Shapiro, I. I., Moustakas, L. A., & Davis, M. 1997, ApJ, 484, 70

Fausnaugh, M. M., Denney, K. D., Barth, A. J., et al. 2016, ApJ, 821, 56

Feynman, R. 1963, The Feynman Lectures on Physics

Floyd, D. J. E., Bate, N. F., & Webster, R. L. 2009, MNRAS, 398, 233

Foëx, G., Motta, V., Jullo, E., Limousin, M., & Verdugo, T. 2014, A&A, 572, A19

Foëx, G., Motta, V., Limousin, M., et al. 2013, A&A, 559, A105

Frenk, C. S., Evrard, A. E., White, S. D. M., & Summers, F. J. 1996, ApJ, 472, 460

Gaia Collaboration, Brown, A. G. A., Vallenari, A., et al. 2018, ArXiv e-prints

Gaia Collaboration, Prusti, T., de Bruijne, J. H. J., et al. 2016, A&A, 595, A1

Girardi, M., Mercurio, A., Balestra, I., et al. 2015, A&A, 579, A4

Gonzalez, O. A., Rejkuba, M., Zoccali, M., Valenti, E., & Minniti, D. 2011, A&A, 534, A3

Gonzalez, O. A., Rejkuba, M., Zoccali, M., et al. 2012, A&A, 543, A13

Gould, A. 2001, PASP, 113, 903

Gould, A. 2005, New Astronomy Reviews, 49, 424

Gould, A., Udalski, A., Shin, I.-G., et al. 2014, Science, 345, 46

Guerras, E., Mediavilla, E., Jimenez-Vicente, J., et al. 2013a, ApJ, 764, 160

Guerras, E., Mediavilla, E., Jimenez-Vicente, J., et al. 2013b, ApJ, 778, 123

Hambly, N. C., Mann, R. G., Bond, I., et al. 2004, in proc. SPIE, Vol. 5493, Optimizing Scientific Return for Astronomy through Information Technologies, ed. P. J. Quinn & A. Bridger, 423–431

Hennawi, J. F., Dalal, N., & Bode, P. 2007, ApJ, 654, 93

Hewitt, J. N., Turner, E. L., Schneider, D. P., Burke, B. F., & Langston, G. I. 1988, Nature, 333, 537

Hoffman, M. D. & Gelman, A. 2011, ArXiv e-prints

Howarth, I. D., Murray, J., Mills, D., & Berry, D. S. 2004, Starlink User Note, 50

Inada, N., Becker, R. H., Burles, S., et al. 2003, AJ, 126, 666

Inada, N., Oguri, M., Morokuma, T., et al. 2006, APJ, 653, L97

Inada, N., Oguri, M., Shin, M.-S., et al. 2012, AJ, 143, 119

Irwin, M. J., Lewis, J., Hodgkin, S., et al. 2004, in proc. SPIE, Vol. 5493, Optimizing Scientific Return for Astronomy through Information Technologies, ed. P. J. Quinn & A. Bridger, 411–422

Irwin, M. J., Webster, R. L., Hewett, P. C., Corrigan, R. T., & Jedrzejewski, R. I. 1989, AJ, 98, 1989

Ivezić, Ž., Connolly, A., Vanderplas, J., & Gray, A. 2014, Statistics, Data Mining and Machine Learning in Astronomy (Princeton University Press)

Jauzac, M., Clément, B., Limousin, M., et al. 2014, MNRAS, 443, 1549

Jauzac, M., Jullo, E., Kneib, J.-P., et al. 2012, MNRAS, 426, 3369

Jiménez-Vicente, J., Mediavilla, E., Kochanek, C. S., & Muñoz, J. A. 2015a, ApJ, 799, 149

Jiménez-Vicente, J., Mediavilla, E., Kochanek, C. S., & Muñoz, J. A. 2015b, ApJ, 806, 251

Jiménez-Vicente, J., Mediavilla, E., Kochanek, C. S., et al. 2014, ApJ, 783, 47

Jiménez-Vicente, J., Mediavilla, E., Muñoz, J. A., & Kochanek, C. S. 2012, ApJ, 751, 106

Jullo, E., Kneib, J.-P., Limousin, M., et al. 2007, New Journal of Physics, 9, 447

Jullo, E., Natarajan, P., Kneib, J.-P., et al. 2010, Science, 329, 924

Keeton, C. R. 2001, ArXiv Astrophysics e-prints

Keeton, C. R., Burles, S., Schechter, P. L., & Wambsganss, J. 2006a, ApJ, 639, 1

Keeton, C. R., Burles, S., Schechter, P. L., & Wambsganss, J. 2006b, ApJ, 639, 1

Kepler, S. O., Kleinman, S. J., Nitta, A., et al. 2007, MNRAS, 375, 1315

Kiraga, M. & Paczynski, B. 1994, APJ, 430, L101

Kneib, J. & Natarajan, P. 2011, The Astronomy and Astrophysics Review, 19, 47

Kneib, J.-P. 1993, PhD thesis, Ph. D. thesis, Université Paul Sabatier, Toulouse, (1993)

Kochanek, C. S. 1991, ApJ, 373, 354

Kochanek, C. S. 2004, ApJ, 605, 58

Kochanek, C. S., Falco, E. E., Impey, C. D., et al. 1999, in , 163–175

Kochanek, C. S., Keeton, C. R., & McLeod, B. A. 2001, ApJ, 547, 50

Koester, B. P., McKay, T. A., Annis, J., et al. 2007, ApJ, 660, 239

Komatsu, E., Dunkley, J., Nolta, M. R., et al. 2009, ApJS, 180, 330

Kundic, T., Cohen, J. G., Blandford, R. D., & Lubin, L. M. 1997, AJ, 114, 507

Kurtz, M. J. & Mink, D. J. 1998, PASP, 110, 934

Laplace, P. 1794

Lieu, M., Smith, G. P., Giles, P. A., et al. 2016, A&A, 592, A4

Limousin, M., Cabanac, R., Gavazzi, R., et al. 2009, A&A, 502, 445

Limousin, M., Morandi, A., Sereno, M., et al. 2013, Space Science Reviews, 177, 155

Limousin, M., Richard, J., Kneib, J.-P., et al. 2008, A&A, 489, 23

Lin, H., Buckley-Geer, E., Agnello, A., et al. 2017, APJ, 838, L15

Lira, P., Arévalo, P., Uttley, P., McHardy, I. M. M., & Videla, L. 2015, MNRAS, 454, 368

Lopez, S., Wucknitz, O., & Wisotzki, L. 1998, A&A, 339, L13

Lynds, R. & Petrosian, V. 1986, 1014

MacLeod, C. L., Morgan, C. W., Mosquera, A., et al. 2015, ApJ, 806, 258

Magaña, J., Motta, V., Cárdenas, V. H., Verdugo, T., & Jullo, E. 2015, ApJ, 813, 69

Mamon, G. A., Biviano, A., & Boué, G. 2013, MNRAS, 429, 3079

Mandelbaum, R., Li, C., Kauffmann, G., & White, S. D. M. 2009, MNRAS, 393, 377

Mao, S., Smith, M. C., Woźniak, P., et al. 2002, MNRAS, 329, 349

Mediavilla, E., Jiménez-vicente, J., Muñoz, J. A., & Mediavilla, T. 2015, APJ, 814, L26

Mediavilla, E., Mediavilla, T., Muñoz, J. A., et al. 2011, ApJ, 741, 42

Mediavilla, E., Muñoz, J. A., Falco, E., et al. 2009, ApJ, 706, 1451

Mediavilla, E., Muñoz, J. A., Kochanek, C. S., et al. 2005, ApJ, 619, 749

Mediavilla, E., Muñoz, J. A., Lopez, P., et al. 2006, ApJ, 653, 942

Medina, N., Borissova, J., Bayo, A., et al. 2018, ArXiv e-prints

Michell, J. 1784, Trans. R. Soc. London, 74, 35

Minniti, D. 1995, AJ, 109, 1663

Minniti, D., Contreras Ramos, R., Alonso-García, J., et al. 2015, APJ, 810, L20

Minniti, D., Lucas, P. W., Emerson, J. P., et al. 2010, New A, 15, 433

Miralda-Escude, J. & Lehar, J. 1992, MNRAS, 259, 31P

More, A., Cabanac, R., More, S., et al. 2012, ApJ, 749, 38

Morgan, C. W., Kochanek, C. S., Dai, X., Morgan, N. D., & Falco, E. E. 2008, ApJ, 689, 755

Morgan, C. W., Kochanek, C. S., Morgan, N. D., & Falco, E. E. 2006, ApJ, 647, 874

Morgan, C. W., Kochanek, C. S., Morgan, N. D., & Falco, E. E. 2010, ApJ, 712, 1129

Morgan, N. D., Gregg, M. D., Wisotzki, L., et al. 2003, AJ, 126, 696

Morgan, N. D., Kochanek, C. S., Pevunova, O., & Schechter, P. L. 2005, AJ, 129, 2531

Mosquera, A. M. & Kochanek, C. S. 2011, ApJ, 738, 96

Mosquera, A. M., Muñoz, J. A., & Mediavilla, E. 2009, ApJ, 691, 1292

Motta, V., Mediavilla, E., Falco, E., & Muñoz, J. A. 2012, ApJ, 755, 82

Motta, V., Mediavilla, E., Muñoz, J. A., et al. 2002, ApJ, 574, 719

Motta, V., Mediavilla, E., Rojas, K., et al. 2017, ApJ, 835, 132

Moustakas, L. A. & Metcalf, R. B. 2003, MNRAS, 339, 607

Muñoz, J. A., Falco, E. E., Kochanek, C. S., McLeod, B. A., & Mediavilla, E. 2004, ApJ, 605, 614

Muñoz, J. A., Kochanek, C. S., & Keeton, C. R. 2001, ApJ, 558, 657

Muñoz, R. P., Motta, V., Verdugo, T., et al. 2013, A&A, 552, A80

Myers, S. T., Jackson, N. J., Browne, I. W. A., et al. 2003, VizieR Online Data Catalog, 8072

Narayan, R. & Bartelmann, M. 1996, ArXiv Astrophysics e-prints

Navarro, J. F., Frenk, C. S., & White, S. D. M. 1996, ApJ, 462, 563

Navarro, J. F., Frenk, C. S., & White, S. D. M. 1997, ApJ, 490, 493

Navarro, M. G., Minniti, D., & Contreras Ramos, R. 2017, APJ, 851, L13

Navarro Molina, C., Borissova, J., Catelan, M., et al. 2016, MNRAS, 462, 1180

Nishiyama, S., Tamura, M., Hatano, H., et al. 2009, ApJ, 696, 1407

Ochsenbein, F., Bauer, P., & Marcout, J. 2000, A&AS, 143, 23

Ofek, E. O., Maoz, D., Rix, H.-W., Kochanek, C. S., & Falco, E. E. 2006, ApJ, 641, 70

Oguri, M., Inada, N., Pindor, B., et al. 2006, AJ, 132, 999

Oguri, M., Ofek, E. O., Inada, N., et al. 2008, APJ, 676, L1

Oguri, M., Schrabback, T., Jullo, E., et al. 2013, MNRAS, 429, 482

Oguri, M., Taruya, A., Suto, Y., & Turner, E. L. 2002, ApJ, 568, 488

Ortolani, S., Renzini, A., Gilmozzi, R., et al. 1995, Nature, 377, 701

Ostrovski, F., McMahon, R. G., Connolly, A. J., et al. 2017, MNRAS, 465, 4325

Ota, N., Oguri, M., Dai, X., et al. 2012, ApJ, 758, 26

Paczynski, B. 1991, APJ, 371, L63

Paczynski, B. 1996, ARA&A, 34, 419

Peng, C. Y., Impey, C. D., Rix, H.-W., et al. 2006, ApJ, 649, 616

Pindor, B., Eisenstein, D. J., Inada, N., et al. 2004, AJ, 127, 1318

Planck Collaboration, Aghanim, N., Ashdown, M., et al. 2016, A&A, 596, A107

Pooley, D., Blackburne, J. A., Rappaport, S., & Schechter, P. L. 2007, ApJ, 661, 19

Pooley, D., Rappaport, S., Blackburne, J., et al. 2009, ApJ, 697, 1892

Rattenbury, N. J., Abe, F., Bennett, D. P., et al. 2005, A&A, 439, 645

Refsdal, S. 1964a, MNRAS, 128, 307

Refsdal, S. 1964b, MNRAS, 128, 295

Refsdal, S. 1966a, MNRAS, 134, 315

Refsdal, S. 1966b, MNRAS, 132, 101

Refsdal, S. & Surdej, J. 1994, Reports on Progress in Physics, 57, 117

Richard, J., Pei, L., Limousin, M., Jullo, E., & Kneib, J. P. 2009, A&A, 498, 37

Riess, A. G., Casertano, S., Yuan, W., et al. 2018, ApJ, 855, 136

Rojas, K., Motta, V., Mediavilla, E., et al. 2014, ApJ, 797, 61

Saito, R. K., Hempel, M., Minniti, D., et al. 2012, A&A, 537, A107

Salvatier, J., Wiecki, T., & Fonnesbeck, C. 2016, PeerJ Computer Science, 2:e55

Schechter, P. L., Bailyn, C. D., Barr, R., et al. 1997, APJ, 475, L85

Schechter, P. L., Mateo, M., & Saha, A. 1993, PASP, 105, 1342

Schneider, P. 1984, A&A, 140, 119

Schneider, P. 2006, 1–89

Schneider, P., Ehlers, J., & Falco, E. E. 1992, Gravitational Lenses

Shakura, N. I. & Sunyaev, R. A. 1973, A&A, 24, 337

Shvartzvald, Y., Bryden, G., Gould, A., et al. 2017, AJ, 153, 61

Skowron, J., Jaroszynski, M., Udalski, A., et al. 2007, Acta Astron, 57, 281

Skrutskie, M. F., Cutri, R. M., Stiening, R., et al. 2006, AJ, 131, 1163

Sluse, D., Hutsemékers, D., Courbin, F., Meylan, G., & Wambsganss, J. 2012, A&A, 544, A62

Sluse, D., Surdej, J., Claeskens, J.-F., et al. 2003, A&A, 406, L43

Smith, L. C., Lucas, P. W., Kurtev, R., et al. 2018, MNRAS, 474, 1826

Soldner. 1804, Annalen der Physik, 17, 44

Soucail, G., Fort, B., Mellier, Y., & Picat, J. P. 1987, A&A, 172, L14

Soucail, G., Mellier, Y., Fort, B., Mathez, G., & Cailloux, M. 1988, A&A, 191, L19

Springel, V., White, S. D. M., Jenkins, A., et al. 2005, Nature, 435, 629

Stockton, A. 1980, APJ, 242, L141

Sumi, T., Bennett, D. P., Bond, I. A., et al. 2013, ApJ, 778, 150

Suyu, S. H., Auger, M. W., Hilbert, S., et al. 2013, ApJ, 766, 70

Taylor, M. B. 2006, in Astronomical Society of the Pacific Conference Series, Vol. 351, Astronomical Data Analysis Software and Systems XV, ed. C. Gabriel, C. Arviset, D. Ponz, & S. Enrique

Tie, S. S. & Kochanek, C. S. 2018a, MNRAS, 473, 80

Tie, S. S. & Kochanek, C. S. 2018b, MNRAS, 473, 616

Tisserand, P., Le Guillou, L., Afonso, C., et al. 2007, A&A, 469, 387

Tonry, J. L. 1998, AJ, 115, 1

Treu, T., Agnello, A., & Strides Team. 2015, in , 318.04

Tsvetkova, V. S., Vakulik, V. G., Shulga, V. M., et al. 2010, MNRAS, 406, 2764

Tully, R. B. 2015, AJ, 149, 54

Udalski, A., Yee, J. C., Gould, A., et al. 2015, ApJ, 799, 237

Vanderplas, J., Connolly, A., Ivezić, Ž., & Gray, A. 2012, in Conference on Intelligent Data Understanding (CIDU), 47 –54

Verdugo, T., Limousin, M., Motta, V., et al. 2016, A&A, 595, A30

Verdugo, T., Motta, V., Foëx, G., et al. 2014, A&A, 571, A65

Verdugo, T., Motta, V., Muñoz, R. P., et al. 2011, A&A, 527, A124

Vernardos, G., Fluke, C. J., Bate, N. F., & Croton, D. 2014, ApJS, 211, 16

von Neumann, J. 1941, Ann. Math. Statist., 12, 367

Vuissoz, C., Courbin, F., Sluse, D., et al. 2007, A&A, 464, 845

Walsh, D., Carswell, R. F., & Weymann, R. J. 1979, Nature, 279, 381

Wambsganss, J. 2006, in Saas-Fee Advanced Course 33: Gravitational Lensing: Strong, Weak and Micro, 453–540

Wambsganss, J. & Paczynski, B. 1991, AJ, 102, 864

Wambsganss, J., Witt, H. J., & Schneider, P. 1992, A&A, 258, 591

Wanders, I., Peterson, B. M., Alloin, D., et al. 1997, ApJS, 113, 69

Weymann, R. J., Latham, D., Angel, J. R. P., et al. 1980, Nature, 285, 641

Williams, P. R., Agnello, A., Treu, T., et al. 2018, MNRAS, 477, L70

Wilman, D. J., Balogh, M. L., Bower, R. G., et al. 2005, MNRAS, 358, 88

Wisotzki, L., Koehler, T., Ikonomou, M., & Reimers, D. 1995, A&A, 297, L59

Wisotzki, L., Koehler, T., Lopez, S., & Reimers, D. 1996, A&A, 315, 405

Wisotzki, L., Schechter, P. L., Chen, H.-W., et al. 2004, A&A, 419, L31

Wyrzykowski, Ł., Kostrzewa-Rutkowska, Z., Skowron, J., et al. 2016, MNRAS, 458, 3012

Wyrzykowski, Ł., Rynkiewicz, A. E., Skowron, J., et al. 2015, ApJS, 216, 12

Yee, J. C., Hung, L.-W., Bond, I. A., et al. 2013, ApJ, 769, 77

Yonehara, A., Hirashita, H., & Richter, P. 2008, A&A, 478, 95

York, D. G., Adelman, J., Anderson, Jr., J. E., et al. 2000, AJ, 120, 1579

Young, P., Deverill, R. S., Gunn, J. E., Westphal, J. A., & Kristian, J. 1981, ApJ, 244, 723

Young, P., Gunn, J. E., Kristian, J., Oke, J. B., & Westphal, J. A. 1980, ApJ, 241, 507

Zoccali, M., Renzini, A., Ortolani, S., et al. 2001, ApJ, 553, 733

Zwicky, F. 1937a, Physical Review, 51, 290

Zwicky, F. 1937b, Physical Review, 51, 679

List of Tables

List of Figures